Ultrahigh energy cosmic rays

Antoine Letessier-Selvon*

LPNHE, University of Paris UPMC, CNRS/IN2P3, 4, place Jussieu, 75252 Paris Cedex 05—France

Todor Stanev†

Bartol Research Institute, Department of Physics and Astronomy, University of Delaware, Newark, Delaware 19716, USA

(Received 30 September 2010; published 7 September 2011)

This is a review of the most resent results from the investigation of the ultrahigh energy cosmic rays, particles of energy exceeding 10^{18} eV. After a general introduction to the topic and a brief review of the lower energy cosmic rays and the detection methods, the two most recent experiments, the High Resolution Fly's Eye and the Southern Auger Observatory, are described. Results from these two experiments on the cosmic ray energy spectrum, the chemical composition of these cosmic rays, and searches for their sources are presented. An analysis of the controversies in these results and the projects in development and construction that can help solve the remaining problems with these particles is also presented.

DOI: 10.1103/RevModPhys.83.907 PACS numbers: 96.50.S−, 96.50.sd, 98.70.Sa, 96.50.sb

CONTENTS

*Antoine.Letessier-Selvon@in2p3.fr
†stanev@bartol.udel.edu

I. INTRODUCTION

Cosmic rays are defined as charged nuclei that originate outside the solar system. Such nuclei of total energy between 1 GeV to above 10^{11} GeV have been detected. Below energies of several GeV cosmic rays are usually studied in terms of kinetic energy $E_k = E_{\text{tot}} - mc^2$. In such terms, the cosmic ray energy spectrum extends more than 14 orders of magnitude, from 10^6 eV to above 10^{20} eV.

The exploration of cosmic rays began as a mixture of physics and environmental studies almost a hundred years ago. After the discovery of radioactivity, it was noticed that between 10 and 20 ions were generated per cubic centimeter of air every second. The main question was if this ionization was a product of the natural radioactivity of the Earth. The agent of this radioactivity was assumed to be γ rays because the two other types of radioactive rays, α rays (ionized He nuclei) and β rays (electrons), were easily shielded. To prove that natural radioactivity is the culprit, physicists started

measurements of the ionization at different heights above the surface. Such measurements were done at the Eiffel tower.

Just before the first World War, Victor Hess started measuring the ionization on balloons. In 1912, he flew a balloon from Austria to an altitude of 5 km and to everybody's surprise, the ionization increased by a factor of 2 rather than decreased. Werner Kohlhörster flew balloons to altitudes exceeding 9 km in Germany and measured an even higher ionization level of the *Höhenstrahlung* (high altitude radiation), as the cosmic rays were called by the first explorers. The term *cosmic rays* was put together by Robert Millikan, who was trying to prove that cosmic rays are 10 to 100 MeV γ rays from nucleosynthesis of the common C and O elements.

Kohlhörster continued his cosmic ray research during the 1930s. In collaboration with Walther Bothe, he proved that cosmic rays can penetrate through heavy absorbers. Bruno Rossi shielded his detectors with 1 m of lead and saw some cosmic rays still penetrating. Many expeditions were organized at high mountains to study the interactions of cosmic rays with the geomagnetic field. Arthur Compton organized expeditions at different geomagnetic latitudes, which proved that cosmic rays are positively charged particles. More come from the West than from the East because the geomagnetic field bends positively charged particles coming from the West towards the surface of the Earth and those from the East away from it.

Cosmic ray research was the basis for the development of the QED and the electromagnetic cascade theory. Towards the end of the decade, Pierre Auger and collaborators made several experiments at high mountain altitudes where they ran in coincidence Geiger-Müller tubes at large distances from each other. They concluded that primary cosmic rays generate showers in the atmosphere. Kohlhörster and Rossi ran similar experiments even earlier, but of smaller dimensions. Auger estimated that the showers that were detected came from a primary cosmic ray of energy up to 10^6 GeV. The term "shower" is an English interpretation by Patrick Blackett of the Italian expression *sciami* that Rossi used in conversations with Beppo Occhialini. The knowledge accumulated in the 1930s was published in the magnificent article of Rossi and Greisen (1941) "Cosmic Ray Theory." This is the beginning of the investigations of high energy cosmic rays, their energy spectrum, and composition.

Figure 1 shows the energy spectrum of cosmic rays with energy above 10^{11} eV. Note that the lower energy cosmic ray spectrum at Earth is affected by the magnetic fields of the heliosphere and the geomagnetic field. The cosmic ray flux as a function of energy is multiplied by E^2 to emphasize the spectral shape and to indicate the amount of energy carried by cosmic rays of different energy. This is a smooth power law spectrum that contains three general features: the cosmic ray *knee* above 10^{15} eV, the cosmic ray *ankle* at about 3×10^{18} eV (3 EeV), and the *cutoff* above 3×10^{19} eV. The approximate positions of the knee and ankle are indicated with arrows above them. The cosmic ray spectrum below the knee is a power law $E^{-\alpha}$ with spectral index $\alpha = 2.7$. Above the knee, the spectral index increases with $\Delta\alpha = 0.3$. Above the ankle, the power law spectrum becomes flatter and similar to that before the knee.

The values of the spectral indices show that below the knee the flux decreases by a factor of 50 when the energy increases

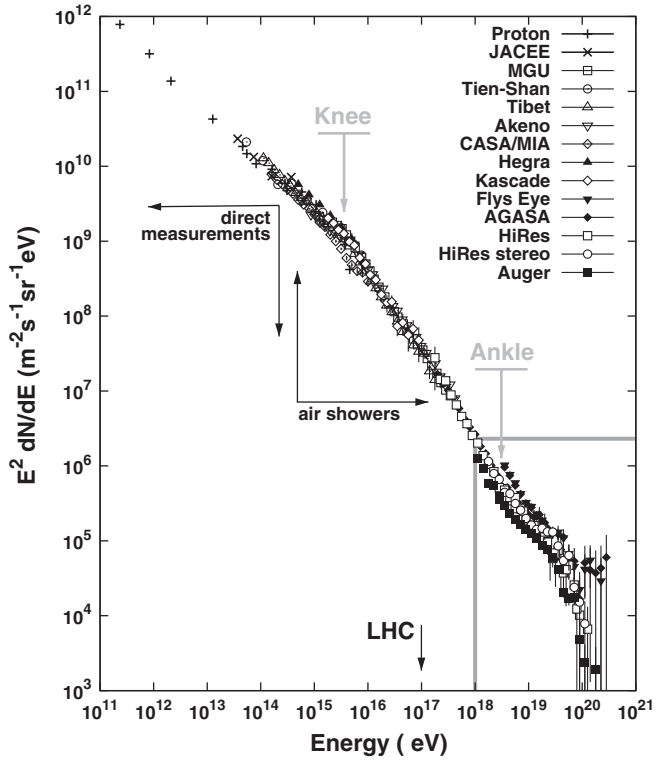

FIG. 1. Differential energy spectrum of cosmic rays of energy above 10^{11} eV multiplied by E^2. The positions of the cosmic rays knee and ankle are indicated with gray arrows. The experiments that contribute data to this graph are shown. The equivalent laboratory energy of the Large Hadron Collider is also shown.

by an order of magnitude. Above the knee, the decrease is by a factor of 100. Because of the decrease, cosmic rays of energy above 10^{14} eV are difficult to measure by direct experiments performed on balloons and satellites. The flux of such cosmic rays is about 3 particles per hour per steradian in one square-meter detector. Particles above 10^{15} eV can only be measured by air-shower arrays of areas more than 10^4 m^2. Various air-shower experiments obviously have different energy assignments that lead to the inconsistencies in the presented spectra.

The standard thinking in the field of cosmic rays is that particles of energy below and around the knee are accelerated at galactic astrophysical objects, mainly at supernova remnants and possibly at powerful binary systems. The knee itself is probably a result of reaching the maximum energy of such accelerators. Particles above the ankle are believed to be of extragalactic origin. They may be accelerated at active galactic nuclei (AGN), at radio galaxies, in gamma-ray bursts (GRB), or in other powerful astrophysical systems. It is not obvious where the particles above the knee and below the ankle are accelerated, possibly at some special, very efficient galactic accelerators.

In this article, we concentrate on the cosmic rays of energy above 10^{18} eV, in the lower right hand part of the graph. The search for such high energy cosmic rays started in the 1950s by the MIT group led by B. Rossi. The first announcement of a cosmic ray shower of energy above 10^{19} eV came from the Volcano Ranch air-shower array in New Mexico (Linsley *et al.*, 1961) that had an area of about 8 km^2. Two years later,

John Linsley reported on the detection of an event of energy 10^{20} eV (Linsley, 1963). The discoveries continued during the next 50 years with larger and larger arrays but the total of world statistics is still small.

These are the ultrahigh energy cosmic rays (UHECR) at least a part of which are of extragalactic origin. We discuss the requirements for acceleration of such particles that carry more than 7 orders of magnitude more energy than the Large Hadron Collider (LHC) beam and their propagation in the intergalactic space from their sources to us. We introduce the UHECR detection methods and detectors and the results on the cosmic ray spectrum and composition. We concentrate on the new results presented by the High Resolution Fly's Eye experiment and the Auger Southern Observatory to which we often refer as HiRes and Auger. Please consult the excellent review of Nagano and Watson (2000) for the older experiments and results and that of Cronin (1999) for the importance of the research in this field. Some more information could be found in the reviews of Bluemer *et al.* (2009) and Beatty and Westerhoff (2009). We conclude with a discussion of the remaining problems and description of possible future experiments.

II. EXTENSIVE AIR SHOWERS

Extensive air showers (EAS) are the particle cascades following the interaction of a cosmic ray with an atom of the atmosphere. After this first interaction, the atmosphere acts like a calorimeter of variable density with a vertical thickness of more than 11 interaction lengths and 26 radiation lengths.

A 10^{19} eV (10 EeV, 1 EeV $= 10^{18}$ eV) proton vertically striking the top of the atmosphere produces at sea level (atmospheric thickness of 1033 g/cm^2) about 3×10^{10} particles (with energy in excess of 200 keV). 99% of these particles are photons and electrons or positrons (referred to simply as electrons in the following) in a ratio of about 6 to 1. Their energy is mostly in the range of 1 to 10 MeV and they transport 85% of the total energy. The remaining particles are either muons with an average energy of about 1 GeV (carrying about 10% of the total energy), few GeV pions (about 4% of the total energy), and, in smaller proportions, neutrinos and baryons. The shower footprint (more than 1 muon per m^2) on the ground extends over a few km^2.

The basic properties of the development of the cascade can be extracted from a simplified model due to Heitler. It describes the evolution of a pure electromagnetic cascade (Heitler, 1954).

A. Heitler's model of electromagnetic showers

In his model, Heitler described the evolution of electromagnetic cascades as a perfect binary tree (see Fig. 2). At each step, all particles interact and produce two secondaries of equal energy. This description assumes that at each step electrons split their energy in half via bremsstrahlung emission of a single photon while photons produce an electron-positron pair of equal energy. In this simplified approach, all of the processes' cross sections are taken as independent of energy and collision energy losses are ignored.

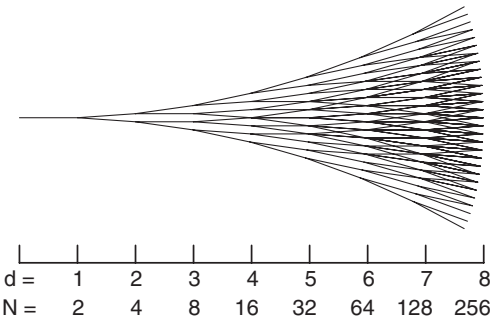

FIG. 2. Heitler's schematic evolution of an electromagnetic cascade. At each stage of the cascade the number of particle is multiplied by two, through either pair creation or single photon bremsstrahlung. The evolution stops when individual particle energy fall below the critical energy, about 80 MeV in air.

The interaction step length d in the cascade is therefore given by the radiation length of the medium λ_r ($\lambda_r = 37$ g/cm^2 in air) as $d = \lambda_r \ln 2$. After n steps, the particle number is $N_n = 2^n$, and their individual energy is E_0/N_n. This development continues until the individual energy drops below a critical value where the rate of energy loss by electrons via bremsstrahlung is equal to the rate of energy loss by ionization. This energy is about $E_c^\gamma = 80$ MeV in air. At this point of development, the electromagnetic cascade has reached a maximum and the number of particles is given by the ratio of the original energy to the critical one.

Although simplified, Heitler's model correctly reproduces three properties of electromagnetic cascades:

(1) The number of particles at the maximum of the cascade development is proportional to the incoming primary cosmic ray energy,

$$N_{\max} = E_0/E_c^\gamma. \tag{1}$$

(2) The evolution of the depth of the maximum of the shower (measured in g/cm^2) is logarithmic with energy,

$$X_{\max} = X_0 + \lambda_r \ln(E_0/E_c^\gamma), \tag{2}$$

where X_0 is the position of the start of the cascade.

(3) The rate of evolution of $X_{\max}$ with energy, the elongation rate, defined as

$$D_{10} \equiv \frac{dX_{\max}}{d\log_{10}E_0} = 2.3\lambda_r \tag{3}$$

is given by the radiation length of the medium. This elongation rate is about 85 g/cm^2 in air.

Extensive simulations of electromagnetic cascades confirm these properties, although the particle number at the maximum is overestimated by about a factor of 2 to 3. Moreover, Heitler's model predicts a ratio of electrons to photons of 2 while simulations and direct cascade measurements in air show a ratio of the order of 1/6th. This is, in particular, due to the facts that multiple photons are emitted during bremsstrahlung and that electrons lose energy much faster than photons do.

B. Extension to hadronic showers

Heitler's model can be adapted to describe hadronic showers (Matthews, 2005; Stanev, 2010). In this case, the relevant parameter is the hadronic interaction length λ_I. At each step of thickness $\lambda_I \ln 2$ it is assumed that hadronic interactions produce $2N_\pi$ charged pions and N_π neutral ones. While π^0 decay immediately and feed the electromagnetic part of the shower, π^+ and π^- interact further. The hadronic cascade continues to grow, feeding the electromagnetic part at each step, until charged pions reach an energy where decay is more likely than a new interaction. A schematic of an hadronic cascade is shown in Fig. 3. The interaction length and the pion multiplicity ($3N_\pi$) are energy independent in the model. The energy is equally shared by the secondary pions. For pion energy between 1 GeV and 10 TeV, a charged multiplicity of 10 ($N_\pi = 5$) is an appropriate number.

One-third of the available energy goes into the electromagnetic component, while the remaining 2/3 continues as hadrons. Therefore, the longer it takes for pions to reach the critical energy E_c^π (20 GeV in air, below which they will decay into muons), the larger the electromagnetic component. Consequently, in long developing showers, the energy of the muons from the decaying pion will be smaller. In addition, because of the density profile of the atmosphere, E_c^π is larger high above ground than at sea level and deep showers will produce fewer muons.

This positive correlation introduces a link between the primary cosmic ray interaction cross section with air and the muon content at the ground. According to those principles, primaries with higher cross sections will have a larger muon to electron ratio at the ground.

To obtain the number of muons in the shower, one simply assumes that all pions decay into muons when they reach the critical energy $N_\mu = (2N_\pi)^{n_c}$, where $n_c = \ln(E_0/E_c^\pi)/\ln 3N_\pi$ is the number of steps needed for the pions to reach E_c^π. Introducing $\beta = \ln 2N_\pi/\ln 3N_\pi$ (0.85 for $N_\pi = 5$) we have

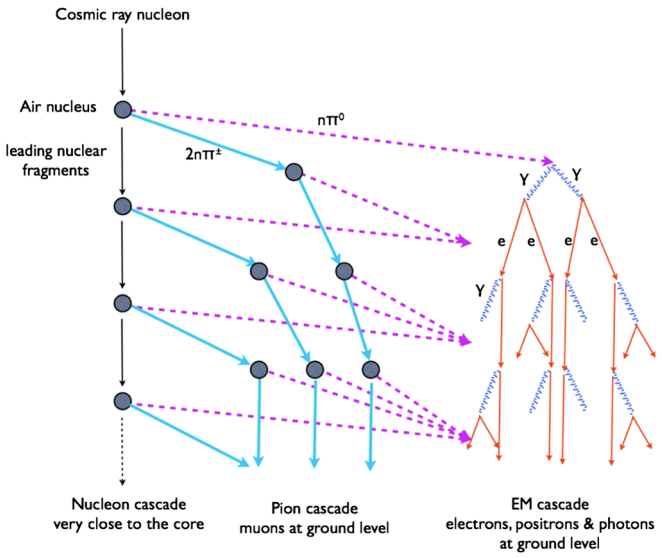

FIG. 3 (color online). Schematic evolution of an hadronic cascade. At each step roughly 1/3 of the energy is transferred from the hadronic cascade to the electromagnetic one.

$$N_\mu = (E_0/E_c^\pi)^\beta. \tag{4}$$

Unlike the electron number, the muon multiplicity does not grow linearly with the primary energy, but at a slower rate. The precise value of β depends on the average pion multiplicity used. It also depends on the inelasticity of the hadronic interactions. Assuming that only half of the available energy goes into pions at each step (rather than all of it as done above) would lead to $\beta = 0.93$. Detailed simulations give values of β in the range 0.9 to 0.95 (Alvarez-Muñiz *et al.*, 2002).

Determination of the position of shower maximum is more complex in the case of a hadronic shower than in the case of a pure electromagnetic one. The larger cross section and the larger multiplicity at each step will reduce the value of $X_{\max}$ while the energy evolution of those quantities will modify the rate of change of $X_{\max}$ with energy, a quantity known as the elongation rate. In addition, the inelasticity of the interaction will also modify both the position of the maximum and the elongation rate. Proper account for the energy transfer from the hadronic component to the electromagnetic one at each step together with a correct superposition of each electromagnetic subshowers to compute $X_{\max}$ is beyond the scope of a simple model, but can be successfully done in a simulation. An approximation based on the sole evolution of the electromagnetic (EM) cascade initiated by the first interaction falls short of the full simulation value by about 100 g/cm^2 (Matthews, 2005).

A good approximation of the elongation rate can be obtained when introducing the cross section and multiplicity energy dependence. Using a proton air cross section of 550 mb at 10^{18} eV and a rate of change of about 50 mb per decade of energy (Ulrich *et al.*, 2009) one obtains

$$\lambda_I \simeq 90 - 9\log(E_0/\mathrm{EeV})\ \mathrm{g/cm^2}. \tag{5}$$

Assuming, as in Matthews (2005), that the first interaction initiates $2N_\pi$ EM cascades of energy $E_0/6N_\pi$ with $N_\pi \propto (E_0/\mathrm{PeV})^{1/5}$ for the evolution of the first interaction multiplicity with energy, one can calculate the elongation rate

$$D_{10}^p = \frac{dX_{\max}}{d\log E_0} = \frac{d(\lambda_I \ln 2 + \lambda_r \ln[E_0/(6N_\pi E_c^\gamma)]}{d\log E_0} \tag{6}$$

or

$$D_{10}^p = \tfrac{4}{5} D_{10}^\gamma - 9\ln 2 \simeq 62\ \mathrm{g/cm^2}. \tag{7}$$

This result is quite robust as it only depends on the cross section and multiplicity evolution with energy. It is in good agreement with simulation codes (Alvarez-Muñiz *et al.*, 2002).

The fast rate of the energy transfer in hadronic showers was noted long ago by Linsley (1977) who introduced the *elongation rate theorem* which stipulates that the elongation rate for electromagnetic showers (D_{10}^γ) is an upper limit to the elongation rate of hadronic showers. This is of course a direct consequence of the larger hadronic multiplicity which increases the rate of conversion of the primary energy into secondary particles.

Extension of this description to nuclear primaries can finally be done using the superposition model. In this framework, the nuclear interaction of a nucleus with atomic

number A is simply viewed as the superposition of the interactions of A nucleons of individual energy E_0/A. Showers from heavy nuclei will therefore develop higher, faster, and with less shower to shower fluctuations than showers initiated by lighter nuclei. The faster development implies that pions in the hadronic cascade will reach their critical energy (where they decay rather than interact) sooner and therefore augment the relative number of muons with respect to the electromagnetic component. From these simple assumptions, one can directly see that (1) shower induced by nuclei with atomic number A will develop higher in the atmosphere. The offset with respect to proton showers is simply

$$X^A_{\max} = X^p_{\max} - \lambda_r \ln A. \tag{8}$$

(2) Showers initiated by nuclei with atomic number A will have a larger muon number

$$N^A_\mu = N^p_\mu A^{1-\beta}. \tag{9}$$

(3) The evolution of the primary cross section and multiplicity with energy for nuclei is the same as for protons. Different nuclei will have identical elongation rates and will show up as parallel lines in an $X_{\max}$ versus energy plot; see Fig. 4. (4) The fluctuation of the position of $X_{\max}$ from one shower to another is smaller for heavy nuclei than for light ones.

All of the above results and properties are qualitatively confirmed by detailed simulations. All interaction models share those basic principles and they all predict that iron showers have a smaller average $X_{\max}$, less fluctuations on $X_{\max}$, and a larger muon to electron ratio at ground than proton ones. In particular, the offset in $X_{\max}$ from iron to proton showers is more than 100 g/cm^2, and iron showers carry about 1.8 times as many muons as proton showers of the same energy. Of course, in quantitative terms there are differences, but all of the basic trends regarding the evolution of $X_{\max}$ and N_μ with energy and atomic number are reproduced.

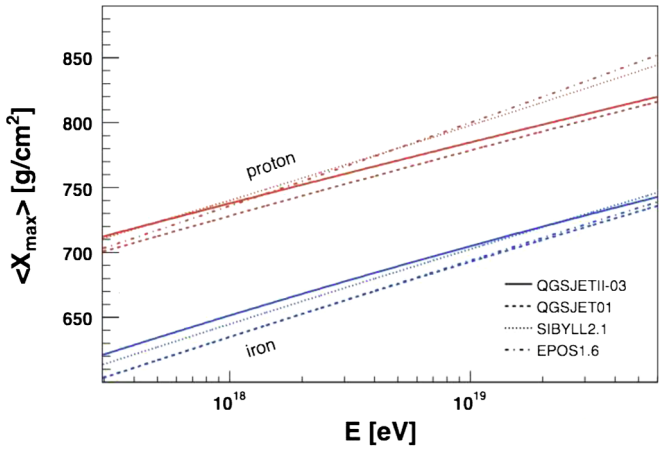

FIG. 4 (color online). Evolution of the position of $X_{\max}$ as a function of energy (elongation rate) for iron and proton induced air showers. Elongation rate of different nuclear species are with nearly constant slope and almost parallel to each other. Shown are the results of detailed simulation performed by the Auger Collaboration using various interaction models.

This is of particular importance in the attempts to relate experimentally measured quantities to mass composition.

C. Main features used for composition studies

On a shower to shower basis, composition studies are particularly difficult because of the intrinsic shower to shower fluctuation of $X_{\max}$ and N_μ. Those fluctuations come from the random nature of the interaction processes (in particular, the position of the first interaction) and from the large spacing and limited sampling size of the detectors. Nevertheless, due to the difference in their cross section with air, showers originating from different primaries can, at least statistically, be distinguished.

In a real situation, where the composition evolves with energy, one observes changes in the elongation rate that are not compatible with a single species because the rate of change is either too large when composition evolves from heavy to light (violating the elongation rate theorem) or too small going from light to heavy.

From the superposition principle, we have seen that distinct primaries will show up as parallel lines of constant slopes in an elongation rate plot. Detailed simulations qualitatively confirm this principle although the lines are neither totally parallel nor exactly of constant slope. Those features are model dependent as they depend on the inelasticity treatment of the cross section and on the leading (the fastest) particle effect together with the evolution of the rate of change of the cross section with energy which is not measured at the highest energies (above 10^{17} eV). Nevertheless, for a detector that can measure in each individual cosmic ray event the position of $X_{\max}$ with decent precision (a few tens of g/cm^2 or less), the elongation rate plot provides information about the evolution of cosmic ray composition with energy. It is important to note that both the absolute value of $X_{\max}$ and its rate of change with energy are not the same for the various interaction models that have been developed (Ostapchenko, 2007; Ahn *et al.*, 2009; Pierog and Werner, 2009). Therefore, going from the experimental average value of $X_{\max}$ at a given energy to an average atomic number is strongly model dependent.

Beside the average value of $X_{\max}$ at a given energy, another statistical observable which distinguishes composition and is less model dependent is given by the width of the $X_{\max}$ distribution. In a simple approach, the shower to shower (of the same energy) fluctuations of $X_{\max}$ are dominated by the fluctuations of the first interaction point X^0. X^0 follows an exponential distribution. As in Heitler's model, we take the 50% energy loss distance, $\lambda_I \ln 2$ for the characteristic length in the distribution of X^0. At 10^{18} eV, this approach gives, according to Eq. (5), a fluctuation of X^0 for protons of 60 g/cm^2, which is in good agreement with simulation results. For an iron nucleus of the same energy, the lower energy of individual nucleons and the strict application of the superposition principle give $\mathrm{RMS}[X^0] = \lambda_I(10^{18}\ \mathrm{eV}/56) \times \ln 2/\sqrt{56} \simeq 14$ g/cm^2. This is in reasonable agreement with detailed simulations, which give a value between 20 and 24 g/cm^2. Leading fragment effect (violating the superposition principle) and fluctuation in subsequent interactions also play a role in the case of heavy nuclei. Here the fluctuations of X^0 give only a lower bound to the fluctuations of $X_{\max}$.

On an individual shower basis, the identification of the primary cosmic ray is experimentally more challenging, but not impossible. Because of the fast rate of growth of the particle number in the cascade and the large phase space available for secondaries at each interaction, the particle fluxes converge rapidly towards distributions that are independent of the primary particle type. This is especially true around the maximum development of the shower. Electromagnetic and muon fluxes are adequately described by a Gaisser and Hillas (1977) type function [as in Eq. (15)] whose ''age'' parameter describing their stage of development is derived from $X_{\max}$ and whose normalizations are given by the primary energy and the muon fraction. This universality property was recently discussed by Chou *et al.*(2005) and studied by Giller *et al.* (2004); Nerling *et al.* (2006); Schmidt *et al.* (2007); Apel *et al.* (2008); Schmidt *et al.* (2008); Lipari (2009).

Air-shower universality states that the longitudinal development of the electromagnetic component of nuclei-induced air showers can be completely described in terms of two parameters, the primary nucleus energy and the shower age. Shower universality tells us that all information about the primary particle can in principle be recovered from the measurements of three parameters. While, due to fluctuations, it is insufficient to measure only $X_{\max}$ and E^0, efficient separation can be achieved if the muonic content of the shower is also measured. Additional information on the first interaction cross section can also be retrieved by fitting an exponential to the right-hand side (deeper side) of the $X_{\max}$ distribution in fixed energy bins.

Unlike the electromagnetic component of EAS, muons reaching ground level still carry information about their production point along the shower axis. Because they mostly travel in straight lines without much scattering, they dominate the early part of the signal at the ground. Therefore, detectors with good timing capabilities can construct composition sensitive parameters based on the signal shape either in individual detectors (rise-time parameters) or comparing signals in several detectors (asymmetries and curvature parameters). Even when the absolute muon content cannot be retrieved, these shape parameters provide valuable information characterizing the primary composition.

D. Detection methods

Above 10^{15} eV, the cosmic ray flux drops below a few tens of particle per m^2 and per year. It is no longer possible to detect the incident particles above the atmosphere before they interact. Detectors flying in balloons or satellites that are less than a few m^2 in size must be replaced by ground based instruments that cover up to several thousands of km^2.

From the direct measurement of the incident particle properties, energy, mass, charge, etc., one must revert to the indirect measurement of the EAS produced by the interaction in air. The atmosphere acts as a calorimeter and becomes part of the detection system. As this is not a fully controlled environment, atmospheric conditions must be carefully monitored and recorded along with the air-shower data. All experiments aim at measuring, as accurately as possible, the primary direction (by the relative times of the signals), the primary energy (inferred from the integrated signals densities), and the primary nature or mass (extracted from the signals shapes).

With the exception of fluorescent light from the nitrogen molecules excited along the shower trajectory and the possible microwave emission (P. Gorham *et al.*, 2008), most radiation emitted from EAS are concentrated in the forward direction and cannot be detected far away from the shower axis. Hence the original, and most frequent technique, used to detect UHECR is to build an array of sensors (scintillators, water Cherenkov tanks, muon detectors, Cherenkov telescopes, etc.) spread over a large area. When a cosmic ray event falls within the array boundary, the subsample of detectors placed near enough to the shower axis will observe the radiation reaching the ground. The surface area of the array is chosen according to the incident flux, i.e., the energy range one wants to explore.

Ignoring the remaining fragments of the hadronic cascade, which are concentrated very near the shower core electrons and photons from the EM cascade, muons and forward-beamed Cherenkov light propagate along the shower axis. Particles reaching the ground from the EM cascade are the result of a long chain of interactions, they are constantly regenerated and progress in a diffusive way. Those observed at the ground are produced in the vicinity (a couple of Molière radii or a few 100 m) of the ground detector that measures them. Their time profiles carry little information on the shower development itself, but their density gives information on the primary energy. This radiation is concentrated around the shower axis, but at the highest energies, above 10^{18} eV, particles can be observed up to a couple of kilometers away with detectors of about 10 m^2 in size. Like the EM cascade, muons and (direct) Cherenkov light are concentrated around the shower axis. However, they reach the ground essentially unaltered. Their time profile carries the memory of their production point along the shower axis and can be used to construct composition sensitive parameters.

Fluorescent light is emitted isotropically and hence can be detected with appropriate telescopes tens of kilometers away from the shower axis. The light is emitted proportionally to the number of electrons in the EM cascade and reaches the telescopes essentially unaltered (we neglect the losses due to diffusion). The time profile will then reflect the evolution of the electromagnetic cascade and allows for direct measurement of composition sensitive parameters such as $X_{\max}$. Moreover, because the radiation can be observed far away, a clear lateral view of the shower profile is possible, unlike in the case of a detection close to the shower axis.

1. Air-shower arrays

Air-shower arrays are networks of particles detectors. They cover a surface area in direct proportion to the cosmic rays (CR) flux in the region of the spectra one wishes to study. A few thousands m^2 is enough for the knee region around 10^{15} eV, while thousands of km^2 are necessary for studies near the spectral cutoff at energies above 10^{19} eV. The spacing of the detector is also a function of the energy range of interest. For cosmic rays of energy 10^{18} eV and above, spacing is of the order of 1 km.

The array of detectors counts the number of secondary particles which cross them as a function of time. They

sample the part of the shower which reaches the ground. The incident cosmic ray direction and energy are measured assuming that the shower has an axial symmetry in the transverse shower plane. This assumption is valid for zenith angles up to about 60°. At larger zenith angles, the EM part of the cascade is largely absorbed and the muons start to be bent by the geomagnetic field. Above 75°, the ground pattern shows a clear butterfly shape characteristic of the geomagnetic field effect.

The pioneer work of J. Linsley at Volcano Ranch (Linsley *et al.*, 1961) used an array of 3 m^2 scintillators 900 meters apart covering a total surface area of about 8 km^2. It is with this detector that the first event in the 10^{20} eV range was detected (Linsley, 1963). Scintillator arrays are usually made of m^2 flat pieces of plastic scintillators laid on the ground and connected by cables. They are equally sensitive to all charged particles, thus mostly measure the EM component of the cascade. Particularly simple to use and deploy, they have been quite popular for studies at the highest energies (Linsley *et al.*, 1961; Efimov *et al.*, 1991; Chiba *et al.*, 1992). The aperture of flat scintillator arrays drops quickly with the zenith angle because of the decrease of their effective surface and because of the absorption of the EM component. For accurate measurements, data of scintillator arrays are usually restricted to zenith angles below 45°.

In principle, the measurement of the EM cascade allows for a calorimetric and essentially mass independent measure of the primary cosmic ray energy. However, detector arrays sample the particle densities at a fixed atmospheric depth, which varies from shower to shower because of the variations of the position of $X_{\max}$. This introduces a mass dependent bias in the energy estimates. In practice, the energy calibration of scintillator arrays relies on simulations. This has always been the major difficulty of the technique.

Water Cherenkov tanks have also been successfully used in large cosmic ray arrays. The Haverah Park array, made of Cherenkov tanks of various sizes spread over about 12 km^2, took data for almost 20 years (Lawrence *et al.*, 1991). Heavy, requiring extra pure water with excellent protection against contamination, water Cherenkov detectors are not as easy to deploy as scintillators. However, since the Cherenkov light generated in the water is proportional to the path length of the particle, water tanks are sensitive to both the numerous electrons and photons and the shower muons. On the average, depending on the exact detector geometry, a muon will deposit about 10 times more light than a single 20 MeV electron. Because of their height, water tanks also offer a nonzero effective surface for horizontal showers. Together with the muon sensitivities, this extends the aperture of such arrays to nearly horizontal showers.

Reconstruction of the primary particle parameters is based on timing for the geometry and on the distribution of signal densities as a function of the lateral distance to the shower axis for the energy.

From the position of the different detectors and from the onset of the shower front signal recorded in each of them, one can reconstruct the shower axis and hence the original cosmic ray direction. Precision of one to three degrees are usually obtained given the large base line of the detector spacing (1 km). For charged cosmic rays, this precision is sufficient given the deflection expected from the galactic coherent and random magnetic field.

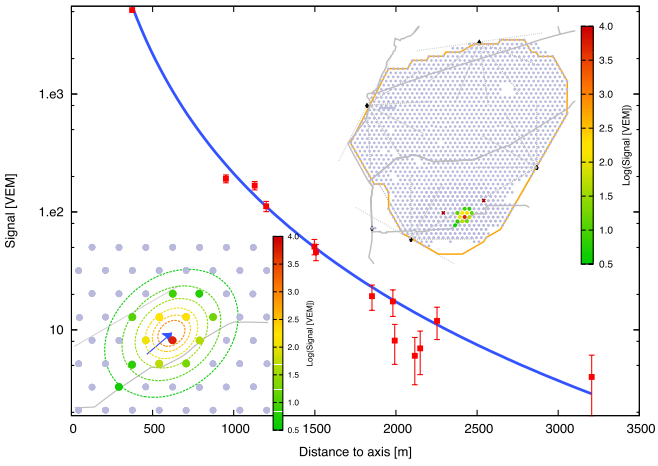

FIG. 5 (color online). Example of detection using a surface array. The upper right inset shows the whole Auger surface array and the footprint of the shower, each dot represents a detector and the spacing between them is 1.5 km. The lower inset shows details of this footprint with the estimated contours of the particle density levels. The curve represents the adjusted LDF (lateral distribution function) and the center point represents the measured densities as a function of the distance to the shower core. From the Auger Collaboration.

For the energy, the detector positions are projected onto the plane transverse to the shower axis and a lateral distribution function (LDF) is adjusted to the measured signals. Hillas (1970) proposed to use the signal at an optimal distance r_{opt} depending on the energy range and the array spacing. At r_{opt}, the sum of the fluctuations from shower to shower and of the statistical fluctuations from particle counting are minimum.

Several LDFs have been used to represent the lateral signal distribution. The Haverah Park experiment used as a LDF the function

$$S(r, \theta, E) = kr^{-[\beta(\theta,E)+r/4000]} \tag{10}$$

for distances less than 1 km from the shower core. Here, r is in meters, θ is the zenith angle, and β can be expressed as

$$\beta(\theta, E) = a + b \sec\theta. \tag{11}$$

The value of β is derived from Monte Carlo simulations and can also incorporate a slow logarithmic evolution with energy. Roughly, $a \simeq 3.5$ and $b \simeq -1.2$ for a vertical value of β under 3. At larger distances (and higher energies), this function has to be modified to take into account a change in the rate at which the densities decrease with distance. This is due to the increasing dominance of muons over electrons at large core distance, since muons have a flatter LDF. A more complicated form was used by the AGASA group (Yoshida *et al.*, 1995). However, the principle remains the same. Figure 5 is an example, taken from the Auger Collaboration public event display[1] of the footprint of an air shower on the ground together with the reconstruction of the LDF.

Once the attenuation of the signal due to the zenith angle is accounted for, an estimator of the energy is obtained from the corrected density at r_{opt} in the form

[1] http://auger.colostate.edu/ED/

$$E = kS(r_{\rm opt}, \theta_{\rm ref})^{\alpha}, \tag{12}$$

where α is a parameter of order 1.

To reconstruct the primary parameters, a minimum of three detectors with signal is necessary. The spacing between those detectors will determine the array energy threshold. For a vertical shower, the 500 m spacing of the trigger stations in Haverah Park corresponds to a threshold of a few 10^{16} eV, while the 1.5 km separation of the Auger Observatory stations gives a few 10^{18} eV.

Ground arrays do not have direct access to the position of the shower maximum and this is a strong limitation to this technique for primary identification. Muon counting can be done with buried detectors or, in favorable conditions, when the EM to muon signal ratio is not too large, by counting muon spikes in the recorded traces of water Cherenkov tanks. Additionally, when the EM to muon signal ratio is not too large, the early part of the traces is dominated by the muon signal and its time evolution carries information on the position of the shower maximum. This is always less sensitive than a direct measurement of $X_{\rm max}$ as done by the fluorescent technique. Only a combination of both measurements, $X_{\rm max}$ and N_{μ}, can give a shower by shower composition indication.

Alternative techniques trying to exploit the emission of EAS in the radio band have also been explored. Between 1967 and 1973, extensive studies took place in the 10–100 MHz band. However, the technique was judged unworthy, in particular, due to the strong beaming of the emission in the forward direction and the poor signal to noise ratio achieved at the time (Allan, 1977). With the progress in fast digital electronics and low noise amplifiers, the interest for the technique was revived. These new efforts (Ardouin *et al.*, 2006; Haungs *et al.*, 2009) aim at replacing ground array detectors with radio antennas, which are both less expensive and easy to deploy. In addition, the radio signal, which propagates essentially nonaltered from its source to the detector, carries information on the shower evolution. Important progress has been made and the radio signal in the VHF band has been showed to be dominated by the geosynchrotron emission of the electrons and positrons of the EM cascade. However, detection of the transient signal in those frequencies is still a challenging task, even more so given the very tight lateral distribution of the radio signal. Recent measurements confirm the strong concentration of the signal in the forward region with an exponential decrease from the core with a characteristic distance of order 150–200 m. However, they demonstrated the possibility to reconstruct the CR direction with reasonable accuracy (Revenu *et al.*, 2009). Progress regarding this technique and its exploitation at the highest energies is expected in the coming years as important research and development efforts are being pursued (van den Berg, 2009a).

2. Cherenkov light

According to Brennan and Chudakov (Brennan *et al.*, 1958; Chudakov *et al.*, 1960), the Cherenkov light emission from the charged particle component of an air shower can provide an integrated measurement of the longitudinal development. The Cherenkov intensity is proportional to the primary energy, while the slope of the lateral distribution is related to the depth of maximum shower development. Thus, if one samples the Cherenkov lateral distribution, i.e., the photon density as a function of the distance from the air-shower core, it is possible to estimate both the primary energy and composition.

From air-shower simulations, it was shown (Patterson and Hillas, 1983) that at distances larger than about ~150 m from the shower core, the density of Cherenkov light is proportional to the primary energy, but essentially independent of its nature. The light profile close to the core is sensitive to the depth of penetration of the shower in the atmosphere, which correlates with the primary cross section.

Experimental setups exploiting the Cherenkov light for EAS are usually associated with standard particle detector arrays (Efimov *et al.*, 1991; Cassidy *et al.*, 1997; Dickinson *et al.*, 1999; Arqueros *et al.*, 2000; Swordy *et al.*, 2000; Chernov *et al.*, 2006). Cherenkov light is also used in CR observation at other energies. For a complete overview and history of Cherenkov detection of cosmic rays, see (Lidvansky, 2005).

In Cassidy *et al.* (1997), Arqueros *et al.* (2000), and Chernov *et al.* (2006) the experimental setups consist of open photomultipliers fitted with Winston cones and looking upward in the sky. The largest array composed of 150 of such sensors distributed about every 40 m was installed on the Fly's Eye site in Dugway (Utah, USA) together with the CASA and CASA-MIA (Borione *et al.*, 1994) detector arrays. Near the core, the lateral distribution of Cherenkov light was shown to be exponential as in Patterson and Hillas (1983). The CASA-BLANCA group (Fowler *et al.*, 2001) used a two component function, which matches both their real and simulated data. The function is exponential in the range 30–120 m from the shower core and a power law from 120 to 350 m. It has three parameters: a normalization C_{120}, the exponential "inner slope" s, and the power law index β

$$C(r) = \begin{cases} C_{120} e^{s(120\ \mathrm{m}-r)}, & 30 < r \le 120\ \mathrm{m} \\ C_{120}(r/120\ \mathrm{m})^{-\beta}, & 120 < r \le 350\ \mathrm{m} \end{cases}. \tag{13}$$

The primary energy depends primarily on C_{120}, the Cherenkov intensity 120 m from the core. Detailed simulation of the shower and of the detector can be used to derive the relation between those two quantities. Hadronic models predict that C_{120} grows approximately as $E^{1.07}$, because in a hadronic cascade the fraction of primary energy directed into the electromagnetic component increases with energy.

Similarly, the slope of the exponential can be related to the shower maximum using simulations. The relation between the two is essentially linear (Arqueros *et al.*, 2000; Fowler *et al.*, 2001).

In the low duty cycle (Cherenkov detector can only be operated on clear dark nights), the short core distance up to which the inner slope parameter can be used to estimate $X_{\rm max}$ and consequently the small spacing within units made this technique inappropriate to study EAS beyond an energy of about 10^{17} eV. The success of the fluorescent detection technique contributed to the decline in the interest for this technique at the highest energies.

3. Fluorescent light

The charged secondary particles in EAS produce ultraviolet light through nitrogen fluorescence. Nitrogen molecules,

excited by a passing shower, emit photons isotropically into several spectral bands between 300 and 420 nm. As discussed above, a much larger fraction of UV light is emitted as Cherenkov photons. But this emission is strongly beamed along the shower axis and usually considered as a background to fluorescent detection.

The first fluorescent detector assembled for UHECR detection was laid down by Greisen and his team in the mid 1960s (Bunner, 1967; Bunner *et al.*, 1967). Small mirrors and the atmospheric conditions did not allow one to record signals from EAS. Detectors were built in the late 1970s by a group at the University of Utah and tested at the Volcano Ranch ground array (Bergeson *et al.*, 1977) while the first detection of fluorescent light from UHECR was made by Tanahashi and collaborators (Hara, *et al.*, 1970). Later on, a fully functional detector was installed at Dugway (Utah) under the name of Fly's Eye (Baltrusaitis *et al.*, 1985). It took data from 1981 until 1993 and fully demonstrated the extraordinary potential of the technique. The highest energy shower ever detected (320 EeV) was observed by this detector. An updated version of this instrument, the High-Resolution Fly's Eye, or HiRes (Boyer *et al.*, 2002), ran on this same site from 1997 until 2006.

The fluorescent yield is 4 photons per electron per meter at ground level pressure. Under clear moonless night conditions, using square-meter scale telescopes and sensitive photodetectors, the UV emission from the highest energy air showers can be observed at distances in excess of 20 km from the shower axis. This represents about two attenuation lengths in a standard desert atmosphere at ground level. Such a large aperture, instrumented from a single site, made this technique a very attractive alternative to ground arrays despite a duty cycle of about 10%.

Fluorescent photons reach the telescopes in a direct line from their source. Thus, the collected image reflects exactly the development of the EM cascade (see Fig. 6). From the fluorescent profile, it is in principle straightforward to obtain the position of the shower maximum and a calorimetric estimate of the primary energy. In practice, a number of corrections must be made to account for the scattering and the absorption of the fluorescent light. Also, pollution from other sources, such as the Cherenkov component, which can be emitted directly, or diffused by the atmosphere into the telescope, must be carefully evaluated and accounted for. A constant monitoring of the atmosphere and of its optical quality is necessary together with a precise knowledge of the shower geometry for a careful account for those corrections.

The shower geometry as viewed from a fluorescent telescope is depicted in Fig. 7. It is defined by the shower detector plane (SDP), the distance of closest approach R_p, the time t_0 along the shower axis at the distance of closest approach, and the angle χ_0 within the SDP between the ground plane and the shower axis. This geometry is usually reconstructed in two steps. First, the SDP is determined. Next, the arrival time t_i of the signal in each pixel in the direction of SDP χ_i is used to determine χ_0, R_p, and t_0 from (Baltrusaitis *et al.*, 1985)

$$t_i = t_0 + \frac{R_p}{c}\tan\left(\frac{\chi_0 - \chi_i}{2}\right). \tag{14}$$

One important property of this equation is that unless the angular velocity in the camera and its rate of change can be measured, there is a degeneracy between the impact parameter R_P and the angle χ_0. This degeneracy leads to poor pointing resolution—the three parameters defining the shower geometry cannot be constrained accurately (Sommers, 1995). The situation can be improved using fast electronics to achieve a good precision on t_i and for those showers with sufficient track length in the camera (over about 10°). This was first used by the HiRes Collaboration with the HiRes-II detector (Abbasi *et al.*, 2005a). Alternatively, the HiRes Collaboration also developed a profile constrained time fit for the part of its detector not equipped with fast electronic (Abbasi *et al.*, 2005a). Nevertheless, in both cases the geometrical resolution remains at a few degrees. The best option to resolve this ambiguity is to improve the measurements. This can be done in two ways. (A) Using a second telescope viewing the shower from a different position, the intersection of the two SDP will constrain the geometry of the shower axis to within a fraction of a degree. This is called a stereo reconstruction and is the technique used by the HiRes detector. (B) Constrain the t_0 parameter by a direct measurement of the time of arrival of the

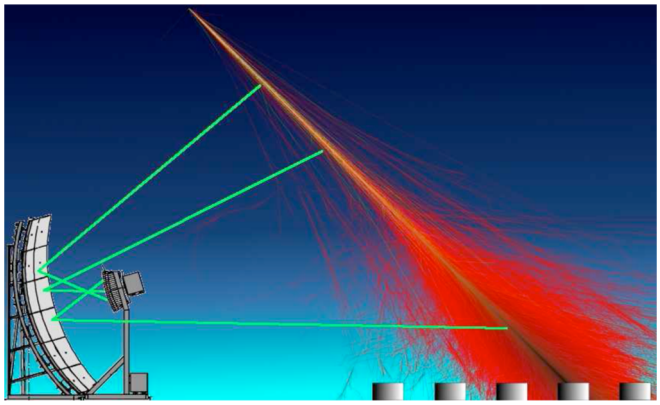

FIG. 6 (color online). Sketch of the detection principles of a fluorescent detector. The fluorescent light emitted by the air shower is collected on a large mirror and focussed onto a camera composed of photomultipliers (Auger Collaboration).

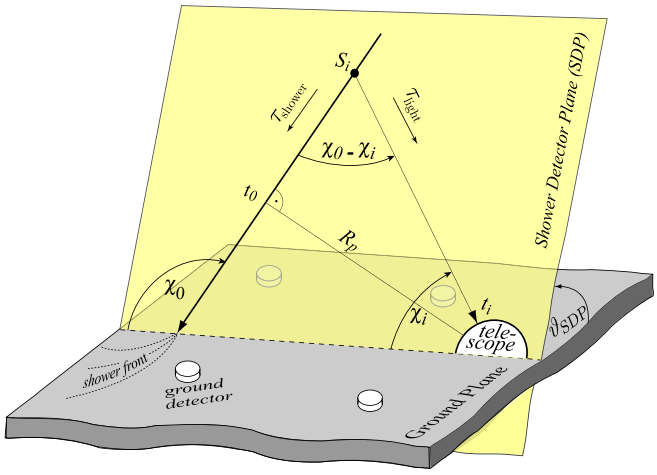

FIG. 7 (color online). Geometry of the detection of an air shower by a fluorescent telescope. From Kuempel *et al.* (2008).

shower at the ground. This is the hybrid technique used by the Auger detector. Again, the geometry can then be constrained to within a fraction of a degree.

Once the geometry has been determined, the fluorescent technique is the most appropriate way to measure the energy of the incident cosmic ray. The amount of fluorescent light emitted along the shower axis is proportional to the number of electrons in the shower. The EAS has a longitudinal development usually parametrized by the four parameter Gaisser-Hillas function giving the size N_e of the shower as a function of the atmospheric depth X (Gaisser and Hillas, 1977)

$$N_e(X) = N_{\max}\left(\frac{X - X_0}{X_{\max} - X_0}\right)^{(X_{\max}-X_0)/\lambda} e^{(X_{\max}-X)/\lambda}. \quad (15)$$

The total energy of the shower is proportional to the integral of this function, knowing that the average energy loss per particle is 2.2 $\mathrm{MeV/g\,cm^{-2}}$.

The Pierre Auger fluorescent reconstruction uses Eq. (15) while the HiRes group has used both the Gaisser-Hillas form and a three-parameter Gaussian in age (Abu-Zayyad *et al.*, 2001). Alternatively, analytic shower theory led to yet another form popularized by Greisen (1956). In a recent study (Matthews *et al.*, 2010), it was shown that the introduction of the profile full width at half maximum (FWHM) and its asymmetry (defined by the ratio of the left width at maximum to the FWHM) could unify the parametrization of all three profile functions. Greisen and Gaisser-Hillas profiles are shown to be essentially identical while Gaussian in age profile only differ at the very early and very late development stages of the cascade.

Beside the corrections arising from the experimental conditions discussed above, the energy transported by the neutral particles (neutrinos), the hadrons interacting with nuclei (whose energy is not converted into fluorescence) and penetrating muons, whose energy is mostly dumped into the Earth, must also be accounted for to estimate properly the primary CR energy. This missing energy correction is calculated using detailed simulations and varies with energy, composition, and the interaction model used. It is about 20% at 10^{18} eV for iron (10% for proton) and about 12% at 10^{20} eV (6% for protons). Variations from one model to another are of about 50% (Pierog and Werner, 2007).

Despite the fact that fluorescent measurements give direct experimental access to the position of $X_{\max}$, the separation of hadronic primaries according to their mass cannot be done on a shower by shower basis because of the intrinsic fluctuation of this parameter. One must look for statistical means of studying the chemical composition and/or use additional information such as the muon content that can be provided by particle detectors as in the hybrid detection system.

Statistical methods relying on the measured fluorescent profile only are based on the elongation rate plot, or the RMS($X_{\max}$) plot. In the former, one calculates the average value of $X_{\max}$ from a set of showers of the same energy and plot it as a function of energy. In the latter, it is the width of the distribution of $X_{\max}$ of shower of the same energy that is plotted against energy. Those measurements are discussed in Sec. VII.

III. GALACTIC COSMIC RAYS

A. Origin of the galactic cosmic rays

Galactic cosmic rays are believed to be accelerated at supernova remnants. This idea was justified by Ginzburg and Syrovatskii (1964) through simple and powerful arguments based on the energetics of supernova remnants. If only 5% to 10% of the kinetic energy of supernova remnants is converted to accelerated cosmic rays, this would provide the energy of all galactic cosmic rays.

Supernova remnants are attractive candidates for cosmic ray acceleration because they have higher magnetic fields than the average interstellar medium. They are also large and live long enough to carry the acceleration process to high energy. The acceleration mechanism is believed to be stochastic acceleration at supernova blast shocks.

The idea of stochastic particle acceleration was first developed by E. Fermi who proposed (Fermi, 1949) to use the charged particle interactions with interstellar clouds to accelerate cosmic rays.

The shock ahead of the expanding supernova remnant (SNR) is formed because the expansion velocity of the remnant is much higher than the sound velocity of the interstellar medium. Shock acceleration is much faster than the original Fermi acceleration mechanism. The energy gain is proportional to β (first-order acceleration) rather than to β^2 [second-order (Fermi) acceleration] where β is the velocity of the magnetic cloud or the blast shock velocity in terms of c. In addition, the supernova shock velocity is much higher than the average velocity of molecular clouds. As a result, shock acceleration is orders of magnitude more efficient and correspondingly much faster. The shock acceleration scenario was suggested in the late 1970s by Axford *et al.* (1977), Krymsky (1977), Bell (1978), and Blandford and Ostriker (1978). It is under continuous development (Drury, 1983; Blandford and Eichler, 1987; Jokipii, 1987; Jones and Ellison, 1991; Bell, 2004). The prediction is for a flat, E^{-2} cosmic ray spectrum in acceleration in nonrelativistic shocks and for a steeper $E^{2.2-2.3}$ spectrum at acceleration in highly relativistic shocks (Achterberg *et al.*, 2001b).

The maximum energy that a charged particle could achieve is then expressed as a function of the shock velocity and extension and the value of the average magnetic field as

$$E_{\max} = \beta ZeBr_S, \quad (16)$$

where β is the shock velocity in terms of the speed of light, r_S is the shock radius, and Ze is the particle charge. Equation (16) is valid during the period of the free expansion of the supernova remnant when the shock velocity is constant. During the Taylor-Sedov phase, when the shock has collected enough interstellar matter to start slowing down, the maximum energy starts decreasing as the radius is only proportional to the time to the power of 2/5. More recent detailed calculations (Berezhko, 1996) derive maximum energy values close to 5×10^5 GeV and even higher in some cases (Ptuskin *et al.*, 2010). An important component of the expression for $E_{\max}$ is its dependence on the particle charge Z. This means that a fully ionized heavy nucleus of charge Z could achieve Z times higher energy than a proton.

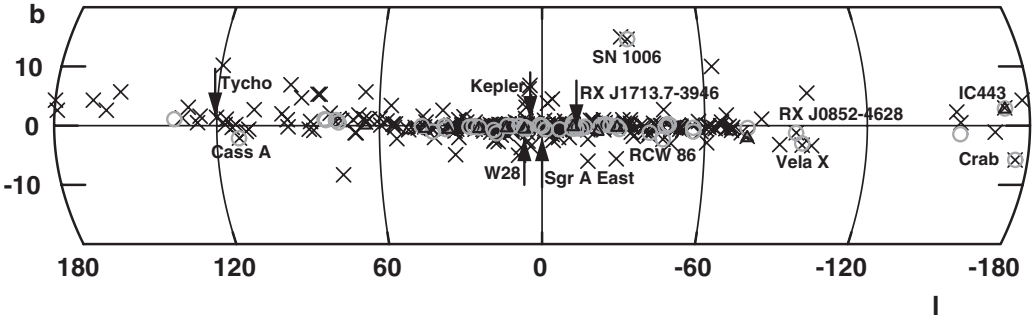

FIG. 8. Comparison of the positions of supernova remnants (x's) with GeV (Fermi/LAT: triangles) and TeV (circles) gamma-ray sources.

Since cosmic rays scatter in the galactic magnetic fields, we cannot observe them coming from particular sources. The only way we can study their acceleration sites is by observing the neutral particles, gamma rays, and neutrinos generated by their interactions during acceleration. There are two epochs in supernova remnant evolution when one can expect γ-ray and neutrino emission. One of them is shortly after the supernova explosion, when the density of the expanding supernova envelope is very high and thus contains enough of a target for hadronic interactions. The emission will continue for about 2 to 10 years (depending on the mass distribution and expansion velocity of the supernova remnants) until proton energy loss on inelastic interactions becomes dominated by the adiabatic loss due to the SNR expansion. The γ-ray emission will fade for a long time, until the SNR reaches the Sedov phase, when most of the galactic cosmic rays are accelerated. Since this phase lasts for more than 1000 years, there should be many supernova remnants that are gamma-ray sources.

The modern expectations of the γ-ray emission of mature supernova remnants was developed by Drury *et al.* (1994). The assumption is that cosmic rays at the source have a much flatter spectrum than the one observed at Earth as acceleration models suggest. As an example of the expectations from a concrete SNR (Drury *et al.*, 1994), apply the calculation to the Tycho (1572) supernova remnant, which should be close to the Sedov phase. One can take the average supernova energy and density from different estimates $E_{\rm SN} = 4.5 \pm 2.5 \times 10^{50}$ ergs, matter density $n_1 = 0.7 \pm 0.4$ and estimate the γ-ray flux for conversion efficiency $\theta = 0.2$ and distance $d = 2.25 \pm 0.25$ kpc. The expected flux is

$$F(>E_\gamma) = \simeq 1.2 \times 10^{-12} \left(\frac{E_\gamma}{\rm TeV}\right)^{-1.1} \ {\rm cm}^{-2}\,{\rm s}^{-1}. \qquad (17)$$

The detection of such a flux is easily within the capabilities of the last generation of γ-ray Cherenkov telescopes.

Figure 8 compares the positions of supernova remnants from the (Green, 2009) catalog with the positions of GeV gamma-ray sources from the Fermi/LAT observations (Abdo *et al.*, 2009) and of TeV sources from the TeVCat catalog.[2] One can clearly see several coincidences. There are others that are more difficult to find by eye because there are so many supernova remnants close to the Galactic center at very low galactic latitude. Many of the TeV sources come from the HESS survey of the galactic plane of galactic longitudes from $-30°$ to $30°$ and latitudes below $3°$ (Aharonian *et al.*, 2006b). The names of some of the SNR that emit TeV γ rays are indicated in the figure whenever possible. There are though no gamma rays coming from the Tycho supernova remnant.

The number of direct coincidences of the supernova remnant locations with the directions of the gamma-ray sources is relatively small. What is the fraction of the supernova remnants that are γ-ray sources and thus are cosmic ray accelerators? The small fraction of γ ray producing SNRs creates doubts that galactic cosmic rays are generated at these objects. This may be true, but the HESS group put together an alternative explanation of this effect in their study of the galactic ridge (Aharonian *et al.*, 2006a). Hadronic gamma-ray production is only possible when the matter density of the medium is much higher than 1 cm^{-3}. A very likely gamma-ray production site is the location of dense clouds of matter close to an acceleration site of cosmic rays. HESS observed that the peaks of the γ-ray emission from the region of the Galactic center ridge, after subtraction of known sources, coincide with the positions of molecular clouds with a matter density of hundreds per cm^3. The total amount of mass in these clouds is $(2–4) \times 10^7$ solar masses. In addition, the energy spectrum of the γ rays is about $E_\gamma^{-2.3}$, which is likely to happen close to the cosmic rays acceleration site. This observation may explain the fact that many sources of TeV γ rays do not exactly coincide with the positions of SNR where the cosmic rays that produce them are accelerated, rather with close by molecular clouds. Higher energy cosmic rays diffuse faster away from their sources. For this reason, it is possible that a molecular cloud could be a source of TeV γ rays before it becomes a strong source of GeV gamma rays.

TeV γ rays have been detected from the Crab nebula and the supernova remnants SN1006, Cas A, RX J1713.7-3946, RX J0852.0-4622, W28, W48, RCW 86, and others. The Crab nebula is the standard candle in TeV γ-ray astronomy; it has a steady flux which is used to measure the fluxes of other sources. The models that explain best its gamma-ray emission do not involve hadronic interactions. They are electromagnetic models that rely on electron acceleration and the inverse Compton process.

B. Energy spectrum and composition at the knee

The energy range in which the cosmic ray spectrum changes its slope is called "the knee." Its existence was

[2]http://tevcat.uchicago.edu

first suggested by the Moscow State University group (Kulikov and Khristiansen, 1958) on the basis of their air-shower data. Many groups have studied the knee region and the change of the cosmic ray spectrum is well established. Up to an energy of 10^6 GeV, the spectrum of all cosmic ray nuclei is a power law with differential spectral index α of 2.70–2.75. The spectral index increases by $\Delta\alpha$ of about 0.3 above the knee. A flattening of the spectral index has been detected (Ahn *et al.*, 2010; Panov *et al.*, 2011) just before the knee.

There is no lack of theoretical ideas about the origin of the knee. Peters (1959) suggested that the knee is a rigidity-dependent effect. Rigidity R is the ratio of the particle momentum to its charge. It could be related to the maximum rigidity that can be achieved in acceleration processes or to rigidity-dependent escape of the cosmic rays from the Galaxy. Rigidity-dependent effect is an attractive idea. We know that heavy charged nuclei can achieve Z times higher energy at acceleration. So a natural assumption could be that at the approach to the knee cosmic ray sources cannot accelerate protons to higher energy. Then the next nucleus, He, takes over and the process continues in order of charge until at some higher energy galactic cosmic rays contain only iron nuclei. Mostly, the common nuclei of H, He, C, O, Si, Mg, and Fe are represented in the cosmic ray spectrum.

Figure 9 shows a very simple flux model with rigidity dependence. It uses the spectrum and composition at low energy and extends it to high energy with exponential cutoff in rigidity at 10^7 GV. The thin lines show the contribution of different nuclear groups to the all-particle spectrum. The proton spectrum turns over at 10^7 GeV and those of heavier nuclei turn over at energies of $Z \times 10^7$ GeV. At energies above 10^8 GeV, there are only heavy, high Z, nuclei in the cosmic ray flux. The end of the modeled spectrum is where the Fe component is also exponentially cut off.

This simple model agrees well with the measurements of the Kascade (Antoni *et al.*, 2005) and Tibet III (Amenomori *et al.*, 2008) air-shower arrays. The normalization of these experiments is slightly different, which affects both the magnitude of the flux when it is multiplied by $E^{2.75}$ and the position of the knee. The analysis of air-shower data depends on the hadronic interaction models used in the simulations. The dependence is stronger for the Kascade experiment, which is located much lower in the atmosphere. Tibet III is close to the depth of shower maximum $X_{\max}$, where the ratio between shower electrons and muons is at its maximum. This ratio decreases with the atmospheric depth, but predictions depend strongly on the hadronic interaction model. The normalization of both spectra, however, depends on the cosmic ray composition.

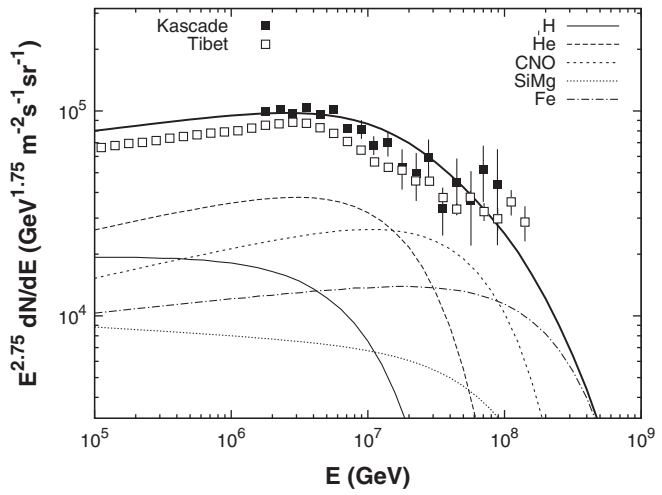

FIG. 9. A simple model of the knee, which extends the low energy spectrum and composition to high energy with an exponential cutoff at 10^7 GeV. The model is normalized to the all-particle flux measured by the Kascade experiment (Antoni *et al.*, 2005), which is shown with full squares. The measurements of the Tibet III experiment (Amenomori *et al.*, 2008) is shown with empty squares.

The cosmic ray composition estimated from air-shower data is usually presented as the average value of the logarithm of the primary particle mass $\langle \ln A \rangle$. Different composition estimates are not in very good agreement. As an illustration, Fig. 10 presents the results from the analyses of data from the Kascade (Antoni *et al.*, 2005) and EAS-TOP (Aglietta *et al.*, 2004) experiments. Both composition results come from the ratio of the shower muon density at predefined distances from the shower core as a function of the total number of electrons in the shower N_e. These two measurements are in a fairly good agreement.

Figure 10 shows that the composition becomes significantly heavier with increasing energy. It is fully consistent with the rigidity-dependent idea. The simple composition model, however, does not describe the data well. It predicts heavier composition at 10^6 GeV and lighter composition at 10^8 GeV. A better model would require a different low energy composition and possibly lower maximum rigidity.

Although the majority of the experiments measure a cosmic ray composition that becomes heavier between 5×10^6 and 10^7 GeV, it is difficult to draw a definite conclusion about the exact changes of the cosmic ray spectrum and composition at the knee. All experiments agree that the cosmic ray spectrum steepens above 10^6 GeV. The exact position of the spectral change and the width of the transition region are not yet well determined. The composition studies,

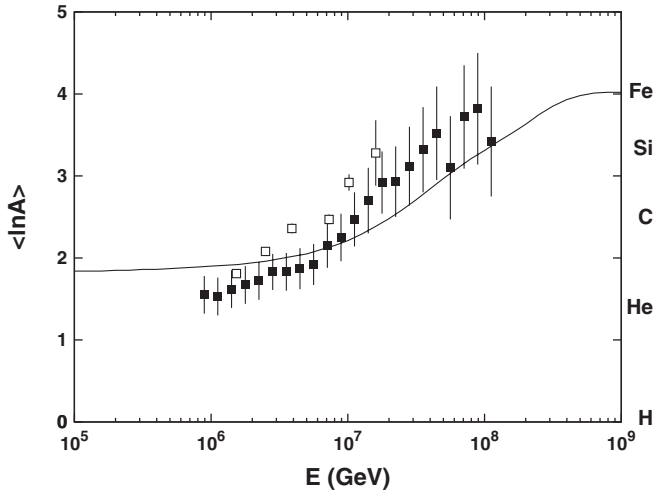

FIG. 10. Results from studies of the cosmic ray composition in the region of the knee compared to the predictions of the simple model presented in Fig. 9.

both with surface air-shower arrays and with optical detectors, indicate a change in the average mass of the cosmic ray nuclei after the steepening of the spectrum, once again with large uncertainty in the energy range and shape. All of these numerous data sets are consistent with rigidity-dependent effects, either in the cosmic ray acceleration or in their propagation. This second scenario assumes that lower rigidity nuclei are contained in the Galaxy longer.

IV. ORIGIN OF COSMIC RAYS UP TO 10^{20} eV

The question of how to accelerate cosmic rays up to 10^{20} eV has been pending since their very first observation in the 1960s. More than 30 years later, in the mid 1990s, the data collected by the AGASA and HiRes experiments generated a profusion of ideas. Some of them aimed at an explanation of the possible absence of a cutoff above 3×10^{19} eV and the lack of visible astrophysical sources. All ideas tried to find a solution to the basic problem of how to transfer efficiently a macroscopic amount of energy, of the order of 20 Joules, to a microscopic particle.

To circumvent this difficulty, one of the main axis of research was the mere suppression of the accelerator itself. Particles are not accelerated as such, but directly produced, via the decay of some supermassive relic of the Big Bang, or by the collapse of topological defects, with energies in excess of 100 EeV. While attractive from a theoretical point of view, these models had the disadvantage of replacing the acceleration problem with the question of the nature and existence of such top-down sources.

With the observational facts collected by HiRes and Auger in the past decade, the situation has been greatly clarified. A cutoff in the high energy end of the spectrum is clearly visible and the limits on the fraction of photons and on the flux of high energy neutrinos have strongly reduced the interest in the top-down models. On the other hand, the possibility of a dominant iron component in the very end of the energy spectrum decreases by a factor of 26, the hard conditions placed on ''standard'' bottom-up cosmic accelerators to reach the 100 EeV barrier.

Nevertheless, after many decades of investigation, the problem has not been solved, and even the extragalactic nature of the sources above 3 EeV has been challenged (Wick *et al.*, 2004),(Calvez *et al.*, 2010). In the following, we briefly review some of the necessary conditions for the acceleration of UHECR at astrophysical sites and enumerate some possible candidates. We also review the main characteristics of the top-down models. More details on this subject can be found in the recent review of Kotera and Olinto (2011).

A. Possible acceleration sites

Acceleration at astrophysical sites may occur principally through two distinct mechanisms: diffusive shock acceleration, based on the Fermi mechanism, and one shot acceleration in very high electric field generated by rapidly rotating compact magnetized objects such as young neutron stars.

Diffusive acceleration takes place near shock waves and rely on the repeated scattering of charged particles on magnetic irregularities back and forth across the shock. In the case of nonrelativistic shock velocities, the energy gain at each crossing is of the order of $\Delta E \sim E$. To reach energies above 1 EeV, large acceleration regions and/or highly relativistic blast waves are necessary. In the case of relativistic shock, the energy gain reaches $\Gamma_s^2 E$ where Γ_S is the shock bulk Lorentz factor. Such gain appears, however, to be limited to the first crossing (Achterberg *et al.*, 2001a).

One of the principal advantages of the diffusive shock acceleration mechanism is that it naturally provides a power law spectrum whose predicted index γ is within the range of the experimental measurements. Depending on the exact geometry of the shock and on its relativistic nature, the combination of the energy gain per crossing and of the escape probability leads to a power law index of exactly 2 for the case of a strong nonrelativistic shock in an ideal gas and to indexes between 2.1 and 2.4 for relativistic shocks.

Hillas (1984) summarized the conditions on potential acceleration sites using a relation between the maximum energy of a particle of charge Ze and the size and strength of the magnetic field of the site

$$E_{\max} = \beta Ze\left(\frac{B}{1\ \mu\mathrm{G}}\right)\left(\frac{R}{1\ \mathrm{kpc}}\right)\ \mathrm{EeV},$$

where β represents the velocity of the accelerating shock wave or the efficiency of the accelerator.[3] We show in Fig. 11 the now famous Hillas plot illustrating this condition.

Looking at the Hillas diagram, one sees that only a few astrophysical sources satisfy this necessary, but not sufficient, condition. Among the possible candidates are neutron stars and other similar compact objects, large-scale shocks due to merging galaxies or clusters of galaxies, the core and jets of AGN, hot spots of Fanaroff-Riley class II (FR-II) radio galaxies, and processes associated with GRB.

AGN have long been considered as potential sites where energetic particle production might take place (Ginzburg and Syrovatskii, 1964; Hillas, 1984). AGN jets have dimensions of the order of a fraction of a parsec with a magnetic field of the order of a few Gauss (Halzen and Zas, 1997). These parameters could in principle lead to a maximum energy for protons of a few tens of EeV. Similarly, AGN cores with a magnetic field of order 10^3 G and size of a few 10^{-5} parsec can reach about the same energy. However, those maxima, already marginally consistent with acceleration up to 100 EeV, are unlikely to be achieved under realistic conditions. The high radiation field around the central engine of an AGN is likely to interact with the accelerated protons while energy losses due to synchrotron radiation, Compton processes, and adiabatic losses will also take place. The situation is worse for nuclei that will photodisintegrate even faster. Such processes may lead to a maximum energy of only a small fraction of EeV (Bhattacharjee and Sigl, 2000). To get around this problem, the acceleration site must be away from the active center and in a region with a lower radiation density, as in the terminal shock sites of the jets, a requirement possibly fulfilled by FR-II galaxies.

[3]In the case of a relativistic shock, the bulk Lorentz factor Γ_s enters the right-hand side of this equation (Achterberg *et al.*, 2001a).

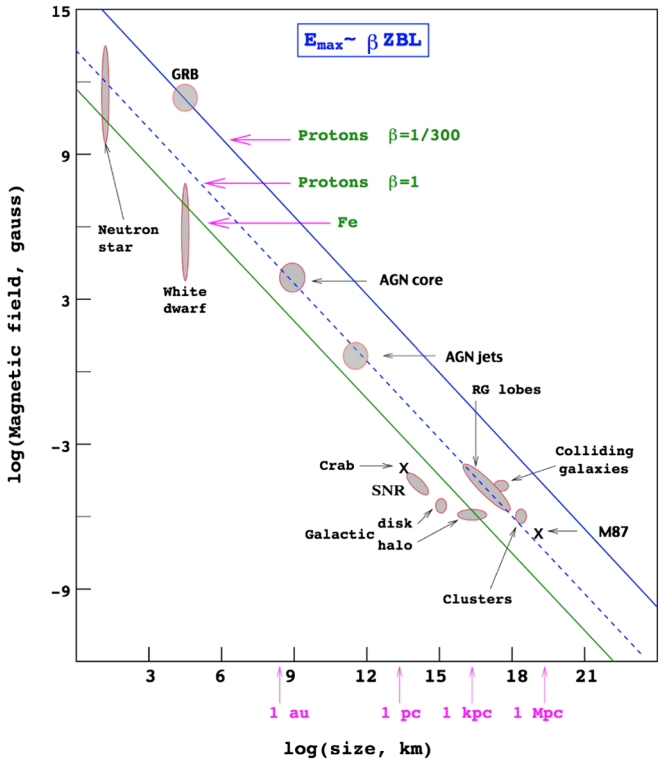

FIG. 11 (color online). Hillas plot for candidate acceleration sites, relating their size and magnetic field strength. To accelerate a given particle species above 100 EeV objects must lie above the corresponding lines.

The link with GRB and UHECR acceleration was initially made by Waxman (1995), Vietri (1995), and Milgrom and Usov (1995), who pointed out that the observed at the time cosmic ray flux beyond 100 EeV (now estimated to be lower by a factor 3 to 10 after the measurements of Auger and HiRes) is consistent with a scenario in which these particles are produced in GRB's provided that each burst produces similar energies in gamma rays and in high energy cosmic rays. From a phenomenological point of view, based on the gamma-ray observations, bursts can be described by the product of the dissipation of the kinetic energy of a relativistic expanding fireball. The time variability of the phenomena and the compact nature of the source suggest that the expanding wind has a bulk Lorentz factor of a few hundreds, a condition in principle sufficient to accelerate charged particles up to 100 EeV. In a more recent analysis, taking into account the cosmological nature of the GRB distribution, a similar conclusion has been drawn, placing GRB's as one of the prominent sites of cosmic ray acceleration. Note that in such a scenario, UHECR sources are not visible since the detected cosmic rays come from various bursts and reach the Earth long after (10^3 to 10^7 years) the gamma-ray burst itself (Waxman, 2006).

Direct observation of radio galaxies gives us their main characteristics in term of their radio luminosity (10^{39}–10^{44} ergs/sec), their size (10^3–10^6 parsecs), their brightness morphology, and the polarization level of the radio emission. From these parameters, one can indirectly infer their mean magnetic field (of the order of 10–10^3 μG) and kinetic power (10^{42}–10^{47} ergs/sec). However, the exact characteristics of the jets and, in particular, their Lorentz factor, density and composition are still under debate (Massaglia, 2008). Among radio loud galaxies, the Fanaroff-Riley radio galaxies of class II are of particular interest because they combine a very powerful engine and relativistic blast wave (with Lorentz factor of the order 2–10) together with a relatively scarce environment. Hence, in the associated hot spots where the relativistic jet terminates, they not only satisfy the acceleration criterion but also the requirement that the accelerated particle does not lose all of its energy via radiation or interactions on its way out of the source (Rachen and Biermann, 1993). Finally, invoking the sheared jet mechanisms where inductive acceleration can take place at the interface of the central spine and outer flow of the jet, acceleration of UHECR can take place in the jets themselves (Lyutikov and Ouyed, 2007).

B. Exotic top-down models

One way to overcome the many problems related to the acceleration of UHECR is to introduce the existence of a new unstable or metastable supermassive particle. Its decay should produce quarks and leptons, which will result in a large cascade of energetic photons, neutrinos, and light leptons with a small fraction of protons and neutrons. In such a model, no acceleration is required and cosmic rays are emerging directly with ultrahigh energy from the decay cascade, hence their name of top-down models.

For this scenario to produce observable particles above 50 EeV the following conditions must be met:

(i) The decay must occur in recent time, i.e., at distances less than about 100 Mpc.
(ii) The mass of this new particle must be well above the observed highest energy (100 EeV range), a hypothesis well satisfied by grand unification theories (GUT) whose scale is around 10^6–10^7 EeV.
(iii) The ratio of the volume density of this particle to its decay time must be compatible with the observed flux. Two distinct mechanisms may produce such energy release.
(iv) Radiation, interaction, or collapse of topological defects (TD), producing GUT particles that decay instantly:. In those models, the TD are leftovers from the GUT symmetry breaking phase transition in the very early Universe. However, little is known about the phase transition itself and about the TD density that survives a possible inflationary phase, and quantitative predictions are usually quite difficult to rely on.
(v) Supermassive metastable relic particles from some primordial quantum field, produced after the inflationary stage of our Universe: The lifetime of those relics should be of the order of the age of the Universe and must be guaranteed by some almost conserved protecting symmetry. It is worth noting that in some of those scenarios the relic particles may also act as nonthermal dark matter.

In the case of TD, the flux of UHECR is related to their number density and their radiation, collapse, or interaction rate, while in the case of massive relics the flux is driven by the ratio of the density of the relics over their lifetime.

The wide variety of topological defect models together with their large number of parameters makes them difficult to review in detail. Many authors have addressed this field. Among them, let us mention Vilenkin and Shellard (1995) and Vachaspati (1997, 1998) for a review on TD formation and interaction. For a review on experimental signatures, see Berezinsky *et al.* (1998), Bhattacharjee (1998), and Bhattacharjee and Sigl (2000).

Basic principles ruling the formation of TD in the early Universe derive from the current picture on the evolution of the Universe. Several symmetry breaking phase transitions such as $\mathrm{GUT} \Rightarrow H \ldots \Rightarrow \mathrm{SU}(3) \times \mathrm{SU}(2) \times \mathrm{U}(1)$ occurred during the cooling. For those ''spontaneous'' symmetry breakings to occur, some scalar field (similar to the Higgs field generating masses to elementary particles) must acquire a nonvanishing expectation value in the new vacuum (ground) state. Quanta associated to those fields have energies of the order of the symmetry breaking scale, e.g., 10^{15}–10^{16} GeV for the grand unification scale.

During the phase transition process, noncausal regions may evolve towards different states in such a way that at the different domain borders, the Higgs field keeps a null expectation value. Energy is then trapped in a TD, whose properties depend on the topology of the manifold where the Higgs potential reaches its minimum. Possible TDs are classified according to their dimensions: magnetic monopoles (zero dimensional, pointlike); cosmic strings (one dimensional); a subvariety of the previous which carries current and is superconducting; domain walls (two dimensional); textures (three dimensional). Among those, only monopoles and cosmic strings are of interest as possible UHECR sources.

Supermassive relic particles may be another possible source of UHECR (Berezinsky, 1999; Bhattacharjee and Sigl, 2000). Their mass should be larger than 10^{12} GeV and their lifetime of the order of the age of the Universe since these relics must decay now in order to explain the UHECR flux. Unlike strings and monopoles, relics aggregate under the effect of gravity similar to ordinary matter and act as a (nonthermal) cold dark matter component. The distribution of such relics should consequently be biased towards galaxies and galaxy clusters.

Regardless of the details and dynamic of the topological collapse or of the massive particle decay, the cascade that is produced will contain, possibly among many other things, quarks, gluons, and leptons. Those particles will in turn produce far more photons and neutrinos than any type of nucleons. Hence, in all conceivable top-down scenarios, photons and neutrinos dominate at the end of the hadronic cascade. This is the important distinction from the conventional acceleration mechanisms. The spectra of photons and neutrinos can be derived from the charged and neutral pion densities in the jets as

$$\Phi_\gamma^{\pi^0}(E,t) \simeq 2\int_E^{E_{\mathrm{jet}}} \Phi_{\pi^0}(\varepsilon,t)d\varepsilon/\varepsilon$$

$$\Phi_\nu^{\pi^\pm}(E,t) \simeq 2.34\int_{2.34E}^{E_{\mathrm{jet}}} \Phi_{\pi^\pm}(\varepsilon,t)d\varepsilon/\varepsilon,$$

where E_{jet} is the total energy of the jet (or equivalently the initial parton energy). Since $\Phi_{\pi^\pm}(\varepsilon,t) \simeq 2\Phi_{\pi^0}(\varepsilon,t)$, photons and neutrinos should have very similar spectra. These injection spectra must then be convoluted with the transport phenomena to obtain the corresponding flux on Earth. In particular, the photon transport equation strongly depends on its energy and on the poorly known universal radio background and extragalactic magnetic fields (Stanev, 2010). Nevertheless, if top-down scenario dominates the UHECR production above a certain energy, the photon fraction should become very large. However, recent observations, in particular, of the Auger observatory, showed the contrary. This has considerably reduced the possibility for such models to be the source of UHECR.

V. UHECR DETECTORS

A. Older experiments: AGASA

The AGASA (Akeno giant air-shower array) is the largest air-shower array of the previous generation of detectors. AGASA covered 100 km^2. It consisted of 111 scintillator counters of area 2.2 m^2 at an average distance of 1 km from each other. Initially, AGASA was divided in four *branches* that operated individually (Chiba *et al.*, 1992). In 1995, the data acquisition system was improved (Ohoka *et al.*, 1997) and the four branches were unified in a single detector. This increased the effective detector area by a factor of 1.7 to reach 100 km^2.

Each AGASA station was viewed by a 125 mm photomultiplier and had a detector control unit that controlled the high voltage of the photomultiplier tube (PMT), adjusted the gain and recorded the timing and pulse height of every signal. The stations were connected by two optical fibers. One of them was used to send commands to the detector control unit. The other reported to the center triggers, shower data, and monitor data. AGASA operated for more than 12 years.

Muon detectors of sizes from 2.4 to 10 m^2 were installed at 27 of the detector stations. In the Southeast corner of AGASA was the Akeno 1 km^2 array, which has been in operation since 1979. It was a densely packed array with detector separations from 3 to 120 m. Akeno has studied the cosmic ray energy spectrum from 3×10^{14} to 3×10^{18} eV (Nagano *et al.*, 1984).

B. HiRes

The HiRes observatory (see Fig. 12) was a much improved follow-up of the pioneer and very successful fluorescent detector Fly's Eye (Baltrusaitis *et al.*, 1985). Also constructed by the University of Utah, the observatory was comprised of two air fluorescent detector sites separated by 12.6 km (Abbasi *et al.*, 2004; Abbasi *et al.*, 2005c). It was located at the U.S. Army Dugway Proving Ground in the state of Utah at 40.00°N, 113°W, at atmospheric depth of 870 $\mathrm{g/cm}^2$. The two detectors, referred to as HiRes-I and HiRes-II, operated on clear moonless nights with a effective duty cycle for physics data of about 10% typical for fluorescent detectors.

The HiRes-I site (Abu-Zayyad *et al.*, 1999) consisted of 21 telescope units, each equipped with a 5 m^2 spherical mirror and 256 phototube pixels at its focal plane. Each telescope

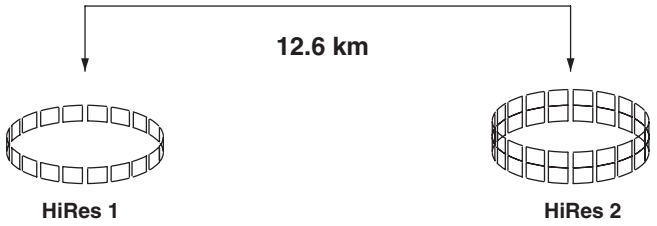

FIG. 12. Sketch of the HiRes fluorescent experiment. Each rectangle represents a fluorescent telescope including a mirror and a camera. Each site of the HiRes detectors has a nearly full azimuth coverage and site 2, which consists of two rings of mirrors covers elevation from 3° to 30° while site 1, with a single ring, covers elevation from 3° to 16°.

covered an elevation range of 14° between 3° and 17° and 360° in azimuth. The phototubes were equipped with sample and hold electronics, which integrated the fluorescent signal within a 5.6 μs window. This was enough to contain the shower signal, but also because of the limited elevation range of the detectors did not allow one to extract the shower geometry from Eq. (14) alone. HiRes-I was in operation from June 1997 up until April 2006.

The HiRes-II site was completed at the end of 1999. Detectors were similar to those of HiRes-I, but with twice as many mirrors organized in two rings covering elevation from 3° to 31° and still 360° in azimuth. Moreover, the HiRes-II phototubes were equipped with fast analog to digital converter electronics which sampled the shower signal every 100 ns. This allowed the reconstruction of the shower geometry from timing alone [Eq. (14)] with a precision of about 5° (Abbasi *et al.*, 2009).

Although the two detectors of HiRes could trigger and reconstruct events independently, HiRes was designed to measure the fluorescent light stereoscopically. Stereoscopic mode allows the reconstruction of the shower geometry with a precision of 0.4° and provides valuable information and cross checks about the atmospheric conditions at the time of the event. HiRes-I and HiRes-II took data until April 2006 for an accumulated exposure in stereoscopic mode of 3460 hours (Abbasi *et al.*, 2009). On the other hand, the ''monocular'' mode had better statistical power and covered a much wider energy range.

In the monocular mode, the geometry of the HiRes-I events was calculated using an expected form of the shower development in addition to Eq. (14) (the profile constrained time fit technique). The shower profile was assumed to be described by the Gaisser-Hillas parametrization, which is in good agreement with HiRes measurements and detailed simulations (Kalmykov *et al.*, 1997; Song *et al.*, 2000; Abu-Zayyad *et al.*, 2001). Significant contamination from the forward-beamed direct Cherenkov light degraded its reliability and tracks with $\chi_0 > 120°$ or with large Cherenkov fraction (as estimated from Monte Carlo simulation) were rejected. Monte Carlo studies showed that the RMS energy resolution for this method was better than 20% only at the highest energies (above $10^{19.5}$ eV).

For monocular reconstruction, from either HiRes-I or HiRes-II, the aperture is energy and composition dependent and must be evaluated by Monte Carlo simulations. The HiRes Collaboration made extensive and detailed simulation of both the atmospheric cascade and their detector and studied the systematics uncertainty in the estimation of the monocular aperture (Abbasi *et al.*, 2007). The stereo aperture was determined by the requirement that the Monte Carlo events trigger both telescopes. Because of the better reconstruction of stereo events, the quality cuts for them were not as strict and the stereo aperture is somewhat higher above energy of $10^{19.7}$ eV (Abbasi *et al.*, 2009). It is smaller for events below $10^{18.5}$ eV.

To determine the correct shower energies, the air fluorescent technique requires accurate measurement and monitoring of the absolute gain of the telescope. In HiRes, two methods of calibration were used. One provided nightly relative calibration and used a laser connected to two mirrors; the other relied on a stable and standard light source and provided monthly absolute calibration. The pulses from a laser were distributed to two mirrors via optical fibers. They provided a nightly relative calibration. Relative phototube gains were stable to within 3.5% and the absolute gains were known to 10% (Abu-Zayyad *et al.*, 2000a). Fluorescent light from air showers is also attenuated by molecular diffusion (Rayleigh) and aerosol scattering. While the former is approximately constant, the aerosol concentration varies rapidly with time. At HiRes (likewise at the Auger observatory), the aerosol content was measured by observing scattered light from steerable laser systems.

The fluorescent yield has been measured by Kakimoto *et al.* (1996), Nagano *et al.* (2004), and more recently by the AIRFLY Collaboration (Ave *et al.*, 2008). A review of those measurements is available in Arqueros *et al.* (2008). The HiRes Collaboration used the fluorescent spectrum compiled by Bunner *et al.* (1967) and normalized it to the yield of Kakimoto *et al.* (1996).

For both HiRes-I and HiRes-II events, the photoelectron count was converted to a shower size at each atmospheric depth, using the known geometry of the shower, and correcting for atmospheric attenuation. The reconstructed profile was integrated over the atmospheric depth. The integral was then multiplied by the average energy loss per particle to give the visible shower energy. A correction (about 10%) for the invisible energy, carried off by nonobservable particles, was applied to give the total shower energy.

The HiRes data contain two events at or above 10^{20} eV, measured at 1.0×10^{20} and 1.5×10^{20} eV. Assuming a purely molecular atmosphere, a lower energy limit of 0.9×10^{20} and 1.2×10^{20} eV was obtained for these events. The flux values were on average 13% lower than the stereo spectrum reported by the Fly's Eye Collaboration (Bird *et al.*, 1993). This difference can be explained by a 7% offset in the energy calibration, well within the uncertainty of the two experiments.

C. Auger

The Pierre Auger Observatory is the largest operating cosmic ray observatory ever built. It is based on the hybrid concept where both fluorescence and surface array detection techniques are used and combined.

The Southern site of the Auger observatory is located in the Pampa Amarilla region (35.1°–35.5° S, 69.0°–69.6° W, and

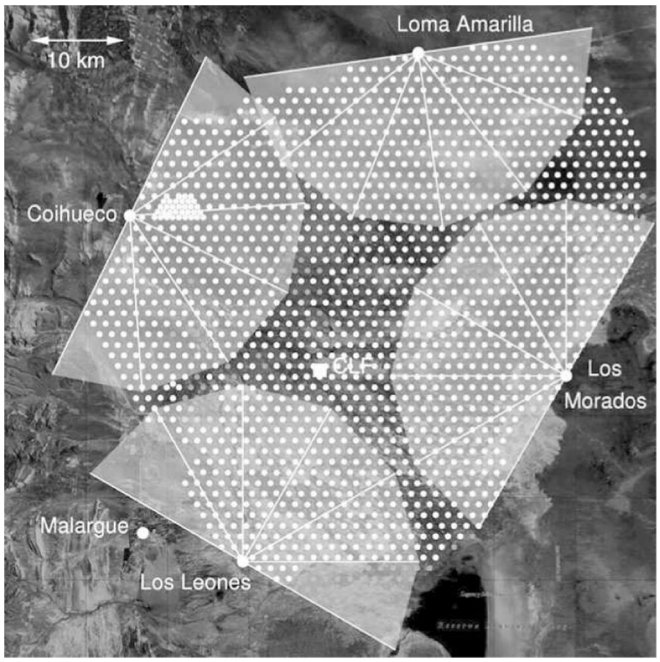

FIG. 13. The Pierre Auger observatory at the end of March 2009. Individual white dots represent Cherenkov tanks, while gray ones are unequiped positions. A denser (infill) area is visible in the upper left. Big white dots at the periphery of the array are fluorescent detector sites with the field of view of individual telescope given by the radial white line. Also shown is the Central Laser Facility (CLF) used for FD calibration and atmospheric monitoring purpose.

1300–1400 m above sea level) of the province of Mendoza, Argentina (Abraham *et al.*, 2004). Construction was completed in 2008, but stable data taking started as early as the beginning of 2004 when Auger already had 100 detectors, covering and area in excess of 150 km^2, installed in the field. The arrangement of the detectors is shown in Fig. 13.

1. Surface array

The surface array (SD) of Auger South is composed of 1600 water Cherenkov tanks, distributed on a triangular grid of 1500 m. It covers a total surface area of 3000 km^2. Each tank is equipped with three photomultiplier tubes to measure the Cherenkov light, a data acquisition and front-end electronic card for control and trigger, a solar panel and two batteries for power, a GPS receiver for the time tagging, and a custom radio emitter and receiver for trigger and data transfer (Allekotte *et al.*, 2008). A central site located on the Southwest corner of the array hosts the central data acquisition system (CDAS), including the central trigger processors and the permanent data storage area.

The SD has a 100% duty cycle, and a well-defined purely geometrical aperture ($\propto \cos\theta$) above trigger saturation at 3×10^{18} eV. The coverage is largely uniform in right ascension. Modulation in the event rate due to the atmospheric conditions are at the level of 2% for daily modulation and about 10% for seasonal ones. Those effects have been carefully studied and can be corrected for (Abraham *et al.*, 2009a).

The water tanks are 1.2 m in height and are mainly sensitive to muons, electrons, positrons, and photons. A vertical GeV muon hitting the tank deposits an energy of about 240 MeV, to be compared to a few tens of MeV for an average electron. The unit for the shower signal is a vertical equivalent muon (VEM). This allows for an *in situ* calibration of the PMT gain based on the rate of atmospheric muons. The gain is adjusted so that a single analog to digital converter count corresponds to about 1.5 MeV. Local triggers are adjusted to a rate of about 20 Hz for a simple threshold trigger and a few Hz for a more sophisticated time over threshold (counting time bins over a certain threshold within a given time window) (Abraham *et al.*, 2010e). Local triggers are sent to CDAS where space-time coincidences of at least three tanks are required to trigger the upload and permanent storage of the full event data.

The large sensitivity to muons and the height of the individual tanks allows the Auger array to have excellent sensitivity to horizontal showers, be them from hadronic origin or from neutrinos. The shower signal is sampled at a rate of 40 MHz. The analysis of its time structure allows, for example, to identify the presence of an electromagnetic component in the ground signal, at appropriate distances from the core to identify the short high pulse from the individual muons and to count them and to calculate signal shape parameters such as the rise time. This information allows one to efficiently distinguish neutrinos from the hadronic background in nearly horizontal showers and photons. Additionally, they also allow one to construct hadronic mass sensitive parameters. Timing information is obtained from a GPS receiver functioning in position hold mode. The absolute time resolution is about 10 ns, combined with the sampling of the shower front and front-end electronics, which allows for an angular resolution of better than 1° above 10^{19} eV (Bonifazi *et al.*, 2008; Bonifazi *et al.*, 2009). The aperture of the Southern Auger Observatory is energy independent when the surface array triggers and is determined by the area of the SD and the maximum shower zenith angle (60°) used in the analysis.

The lateral distribution function of the Auger tank signals is fitted to a NKG (Kamata and Nishimura, 1958; Greisen, 1960) function

$$f(r)_{\mathrm{NKG}} = S_{1000}\left(\frac{r}{1000\,\mathrm{m}}\right)^{\beta}\left(\frac{700\,\mathrm{m}+r}{1000\,\mathrm{m}+700\,\mathrm{m}}\right)^{\beta+\gamma}, \quad (18)$$

where S_{1000} is the adjusted normalization and the exponent β is adjusted to the data using a second-order polynomial in $\sec\theta$, whose coefficient is a linear function of S_{1000} in VEM [e.g., $a = a_0 + a_1 \log_{10}(S_{1000}/\mathrm{VEM})$]. The exponent γ is very close to zero.

2. Fluorescent detector

The fluorescent detector (FD) of Auger South is composed of 24 telescopes distributed in four sites installed at the periphery of the surface array and looking inward. Each telescope has a field of view of 30° × 30° in elevation and azimuth. A set of six telescopes in each site covers 180° in azimuth and observes the atmosphere above the ground array. This geometrical arrangement ensures full detection efficiency for showers in excess of 10^{19} eV over the entire surface of the array (Abraham *et al.*, 2010a).

In each telescope, the optical system is composed of an entrance filter selecting the UV light, an aperture and

corrector ring maintaining a large aperture while reducing spherical and eliminating coma aberrations, and a 3.6 m diameter mirror illuminating a camera composed of 440 PMT tubes. Each tube has a field of view of $1.5° \times 1.5°$.

Triggering is done at the hardware level of each camera for the first (pixel) and second (alignment) levels. A third level trigger is implemented in the software mainly to reject lightning events and random alignments. Each third level trigger is then processed at the fluorescent site level to merge all the telescope information and to send via CDAS, a preliminary shower direction and ground impact time to the surface array. The information from the tanks closest to the shower core is retrieved for showers that do not independently trigger three tanks. Together with additional fiducial cuts, this hybrid trigger is fully efficient above 10^{18} eV. Above this energy, the FD trigger is always accompanied by at least one station, independent of the mass and direction of the incoming primary particle (Abraham *et al.*, 2010d).

Event reconstruction proceeds in two steps. First, the shower geometry is found by combining information from the shower image and timing measured with the FD with the trigger time of the surface detector station that has the largest signal (Mostafa, 2007). From this timing information, it is possible to break the degeneracy intrinsic to Eq. (14). Therefore, the hybrid approach to shower observation enables the shower geometry and consequently the energy of the primary particle to be determined accurately. The Auger Collaboration uses a fluorescent yield in air at 293 K and 1013 hPa from the 337 nm band of 5.05 ± 0.71 photons/MeV of energy deposited taken from the measurements of Nagano and collaborators (Nagano *et al.*, 2004). The wavelength and pressure dependence of the yield adopted follows the measurements of the AIRFLY Collaboration (Ave *et al.*, 2008). Note that the fluorescent yield used by the HiRes Collaboration (Kakimoto *et al.*, 1996) in the same conditions is 5.4 photons/MeV (Arqueros *et al.*, 2009), which is very close to the value used by Auger.

In the second step, light attenuation from the shower to the telescope is estimated and all contributing light sources are disentangled (Unger *et al.*, 2008). A great deal of effort is spent by the Auger Collaboration to accurately monitor the atmospheric transparency and maintain the absolute calibration of the telescopes. An extensive set of instruments is installed and operated at the Auger site for this sole purpose (Abraham *et al.*, 2010b). Finally, the profile of energy deposition of the shower is reconstructed using a Gaisser-Hillas functional form (Abraham *et al.*, 2010a).

The reconstruction accuracy of hybrid events is much better than what can be achieved using SD or FD data independently. For example, the angular and energy resolution of hybrid measurements at 1 EeV is better than 0.5° and 6%, respectively, compared with about 2.5° and 20% for the surface detector alone.

VI. COSMIC RAY ENERGY SPECTRUM

A. The end of the cosmic ray spectrum

In 2008, the HiRes Collaboration published a paper (R. Abbasi *et al.*, 2008) with a title emphasizing the experimental proof of the Greisen-Zatsepin-Kuzmin (GZK) suppression. Soon after, the Auger Collaboration confirmed the observation of the end of the cosmic ray spectrum (Abraham *et al.*, 2008b). Greisen (1966) in 1966 and independently Zatsepin and Kuzmin (1966) predicted that the cosmic ray spectrum will end at several times 10^{19} eV because of the interactions of the UHECR with the microwave background (CMB). Although the energy of the CMB photons is very low, the center of mass energy of these interactions is enough to produce pions and cause high energy loss for these particles that decreases their flux.

The importance of these observation is that the previously largest air-shower array, AGASA, has observed 11 events above 10^{20} eV and no decrease above the predicted cutoff (Takeda *et al.*, 1998). A reevaluation of the energy assignment of AGASA based on a larger data set was published later by Takeda *et al.* (2003). The energy determination of AGASA was tied up to the particle signal at 600 m from the shower axis $S_0(600)$. The Monte Carlo calculations suggested that the primary energy is

$$E = 2.17 \times 10^{1.03} E_0(600) \text{ eV}.$$

Since the detectors of AGASA were scintillator counters, the signal is produced by the shower electromagnetic component with a small contribution from the shower muons. The ultrahigh energy events published by AGASA provided the inspiration for the exotic ''top-down'' models of these particles.

The HiRes energy spectrum was based on monocular observations with the two fluorescent telescopes HiRes-I and HiRes-II that were operated from 1997 to 2005 and from 1999 to 2004, respectively. Some corrections were made on the previous HiRes spectrum release (Abbasi *et al.*, 2004). Special attention was paid to the detector calibration and the atmospheric conditions, which were studied by standard meteorological methods and observation and analysis of laser shots from different locations surrounding the two detectors. Most of the highest energy events were observed with HiRes-I. The exact shape of the spectrum depends strongly on the calculation of the aperture for the two telescopes. The HiRes found two breaks in the cosmic ray spectrum: one at energy $10^{18.65\pm0.05}$ (the cosmic ray ankle) and another at $10^{19.75\pm0.04}$ at the GZK cutoff. The spectral index between the two breaks is 2.81 ± 0.03 and after the cutoff is 5.1 ± 0.7. The spectrum is consistent with various models and, in particular, the model of Berezinsky *et al.* (2006) with pure proton composition. An important parameter is $E_{1/2}$ where the cosmic ray flux is one half of what it should have been without the GZK effect. $E_{1/2}$ was predicted by Berezinsky and Grigor'eva (1988) to be $10^{19.76}$ and HiRes measured $10^{19.73\pm0.07}$. The statistical significance of the cutoff is more than 5σ.

The energy spectrum derived by the Auger Collaboration (Abraham *et al.*, 2008b) is shown with those of HiRes and AGASA in Fig. 14. As well as HiRes, Auger observes the shower profile with its fluorescent detectors. They, however, have a live time of 13% compared to that of the surface detector. Taking full advantage of its hybrid design, the Auger Collaboration decided to correlate the energy derived from the fluorescent observations to the shower signal at 1000 m from the shower core (S_{1000}), which is the least sensitive to

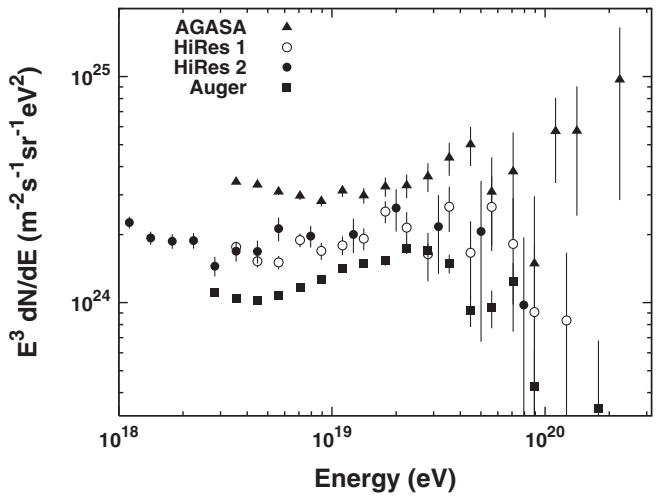

FIG. 14. Cosmic ray spectrum as presented by AGASA, HiRes, and Auger.

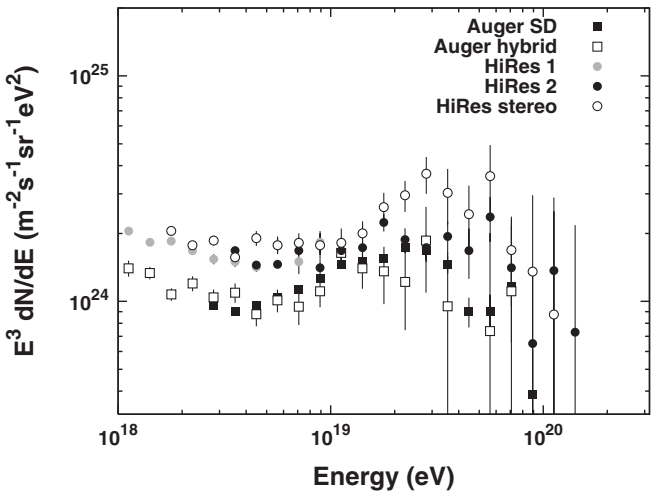

FIG. 15. Cosmic ray spectrum as measured by HiRes and Auger.

the cosmic ray composition. To account for the angular dependence of this quantity, it was corrected to the median angle of 38°, S_{1000}^{38}, using the constant intensity curve (Hersil *et al.*, 1961) observed by the surface array. The constant intensity curve is a study of the change with an angle of the signal threshold above which cosmic rays arrive with constant rate, i.e., study of the shower absorption in the atmosphere.

The correlation between FD and S_{1000} was studied in high quality hybrid events that were seen in both the surface and fluorescent detectors. The correlation showed that

$$E_{\mathrm{FD}} = 1.49 \pm 0.06 \pm 0.12(\mathrm{syst}) \times S_{1000}^{1.08\pm0.01\pm0.04} \times 10^{17}\,\mathrm{eV}. \tag{19}$$

The Auger Collaboration then used the surface detector statistics to produce the energy spectrum. The uncertainty in the energy reconstruction by the fluorescent telescopes was estimated to 22% and the width of the observed correlations was consistent with the statistical uncertainty of both measurements. The surface detector exposure for this publication was twice that of HiRes and 4 times higher than AGASA. Since the fluorescent energy measurement does not depend on the hadronic interaction model used in the analysis, such an estimation of the spectrum was considered to be model independent.

The Auger spectrum has a slightly different shape in addition to the energy assignment. From 4×10^{18} to 4×10^{19} eV, the slope of the spectrum is $2.69 \pm 0.02 \pm 0.06$(syst) and above it is $4.2 \pm 0.4 \pm 0.06$(syst). A single power law for the whole data set is rejected at the 6σ level.

Measurements of the cosmic ray spectrum were extended by using stereo events in HiRes (Abbasi *et al.*, 2009) and hybrid events in Auger (Abraham *et al.*, 2010d). Stereo events are reconstructed much more precisely than monocular ones and they confirmed the previously measured spectrum. Auger used hybrid events to extend the spectrum to lower energy. The Auger exposure at the time of this last publication was 12 790 $\mathrm{km^2\,yr\,sr}$. All measured spectra from HiRes and Auger are shown in Fig. 15.

The new Auger spectrum is a bit flatter than the older one, with an index of 2.59 ± 0.02 between the breaks and 4.3 ± 0.2 above that. The $E_{1/2}$ value is $10^{19.61\pm0.03}$. The differences in the interpretation of the HiRes and Auger spectra are significant. The Auger spectrum can be explained by several different models, some of which include mixed chemical composition at acceleration in the sources. The end of the cosmic ray spectrum measured by Auger is consistent with the GZK effect.

B. Cosmic ray energy loss in propagation

In addition to the adiabatic energy loss because of the expansion of the Universe, there are two important energy loss processes for protons: pion photoproduction interactions and e^+e^- pair-production (BH) interactions identical to the pair-production interactions of γ rays in the nuclear field. The average interaction length λ_{ph} for interactions with the CMB is the inverse of the product of the interaction cross section σ_{ph} and the photon density n. For $\sigma_{\mathrm{ph}} = 10^{-28}$ $\mathrm{cm^2}$ and $n = 400$ $\mathrm{cm^{-3}}$, $\lambda_{\mathrm{ph}} = 8.3$ Mpc.

Heavy nuclei lose energy in photodisintegration (spallation) processes (Stecker, 1969) when the center of mass energy exceeds the giant dipole resonance. Since less energy is required in the center of mass, the cross section is higher, but the energy loss depends on the mass of the nucleus that loses one or two nucleons. The photoproduction energy loss follows the same energy dependence as for protons but in the Lorentz factor space, i.e., in E/A units. The pair-production cross section is a quadratic function of the charge of the nucleus Z.

In the case of γ rays, the energy loss is due to the $\gamma\gamma \rightarrow e^+e^-$ process.

A photoproduction interaction is possible (Stecker, 1968) when the center of mass energy of the interaction $\sqrt{s}$ is higher than the sum of a proton mass m_p and a pion mass m_π. In the laboratory system, the square of the center of mass energy is

$$s = m_p^2 + 2E_p\epsilon(1 - \cos\theta), \tag{20}$$

where ϵ is the photon energy and θ is the angle between the proton and the photon. In a head on collision ($\cos\theta = -1$)

with a photon of the average CMB energy (6.3×10^{-4} eV), the minimum proton energy is

$$E_p = \frac{m_\pi}{4\epsilon}(2m_p + m_\pi) \simeq 10^{20} \text{ eV}. \quad (21)$$

There are many CMB photons with higher energy and the threshold proton energy is actually lower, about 3×10^{19} eV.

The cross section for pion photoproduction was well studied at accelerators. The highest cross section is at the mass of the Δ^+ resonance (1232 MeV). At the peak of the resonance, the cross section is about 500 μb. The cross section decreases to about 100 μb and then increases logarithmically. The neutron interaction cross section is very similar to the proton one.

The CMB spectrum and density are also very well known, so the proton interaction length can be calculated exactly. Since protons lose only a fraction of their energy (K_{inel}), another quantity, the energy loss length $L_{\text{loss}} = -E^{-1}dE/dx$, becomes important. The energy loss length is longer than the interaction length by $1/K_{\text{inel}}$, by about a factor of 5 at threshold. At higher energy K_{inel} grows and this factor is about 2.

In the case of e^+e^- pair production (Berezinsky and Grigor'eva, 1988), the addition of two electron masses to the center of mass energy $\sqrt{s}$ requires much lower proton energy and the process has a lower threshold. The cross section is higher than σ_{ph}, but the fractional energy loss is of order of m_e/m_p. The energy loss length has a minimum around 2×10^{19} eV and is always longer than 1000 Mpc.

The last proton energy loss process is the redshift due to the expansion of the Universe. The energy loss length to redshift is the ratio of the velocity of light to the Hubble constant (c/H_0) and is 4000 Mpc for $H_0 = 75$ km s^{-1} Mpc^{-1}.

The energy loss length of protons in the CMB is shown in Fig. 16.

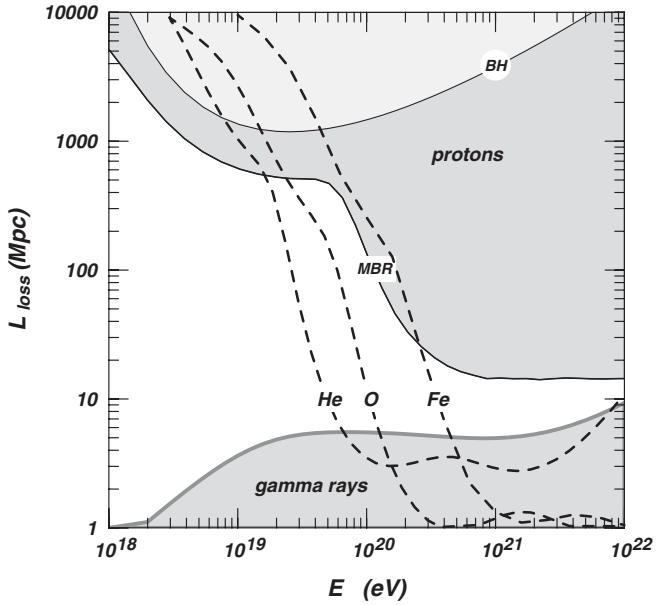

FIG. 16. Energy loss length for protons, nuclei, and gamma rays. The heavier shading points at the proton and gamma ray L_{loss} and the light one shows the contribution of the e^+e^- pair production. The adiabatic energy loss is not included.

The energy loss length for several nuclei is also shown in Fig. 16 as calculated by Allard *et al.* (2005). The minimum value of L_{loss} is significantly lower than that of protons, but is achieved at higher energy AE_p. Since only iron has similar L_{loss} to protons around 10^{20} eV, it is considered the only nucleus that can compete with protons in the chemical composition of UHECR. The effect of propagation on the accelerated UHECR cannot be calculated directly from the energy loss lengths shown in Fig. 16 because an accelerated nucleus changes its mass after the first photodisintegration. A code treating the propagation of nuclei should account for the energy loss of all nuclei and isotopes lighter than the injected nucleus.

The process $\gamma\gamma \rightarrow e^+e^-$ has a resonant character and the cross section peaks at $E_\gamma \epsilon = 2m_e^2$, where ϵ is the ambient photon energy. For CMB, this corresponds to E_γ of 8×10^{14} eV and the mean free path decreases with increasing E_γ. For gamma rays of energy 10^{20} eV, the relevant seed photon frequency is about 1 MHz in the radio band. This creates some uncertainty in the estimates of the UHE γ ray energy loss length because the density of the radio background at such frequencies is not well known.

A different source of uncertainty in the γ-ray propagation is the strength of the extragalactic magnetic fields. If they are negligible, the electrons have inverse Compton interactions, whose interaction length is similar to that of the pair production, and generate a second generation of very high energy γ rays. If, however, the magnetic fields are significant, electrons lose energy very fast on synchrotron radiation and the created γ rays are in the MeV–GeV energy range. The energy loss distance on synchrotron radiation is $2.6E_{18}^{-1}B_{-9}^{-2}$ Mpc, where E_{18} is the electron energy in units of 10^{18} eV and B_{-9} is the strength of magnetic field in nGauss.

C. Formation of the cosmic ray energy spectrum in propagation

Predictions of the shape of the cosmic ray spectrum requires much more than the energy loss in propagation. The necessary astrophysical input includes at least the following items: UHECR source distribution, cosmic ray source emissivity, cosmic ray injection (acceleration) spectrum, maximum acceleration energy E_{max}, cosmic ray chemical composition, cosmic ray source cosmological evolution that are not independent of each other. As an example, we discuss the formation of the proton spectrum in propagation.

Figure 17 shows the contribution to the observed UHE cosmic ray proton flux by sources located at different redshifts that inject protons on a E^{-2} spectrum with an exponential cutoff at $10^{21.5}$ eV. One can see how the energy loss increases the contribution to the $(2–6) \times 10^{19}$ eV energy range after propagation to $z = 0.1$. In models with cosmological evolution of the sources, the effect is stronger and proportional to the strength of the source evolution.

A simplification in such a calculation is the assumption that sources are isotropically and homogeneously distributed in the Universe and the contribution of all sources are identical. In such a case, the cosmic ray flux at the Earth can be determined by an integration of the fluxes from different redshifts shown in Fig. 17. In the case of cosmological evolution of the sources, the integral is

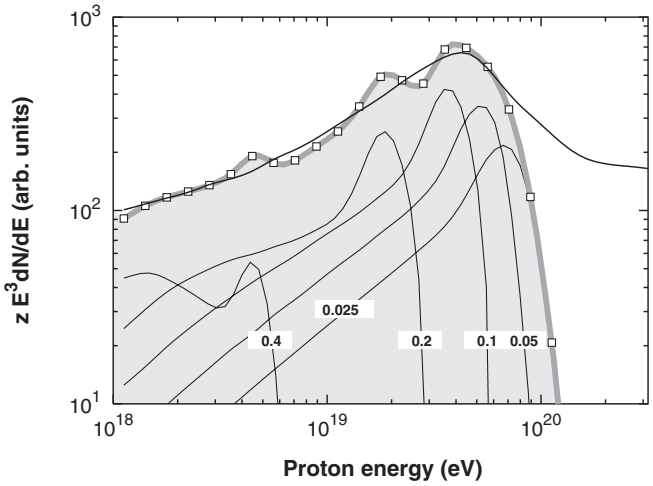

FIG. 17. Contribution of different redshifts to the arrival spectrum for E^{-2} injection spectrum with no cosmological evolution. The thick gray line shows the sum of the contributions from these five redshifts while the black line is a result of a full integration.

$$N(E) = \int_0^{z_{\max}} \int_E^{E_0} L(z) N_0(E_0) P(E_0, E', z) \frac{dt}{dz} dE' dz, \quad (22)$$

where $L(z)$ is the cosmic ray source emissivity as a function of redshift and $N_0(E_0)$ reflects the injection spectrum. $P(E_0, E', z)$ is the probability for a proton injected with energy E_0 at redshift z to reach us with energy E'. The derivative dt/dz depends on the cosmological model and is

$$\frac{dt}{dz} = \frac{1}{H_o(1+z)} [\Omega_M (1+z)^3 + \Omega_\Lambda]^{-1/2}$$

and is simplified to $(1+z)^{-5/2}/H_o(1+z)$ for the Einstein–de Sitter Universe.

It is important to note that the contribution of different redshifts depends not only on the cosmological evolution but also on the injection spectral index as the photoproduction energy loss is a strong function of the injection energy. Since in steep injection spectra a larger fraction of the observed flux comes from lower primary energy (that do not change as much on propagation), the contribution of higher redshifts is larger.

One can see in Fig. 17 that even $z = 0.05$ does contribute to UHECR above 6×10^{19} eV where the GZK cutoff is already present. Another explanation is that the cutoff is just the end of the acceleration power of the sources that does not much exceed 10^{20} eV (Watson, 2007; Aloisio *et al.*, 2009). The extragalactic magnetic fields can also be involved in the explanation. If they are high, UHECR would scatter often and their real path length would be considerably larger than the distance to the sources as in Stanev *et al.* (2000).

VII. CHEMICAL COMPOSITION OF UHECR

One has to use the properties of the extensive air showers to identify the type of the primary particle whose interaction in the atmosphere has initiated the shower. Because of the high level of fluctuations in the shower development, it is quite difficult to distinguish showers originating from different hadronic primaries on an event by event basis—it can only be done on a statistically significant set of showers. At lower energy, around the knee, the main parameter in composition studies is the ratio of the shower muon to electron components, which increases with the primary nucleus mass.

Another way is to study the shower longitudinal development. This is usually done by observing the depth of shower maximum $X_{\max}$ with fluorescent detectors that can determine the atmospheric depth where the shower particles emit the highest amount of fluorescent light. The shower longitudinal development, as we will see in this section, can also be studied by the surface detectors.

A. Limits on the flux of neutrinos

Possible shower neutrino primaries may be the easiest to identify (Capelle *et al.*, 1998). The reason is the many orders of magnitude difference between the hadronic and neutrino cross sections. If neutrinos interact in the atmosphere at all, they would interact very deep. It is more likely that they interact in the rock of the Earth. This was used by the Auger Collaboration in order to set a limit on the flux of τ neutrinos. Setting such a limit is equivalent to a limit on the total neutrino flux. Although ν_τ's are rarely produced in particle interactions, cosmic neutrinos oscillate in propagation to the Earth. While at production, the neutrino flavor ratio $(\nu_e{:}\nu_\mu{:}\nu_\tau)$ is close to 1:2:0; after propagation it is close to 1:1:1.

The tau neutrino detection idea (Bertou *et al.*, 2002) is that in a small fraction of the solid angle at zenith angles θ between 90.1° and 95.9° tau neutrinos will graze the Earth, possibly interact, and after escaping the Earth the tau decay will generate a shower that can be seen by the shower array. The neutrino identification is based on the different quality of vertical and almost horizontal showers. Vertical showers are young: they exhibit long, $\sim\mu$s waveforms in the surface detectors. Old showers, after penetrating about two atmospheric depths, consist mostly of muons. The waveforms they generate in the surface detectors are much shorter, of order of 100 ns. If one detects an almost horizontal shower that has the waveforms of young showers, it would mean that the primary particle has interacted near to the detector and is most likely a neutrino.

Atmospheric interaction of tau neutrinos are also especially interesting, because they should develop two showers (Learned and Pakvasa, 1995), one when the τ neutrino interacts and the second one when the τ lepton decays. Since the τ energy loss is much lower than that of a muon, most of the neutrino energy is released through the τ decay. The exact parameters for ν_τ shower identification are found with Monte Carlo calculations.

The Auger Collaboration is using two related parameters. The first one is the shower shape in the surface array. Because of the large zenith angle, it should be elongated. The collaboration defined the shower *length* and shower *width*. The Monte Carlo calculations showed that there is no chance for a nucleus or a γ ray to generate a shower with length and/or width ratio higher than 5.

The second parameter is the shower *ground speed*. If the shower is indeed horizontal, it has to move with velocity equal to the speed of light. So, they looked for showers with velocity between 0.29 and 0.31 m/ns. Only showers with RMS (ground speed) better than 0.08 m/ns are included in the sample. These requirements together with the general requirement that the tank with the maximum VEM signal is surrounded by six active tanks significantly decrease the size of the sample. Anyway, no such showers were found in the Auger statistics. The Auger exposure as a function of energy was determined by Monte Carlo calculations.

Using the statistics between January 2004 and August 2007, the Auger Collaboration set an integral limit on the ν_τ flux between 2×10^{17} and 2×10^{19} eV of $E_\tau^2 dN/dE_\tau$ of 1.3×10^{-7} GeV. This limit assumes that the ν_τ energy spectrum is E^{-2}. In the same publication (Abraham *et al.*, 2008d), the collaboration used the exposure as a function of the neutrino energy to also give a differential limit. Extending the statistics to April 2008, the Auger Collaboration decreased the integral limit of $E_\tau^2 dN/dE_\tau$ of to about 6×10^{-8} GeV cm^{-2} s^{-1} sr^{-1} (Abraham *et al.*, 2009b) for the same flat ν_τ spectrum. This limit is shown as a gray line in Fig. 25. The integrated Auger limit is competitive with the limits set by the neutrino telescope AMANDA (Achterberg *et al.*, 2007) at lower energy.

The HiRes Collaboration has also set limits on the fluxes of tau and electron neutrinos (Martens *et al.*, 2007; R. U. Abbasi *et al.*, 2008a). The first limit is based on the same assumptions as the Auger one. The HiRes Collaboration has simulated τ-neutrino induced showers hitting the Earth with elevations between 10° and −10° with an account of the topography of the detector. After detection simulation, they obtained 6699 monocular triggers and 870 stereo ones. Then the collaboration analyzed with some quality cuts simulated and real data events with reconstructed zenith angles between 88.8° and 95.5°. The data sample yielded a total of 134 events that happened to be laser events, which passed the cuts because of the light scattering near the ground. Thus, they were left with no neutrino candidates.

For the limit on electron neutrino events, only the HiRes-II detector data were used because of its superior reconstruction. HiRes looked at upward going showers with zenith angles above 105°. Lower zenith angles do not yield more events because of the neutrino absorption in the Earth. The basis of the search is the fact that high energy electrons have much lower energy loss at high energy and especially in dense materials because of the Landau-Pomerntchuk-Migdal effect (Landau and Pomeranchuk, 1953; Migdal, 1956). After electron neutrino charge current interactions in the ground, the generated electrons would not lose much energy and may produce upward moving air showers. The simulations were done for neutrinos of energy exceeding 10^{18} eV that generate horizontal and upward moving air showers with more than 10^7 particles at maximum. These showers were then treated with the HiRes detector simulations and compared to experimental data. No neutrino candidates were observed. The combination of the two searches reduced the integral neutrino flux limits in the three decades above 10^{18} eV to 3.8×10^{-7}, 9.7×10^{-6}, and 4.7×10^{-6} GeV cm^{-2} sr^{-1} s^{-1}.

B. Limits on the fraction of gamma rays

The limit on the fluxes of ultrahigh energy neutrinos is astrophysically important because it is related to the dynamics of the systems where UHE cosmic rays are accelerated and the importance of hadronic interactions in such objects. The limit on the fraction of photons in UHECR determines the general origin of the highest energy particles in the Universe. All top-down models of the UHECR origin predict that 90% of these particles are γ rays and neutrinos. There have been previous limits from several UHECR air-shower arrays for energies above 10^{19} eV, but none of them was less than 10%.

Auger has the advantage of being a hybrid array. A fluorescent detector trigger with a single surface detector trigger improves significantly the shower reconstruction and lowers the detection threshold. The Auger Collaboration set limits on the fraction of γ rays at energies above 2×10^{18}, 3×10^{18}, 5×10^{18}, and 10×10^{18} eV (2, 3, 5, and 10 EeV) (Abraham *et al.*, 2007a; Abraham *et al.*, 2009d). The limit is based on the measurement of the shower depth of maximum $X_{\max}$. Because of the low secondary multiplicity in electromagnetic interactions, UHE γ-ray induced showers reach maximum much later than proton showers. In addition, at energies above 10^{19} eV, the Landau-Pomerntchuk-Migdal effect, which significantly decreases the pair-production cross section, starts becoming important and increases $X_{\max}$ even more. The key in such a measurement is to make certain that the event selection is not biased versus showers with deep $X_{\max}$.

There are many cuts that are applied to the detected showers that exclude the possible biases. Auger requires that the tank with the largest signal is less than 1.5 km from the reconstructed shower axis and the time difference between the fluorescent and tank signals is small. Another requirement is that the shower $X_{\max}$ is observed in the telescope field of view. The minimum angle between a fluorescent pixel and the shower direction has to be above 10° to exclude Cherenkov light contamination. The shower zenith angle has to be higher than 35° and the distance of the shower core to the telescope less than 24 km.

All of these different cuts, together with the requirement for a good reconstruction in the fluorescent detector, decrease the total statistics above 2 EeV to 2063 events. Eight of these events have $X_{\max}$ consistent with possible photon showers. Using the 95% confidence value for the number of photon candidate events and the systematic uncertainty of 22% in the energy estimate and 11% in $X_{\max}$, the Auger Collaboration arrives at an 95% upper limit on the fraction of photon showers above 2 EeV of 3.8%. At higher energy bins, the number of photon candidate showers is 1, 0, and 0, but the statistics are lower, 1021, 436, and 131 events, respectively. This leads to 95% proton fraction estimates of 2.4%, 3.5%, and 11.7% as shown in Fig. 18.

At higher energy, the photon fractions are calculated using the surface detector results (Risse and Homola, 2007). This analysis (Abraham *et al.*, 2008c) is interesting because it uses surface detector shower characteristics rather than the direct $X_{\max}$ measurement. The idea of such an analysis was first developed for the inclined showers detected by the Haverah Park array (Ave *et al.*, 2002). When the air-shower particles hit the surface array detectors, the shower front is not flat, it

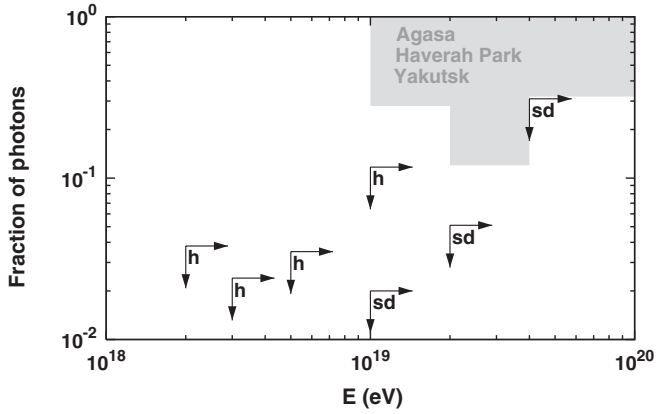

FIG. 18. Fraction of photon showers above certain energy determined by the hybrid analysis (labeled *h*) and the surface detector (*sd*). The shaded area shows limits set by Haverah Park (Ave *et al.*, 2002), AGASA (Shinozaki *et al.*, 2002), and Yakutsk (Glushkov *et al.*, 2010).

has a certain curvature, i.e., the shower particles away from the shower axis arrive later than those close to it. If the shower curvature is assumed to be spherical (which is an oversimplification), the delay is proportional to r^2/H, where H is the altitude of the particle production and r is the distance from the shower axis. This means that in early developing showers, the shower curvature is smaller than in later developing ones. The radius of shower curvature R_c is the first parameter that can be measured by the surface array.

The second parameter is the width of the shower front, i.e., the time that it takes the shower particles to arrive at the surface array. The spread of the arrival time at certain distance r from the core also increases with the depth of $X_{\max}$. This could be measured by the surface array as the arrival time at a fixed distance from the shower core $\tau_{1/2}$, which is defined by Auger as the time in which 10% to 50% of the signal arrives at a detector. Since photon showers develop deeper in the atmosphere than nuclear showers, one can identify them by their large R_c and $\tau_{1/2}$. For photon showers, one can use Monte Carlo calculations that have the advantage to depend very little on the hadronic interaction models used in nuclear shower calculations. The only remaining problem is the energy assignment of the photon showers—the fluorescent detector value is used for hadronic showers. Auger developed an estimate that gave them 25% accuracy for photon showers.

The Monte Carlo calculations of photon showers generated values of these two parameters for all zenith angles that were very different from those of the detected air showers from 2004 to the end of 2006. The data set used includes 2761, 1329, and 372 showers above 10, 20, and 40 EeV. There were no γ-ray candidates in either bin, while 570, 145, and 21 showers are certainly nuclear showers. Since zero events per bin corresponds to less than 3 events at 95% confidence level, the fraction of photon showers was calculated to 2.0%, 5.1%, and 31% in the three bins.

These results demonstrate that the top-down models are not responsible for the production of the majority of UHECR. There is still a little space remaining at the highest energies, but in 5 years of operation Auger South will be able to bring down these limits if the current trend continues.

It is indeed true that the differences between different hadronic interaction models do not play much of a role in the photon showers. Monte Carlo calculations and these analyses are mostly independent of the details of those interactions.

C. Depth of maximum data and their interpretation

The application of Heitler's toy shower model to the shower longitudinal development demonstrates its dependence on the mass of the primary particle. With the advent of fluorescent detectors, the measurement of the shower depth of maximum $X_{\max}$ quickly became a major component of the cosmic rays composition studies. An important parameter is the shower elongation rate D_{10}, the relation of which to the changes in the cosmic ray composition is discussed first by Linsley and Watson (1981).

The first analysis of the $X_{\max}$ energy dependence with fluorescent detector data was done with the Fly's Eye. This analysis (Gaisser *et al.*, 1993), which used only two chemical components, H and Fe, showed a trend of increasing the proton fraction in cosmic rays of energy above 10^{18} eV.

In 2005, the HiRes Collaboration published an analysis of the UHECR composition from $X_{\max}$ measurements (Abbasi *et al.*, 2005b). The data sample included 553 events of energy above 10^{18} detected in stereo by both fluorescent detectors during 20 months from 1999 to 2001. The sample is relatively small because of the different cuts made on the total event sample. The first set of cuts are related to the atmospheric conditions. About 3/4 of the total sample had hourly data on the vertical aerosol optical depth obtained with laser shots from the location of both detectors. The cuts on the remaining events used the average atmospheric conditions and the records made during the measurement. The rest of the cuts address the reconstruction quality. They include a minimum viewing angle of more than 20° in both detectors, more than 5° difference in the shower detector plane (to decrease the effect of scattered Cherenkov light), χ^2 of the global fit of less than 15 p.d.f. and bracketing of $X_{\max}$ within the observed tracks. The application of the same cuts to a Monte Carlo data set gives a $X_{\max}$ resolution of 30 g/cm^2 and energy resolution of 13%.

This analysis was presented in a combination with an earlier result (Abu-Zayyad *et al.*, 2000b) obtained by the HiRes prototype working in coincidence with the the Chicago air shower array and the Michigan muon array. The elongation rate between 10^{17} and $10^{18.5}$ eV was measured to be 93 ± 8.5 g/cm^2 with a systematic uncertainty of 10.5 g/cm^2. This result suggested a quick transition from heavy to light cosmic ray composition.

The HiRes 2005 paper measured $D_{10} = 54.5 \pm 6.5$ g/cm^2 consistent with the values for constant composition from different hadronic interaction models. The data points above 10^{18} eV agreed within the errors with the results from the HiRes-MIA coincidence experiment. The HiRes points, which are derived from fitting the shower profile with the Gaisser-Hillas formula, are shown as empty circles in Fig. 19. The lines in the same figure show the expectations from three

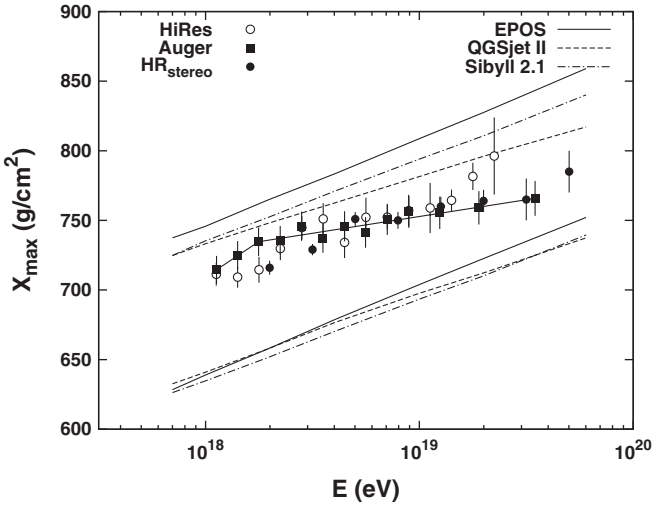

FIG. 19. Depth of maximum measurements of UHECR by the HiRes Collaboration (2005) analysis shown with empty circles and 2010 analysis with full circles and the Auger Collaboration; full squares are compared with the predictions of three different interaction models for H and Fe.

different hadronic interaction models: EPOS 1.99, QGSjet II, and SIBYLL 2.1. The fraction of protons is different for these interaction models. QGSjet II shows almost pure proton composition with a possible small He contamination. In the case of SIBYLL 2.1, the fraction of protons is smaller but still significant. QGSjet II has a moderate cross section energy dependence and fast multiplicity increase. SIBYLL 2.1 has a fast cross section growth and a relatively low multiplicity. The comparison with EPOS 1.99, which has the largest D_{10}, may even point at large, but decreasing with energy, fraction of protons.

The interpretation of the $X_{\max}$ data will become better after the LHC results are accounted for in the hadronic interaction models used in the analysis. The current models do not disagree with each other in the energy range studied in accelerators. After the normalization of these models to the LHC data, the differences in the interpretation of the experimental results will significantly decrease.

HiRes also studied the width of the $X_{\max}$ distributions in different energy bins. Proton showers do have a wider distribution, while iron showers have widths lower by at least a factor of 2. Comparisons with simulations using QGSjet 01 were consistent with a proton fraction of 80% and those with SIBYLL 2.1 suggested a proton fraction of about 60%. EPOS 1.99 did not exist at that time. The general conclusion of the HiRes $X_{\max}$ study is that the cosmic ray composition was heavy at 10^{17} eV, progressed to light in 1 order of magnitude in energy, and stayed light with a proton fraction from 60% to 80% above 10^{18} eV.

Although the Auger Collaboration has presented its $X_{\max}$ measurements at different conferences, the first journal publication on this topic appeared in 2010 (Abraham *et al.*, 2010c). The results of this study are unfortunately very different from those of HiRes. This analysis is done using only hybrid events, i.e., events detected by one or more fluorescent telescopes plus at least one surface detector. Using the timing of the surface detector vastly improves the quality of the reconstruction. The light collected by the fluorescent detector is corrected for attenuation using the atmospheric monitoring devices. The fitting is done using the Gaisser-Hillas function. Events with light emission angle less than 20° are not used, neither are events where $X_{\max}$ uncertainty due to shower geometry and atmospheric conditions is more than 40 g/cm^2. The limit on the reconstruction χ^2 is set to less than 2.5 p.d.f. The resulting $X_{\max}$ resolution above several EeV is about 20 g/cm^2. This number is consistent with the checks with stereo fluorescent detector observations.

Using data taken between 2004 and March 2009, there are 3754 events above 10^{18} passing all cuts. The highest energy event is of energy $(59 \pm 8) \times 10^{19}$ eV. The measured $X_{\max}$ in 10 logarithmic bins per decade are shown in Fig. 19 as full squares. The elongation rate of the three points below $10^{18.25}$ eV is 106^{+35}_{-21} g/cm^2 and that above this point is 24 ± 3 g/cm^2. Both these values are determined with good χ^2 fits. Systematic uncertainty is around 10 g/cm^2. In absolute value, this data set does not appear extremely different from the HiRes 2005 analysis (Abbasi *et al.*, 2005b), but its interpretation is different. Instead of a constant elongation rate of 54.5 g/cm^2, we have a large one, maybe similar to that of HiRes-MIA, in the lower energy part and a short one at higher energy. The cosmic ray composition thus has to become lighter up to $10^{18.25}$ eV and then consistently heavier up to the highest energy measured. The Auger Collaboration is careful enough to state that such interpretation is reasonable if there are no drastic changes in the hadronic interactions in this energy interval.

The Auger Collaboration also studied the width of the $X_{\max}$ distributions (RMS) in the same energy bins. While the RMSs in the first five bins look consistent with a light composition at higher energies there is a steep decrease of RMS($X_{\max}$) consistent with heavier and heavier composition as shown in Fig. 20. The RMS values decrease from about 55 to 26 g/cm^2 in the last bin. This distribution width is consistent with cosmic ray composition dominated by iron. The interaction model predictions for proton showers give 60 g/cm^2

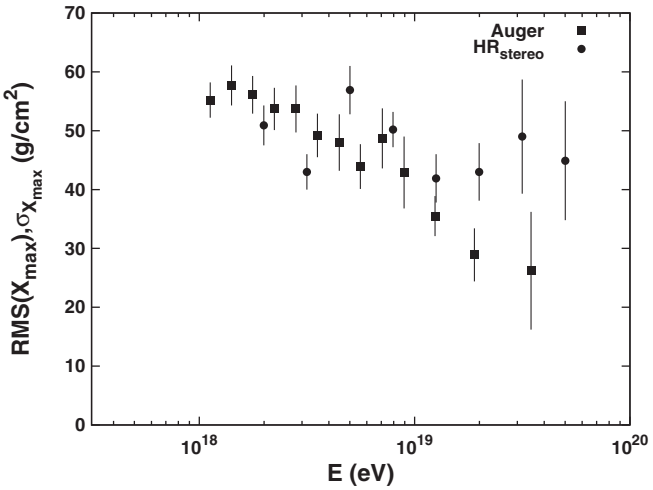

FIG. 20. Width of the $X_{\max}$ distributions as measured by HiRes (full circles) and Auger (full squares). Note that the width is presented in different ways (see text) and the points cannot be compared directly.

with a slight energy dependence and these for iron showers give about 22 g/cm^2. The linear decrease of RMS(X_{max}) is not, however, consistent with a simple change of the cosmic ray composition from pure proton to pure iron.

It is worth noting that the Auger Collaboration has also attempted to use the surface detector data for studies similar to those of X_{max} (Abraham *et al.*, 2009c). Since these results are preliminary, we only give the general idea. The width of the shower front depends on the depth of the shower maximum. One can study the shower front width by measuring the rise time of the surface detector signals. The attempt to do that is fully consistent with the more detailed fluorescent detector analysis.

The final analysis of the stereo measurements of HiRes in the period of 1999 to 2006 was published in Abbasi *et al.* (2010). The cuts on the data are more stringent than in the previous analysis. Apart from the good weather requirement, they limit the chance of noise coincidence to less than 1% and the longitudinal development fit χ^2 to less than 4 p.d.f. The final data set of 815 events includes only events with zenith angle uncertainty of less than 2°, X_{max} uncertainty of less than 40 g/cm^2, zenith angle less than 70°, and distance to HiRes-II more than 10 km. The measured X_{max} should be bracketed by the HiRes-II field of view and have a shower detector plane between 40° and 130°. The application of the vertical aerosol optical depth hourly measurements to the amount of light received by the detectors requires a mean upward correction of ~15% to shower energy for an event 25 km distant from the observatory. Shower segments with emission angles of less than 5° of a bin pointing direction are not used in the analysis.

The measured light profile of the shower is fit to a Gaussian function of the age parameter s to determine the shower energy and X_{max}. The claim is that the use of the Gaisser-Hillas function does not change the results within the errors. Showers of energy between 1.6×10^{18} and 6.3×10^{19} eV are included in the analysis.

All uncertainties in the X_{max} measurement come from the treatment of simulated showers after the detector is accounted for. Comparisons of the reconstructed X_{max} with the original one showed that the selection and reconstruction results in X_{max} shallower by about 15 g/cm^2 than the original one. As such, interpretation of the measurement predictions are appropriately scaled. The Monte Carlo measured uncertainty of X_{max} is better than 25 g/cm^2 over most of the energy range.

This analysis finds a constant elongation rate of 47.9 ± 6 g/cm^2 with fit χ^2 of 0.86 p.d.f over the whole range with systematic uncertainty of 3.2 g/cm^2. Most of the systematic uncertainty is due to the event selection cuts.

HiRes also presents the energy dependence of the X_{max} fluctuations in the same energy bins. These numbers are obtained in a different way from those of the Auger Collaboration. Since these X_{max} distributions are wide and asymmetric, the HiRes analysis fits them to Gaussian distributions truncated at $2 \times$ RMS. The distributions are still wide, as shown in Fig. 20.

The heavy cosmic ray composition derived from the Auger data suggests that the strong decline of the cosmic ray flux may be caused by exceeding the maximum acceleration energy at the cosmic ray sources. In such a case, only iron nuclei could be accelerated to energies exceeding 10^{20} eV.

D. Transition from galactic to extragalactic cosmic rays

One of the reasons for identifying different features at the end of the cosmic ray spectrum is to study the transition between the galactic and extragalactic components. The common opinion is that most of the cosmic rays above 10^{19} eV are of extragalactic origin and the GZK feature supports that. The main question was (and is) the origin of the dip at around 3×10^{18} eV. The prevailing school of thought was that the dip is at the intersection of the galactic and extragalactic components as explained by Hillas (1984) and Bahcall and Waxman (2003). In this model, the extragalactic cosmic rays have a flat E^{-2} spectrum and the galactic ones have a steep $E^{-3.5}$ spectrum as shown in the upper panel of Fig. 21 with two values (3 and 4) of the parameter m in the evolution described as $(1 + z)^m$ up to redshift of about 2. As is seen from the figure, the cosmological evolution does not much affect the predicted spectra because the observed UHECR have to be local. The galactic cosmic rays, although with a small contribution, extend well above 10^{19} eV as shown with a dashed line in the figure. It soon became obvious that extragalactic cosmic rays cannot have such a flat injection spectrum subsequent models deal with $E^{-2.3}$ or slightly steeper spectra.

Soon after that Berezinsky *et al.* (2006) suggested a totally different model. The dip is caused by the pair-production

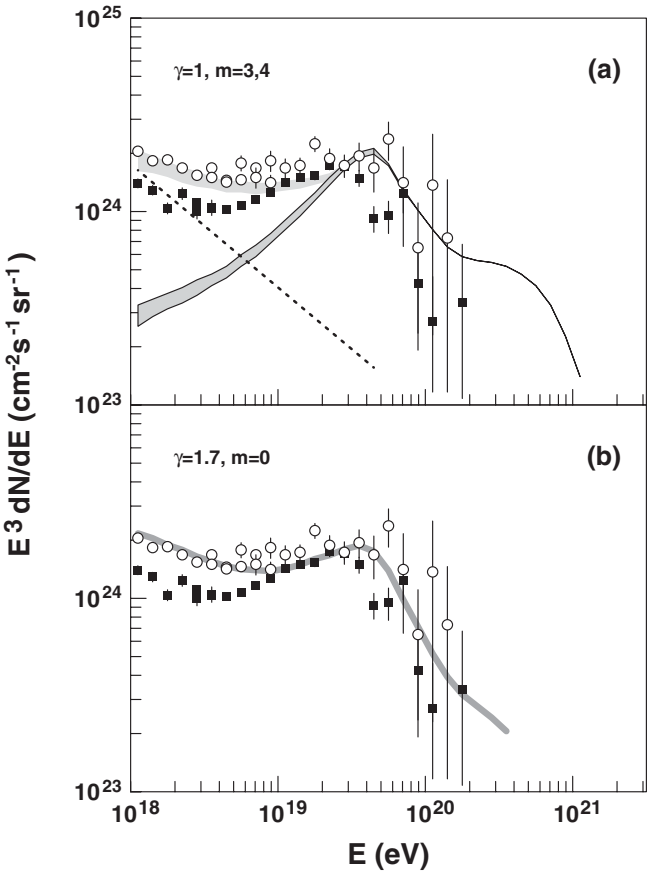

FIG. 21. The models of (a) Bahcall and Waxman (2003) and (b) Berezinsky *et al.* (2006) compared to the more recent data of Auger (full squares) and HiRes (circles).

interaction of the extragalactic protons with CMB as predicted by Berezinsky and Grigor'eva (1988). The model underwent some development later (Aloisio *et al.*, 2007) to convey some of its details. The shocking part of this model, illustrated in the lower panel of Fig. 21, is that the cosmic ray injection spectrum was a steep $E^{-2.7}$ rather than the expected flat one. At about 10^{18} eV, the injection spectrum has to become much flatter for the flux not to exceed the measured cosmic ray spectrum. The transition from galactic to extragalactic cosmic rays should then happen below 10^{18} eV. There is no need for cosmological evolution of the cosmic ray sources in the model. Extragalactic cosmic rays had to be almost exclusively protons.

At about the same time, a third model for the transition became available (Allard *et al.*, 2007) following the calculations of the heavy nuclei propagation in extragalactic space and their interactions with the CMB and other photon fields (Allard *et al.*, 2005; Hooper *et al.*, 2007). Since the extragalactic cosmic rays in such a model may have at least five chemical components, i.e., many more parameters, the model is much more complicated, although it could be made to fit the cosmic ray spectra as well as the first two. These propagation calculations also showed that protons and iron nuclei have approximately equal energy loss lengths, while all intermediate nuclei would disintegrate at much shorter distances.

Since the spectrum shape alone cannot answer the questions about the transition, the answer could only come from an accompanying composition study. The chemical composition derived by the HiRes experiment together with the measurement of Abu-Zayyad *et al.*(2000b) would claim that the galactic cosmic ray spectrum does not extend above 10^{18} eV and higher energies contain only protons with a small admixture of light nuclei. This admixture may be different in the 2005 and 2010 analyses, but it seems to be constant and belong to the same population. Such interpretation may not be consistent with a proton cosmic ray's knee at 3×10^{15} eV or lower as derived by the Kascade experiment, since in such a case the iron knee would start at 10^{17} eV and would leave about 1 order of magnitude of energy unexplained (Hillas, 2005).

A similar simple interpretation of the Auger $X_{\max}$ and RMS result is impossible. The elongation rate derived from the first three points seems to show a quick transition from heavy to light nuclei followed by a slower transition to heavy nuclear composition.

We first have to understand if at least a part of the $X_{\max}$ behavior is not due to a sudden change of hadronic interactions at $\sqrt{s}$ close to 50 TeV, well above the LHC maximum energy. Then we have to relate the change of the injection composition to the shape of the energy spectrum that is in this range quite different from that of HiRes. These are not simple problems to solve, and in our opinion they will take years. The main hope is that Auger and HiRes would examine each others $X_{\max}$ analysis techniques and will come up with similar, if not identical, $X_{\max}$ values as a function of the energy. The lower energy extensions of the UHECR arrays described in Sec. X and the use of different composition related parameters (muon to electron density ratios) may also be of help.

VIII. SEARCH FOR THE SOURCES OF UHECR

Before describing the searches for the sources of UHECR, we briefly introduce some of the ideas about the strengths of the magnetic fields in the Universe. These are important parameters because particle scattering in the magnetic fields can hide the sources. A review of the investigations and results of the studies of astrophysical magnetic fields can be found in Beck (2001).

A. Galactic magnetic fields

Galactic magnetic fields are important for the scattering of UHECR because they definitely have a large-scale structure. This means that cosmic rays coming from the same direction will scatter in a similar way, and the scattering will shift the arrival direction away from the true source.

The regular magnetic field strength is measured mostly by studies of the Faraday rotation of the radio emission of pulsars. The rotation measure RM, measured in rad/m^2, is proportional to $\int_0^d n_e B_\parallel dl$, where d is the distance to the source and n_e is the electron density. The integral over the measured or assumed n_e is used to extract the magnetic field strength as described in a recent review of the galactic magnetic field (Han *et al.*, 2006). In principle, the magnetic field strength is proportional to the matter density in the Galaxy and is decreasing with the galactocentric distance. The field decrease in the galactic plane is best described with an exponential function $e^{-R_{\rm GC}/8.5}$, where the distance from the Galactic center $R_{\rm GC}$ is in kpc. The local regular field in the vicinity of the Solar System has a strength of about 2 μGauss and points counterclockwise close to the direction of the Carina-Sagittarius arm.

This expression is valid for $R_{\rm GC}$ bigger than 3 kpc because the field inside that circle is difficult to study and is not well known. In regions near the Galactic center mGauss fields have been observed pointing almost perpendicular to the galactic plane. This led to suggestions that there is a strong magnetic dipole in the Galactic center. At the Solar System, the dipole field strength is about 0.3 μGauss and points North in galactic coordinates.

The more general estimates of the total field strength at our location give values of 6 μGauss, which results in random field strength twice as large as the regular field. There are also ideas that the random field reaches maximum inside the galactic arms (because of the stellar fields pointing in different directions) and the regular field reaches maximum in the interarm space. The random field is not very important for UHECR scattering because its scale size is only 50–100 pc.

An important question, which is far from solved, is the galactic magnetic halo, i.e., the extension of the magnetic field above and below the galactic plane. More recent measurements tend to show an extended halo that can contribute a lot to the cosmic ray scattering angle (Jiang, *et al.*, 2010). A standard way to study UHECR scattering angle is to inject negatively charged nuclei in a magnetic field model and follow their trajectories until they leave the Galaxy (Stanev, 1997). Such exercises with different toy galactic field models give scattering angles at 100 EeV between 2° and 4° depending on the cosmic ray direction. Some

other estimates, however, give much higher values, up to 10°.[4]

B. Extragalactic magnetic fields

Our knowledge of the extragalactic magnetic fields is much smaller and still on the basic level of the review of Kronberg (1994). Although μGauss magnetic fields have been observed in clusters of galaxies, such objects enclose a small fraction of the Universe (10^{-6} or less) and the upper limit of the average magnetic fields is 10^{-9} Gauss = 1 nGauss if the correlation length of the field L_c is 1 Mpc, the average distance between galaxies. But even such small fields can affect the propagation of UHECR.

The angular deflection due to random walk θ would then be

$$\theta = 2.5° E_{20}^{-1} B_{-9} d_{100} L_C^{1/2}, \tag{23}$$

where E_{20} is the energy in units of 10^{20} eV, B_{-9} is the magnetic field strength in nGauss, d_{100} is the source distance in units of 100 Mpc, and L_C is the correlation length in Mpc. The random walk causes a propagation path length Δd that is larger than the distance to the source and causes increased energy loss. It depends on the square of the parameters above and is

$$\Delta d = 0.047 E_{20}^{-2} B_{-9}^2 d_{100}^2 L_C \text{ Mpc}. \tag{24}$$

The increased propagation distance causes a corresponding time delay. In case UHECR are generated in a GRB, or in an active state of an AGN, we may not be able to correlate these events with the resulting cosmic rays.

The situation changes drastically if the UHECR encounters an extended region with an organized magnetic field. In principle, this should be a rare occasion except close to a powerful astrophysical system where such fields have been observed. Depending on the field strength, its direction toward us, and structure of the field, the angular deflection could be much larger.

C. Correlation of the arrival directions of UHECR with astrophysical objects

The first attempt to correlate the arrival direction of UHECR with known astrophysical objects was by Stanev *et al.* (1995). They used 143 events of energy more than 2×10^{19} eV detected by the Haverah Park array, together with the statistics of the Vulcano Ranch, Yakutsk, and the preliminary data of AGASA. They studied the angular distance between the UHECR events and the supergalactic plane (SGP), which is the plane of weight of almost all extragalactic objects within redshifts below 0.04 (de Vaucouleurs, 1956). The conclusion was that at energy above 4×10^{19} eV, the average and RMS distances of UHECR to SGP are much closer than would be expected from an isotropic distribution of the UHECR sources.

With the increase of the AGASA statistics that started to dominate in the late 1990s, the correlation with the SGP decreased. Other effects were claimed by that experiment: a large-scale isotropy and small-scale anisotropy. The anisotropy was defined by the fact that three pairs and a triple of events coming within 2.5° of each other were found (Takeda *et al.*, 1999) among 47 events of energy above 4×10^{19} eV. The chance probability of this happening from isotropic distribution was less than 1%. Soon after this clustering analysis was extended to include the previously detected events (Uchihori *et al.*, 2000). The conclusions from that analysis were slightly different. Since the angular resolution of the older experiments was worse, the clustering was analyzed in angular distances of 3°, 4°, and 5°. Twelve doubles and 2 triples were found within 3°. The emphasis, though, was on the fact that 8 of the doubles and the 2 triples lie within 10° of the supergalactic plane, which had a chance probability of 0.1% and 0.2% for an isotropic distribution of the sources.

1. Correlation of the Auger events with AGN

After collecting and exposure of 4390 km^2 sr yr, the Auger Collaboration noticed that many of their higher energy events are close to the active galactic nuclei from the VCV (Véron-Cetty and Véron, 2006) catalog. They did a scanning analysis varying the angular distance, event energy, and the source distances. The best correlation appeared for an angular distance of 3.1°, event energy above 5.7×10^{19} eV (57 EeV), and distance of 75 Mpc (redshift less than 0.018). The same analysis was repeated when the exposure more than doubled and the total number of high energy events reached 27. Twenty of these events were within 3.1° of the AGN from the VCV catalog when only 7.4 were expected for isotropic sources. The chance probability for this happening was 1.7×10^{-3} (Abraham *et al.*, 2007b; Abraham *et al.*, 2008a). A significant number of events were close to the nearby (distance of 3.8 Mpc) radio galaxy Cen A. There were no events close to the powerful AGN M87. When the events with galactic latitude less than $\pm 12°$, where the catalog coverage is smaller and UHECR scattering in the galactic magnetic field is supposed to be stronger, were excluded, the strength of the correlation increased and 19 out of 21 events correlated with at least one AGN as shown in Fig. 22. This strong correlation was surprising because of several reasons. First, the VCV optical catalog includes many low power objects that are not likely to accelerate particles to such high energy. Second, the 0.018 redshift does not correspond to the GZK horizon (the distance up to which cosmic ray sources contribute significantly to the flux *observed* above a certain energy) for energy of 57 EeV and the question arose if the Auger energy scale was low by about 25%, which would bring the two distances close to each other.

The Auger Collaboration did not claim that the AGN from the VCV catalog are the actual sources, which may have a sky distribution similar to that of the correlating AGN. The anisotropy of the UHECR sources was emphasized in the papers.

The analysis was repeated by the HiRes experiment (R. U. Abbasi *et al.*, 2008b) as close to the original as possible. There were only two out of 13 events with similar energy that correlated with the same AGNs and the conclusion was the opposite. The HiRes field of view is not the same as that of Auger and the VCV catalog has different coverage of the

[4]R. Beck, private communication

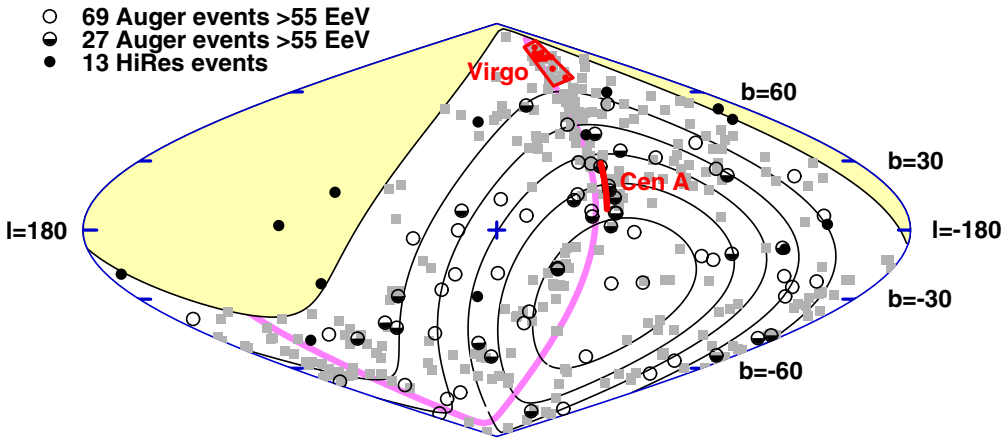

FIG. 22 (color online). Correlation of the arrival directions of UHECR with AGN from the VCV catalog. The shaded part of the sky is not visible by Auger. The gray squares are the AGN within z less than 0.018. The Auger events are shown as circles. The first 27 events are half-filled. The 13 HiRes events are shown with black dots. The thin lines show the six regions of the sky to which Auger has equal exposure. The wide gray line is the supergalactic plane.

corresponding fields of view. Still the results from the two analyses appeared to be controversial since HiRes sees one-half of the Auger field of view.

Recently, the Auger Collaboration presented the correlation results from an exposure of 20 370 $\mathrm{km}^2\,\mathrm{sr\,yr}$ (Abreu *et al.*, 2010), which contains 69 events of energy above 55 EeV (corresponding in the contemporary energy assignment to 57 EeV in 2007). The complete catalog of the 69 Auger events published to date are shown in Fig. 22. The correlation is now weaker -42% of all events (29/69) correlate, compared with 74% in 2007. The event reconstruction is constantly improving and because of that a couple of events move from one group (above 55 EeV or not) to the other. If the events participating in the initial parameter scan are excluded, the corresponding fractions of correlated events are 69% and 38%, respectively. This does not mean, though, that the observed UHECR are isotropically distributed as the expected fraction of correlated events is 21%.

It should be noted that the scattering in the extragalactic magnetic fields should be much stronger according to some calculations. Ryu *et al.* (2010) predicted an average scattering angle of 15° for cosmic ray protons above 60 EeV.

2. Correlation with sources from other catalogs

The most difficult part of the search for UHECR sources is that we have no idea what is the best proxy for cosmic ray acceleration to the highest energy: Is it the optical-UV luminosity, or the x-ray one, or still higher energy γ-ray emissivity? The last paper on the Auger events anisotropy explores the correlations with two more catalogs: the 2MRS catalog (Huchra *et al.*, 2005), which contains the brightest galaxies from the 2 MASS catalog, and the Palermo Swift-BAT hard x-ray catalog (Cusumano *et al.*, 2010). 2MRS contains 13 000 galaxies within 100 Mpc and 22 000 galaxies within 200 Mpc. The Swift-BAT catalog has the advantage to cover well the region of the galactic plane. It contains 133 extragalactic sources within 100 Mpc and 267 within 200 Mpc. The correlation of the Auger UHECR arrival directions with the positions of the objects in both catalogs is much better than an isotropic source distribution would suggest.

To fully understand the correlations with catalogs containing a different number of objects and to estimate the statistical significance of these correlations, the Auger Collaboration used a different approach. The catalogs were used to create maps of possible sources using the object densities per unit area of sky where each object position was extended by several degrees. These extensions are supposed to account for the particle scattering in magnetic fields and the angular sensitivity of the experiment. The UHECR luminosity of the sources were scaled with the distance and with the observed source luminosity at different wavelengths. With the use of simulations, the events were then separated in *source* and *isotropic* fractions with different confidence levels. The isotropic fraction became on the average 0.64 for the 2MRS catalog and 0.62 for Swift-BAT with large error bars even at the 1σ level. In a way, this analysis produced similar results to the contemporary correlation with the VCV catalog.

The last test of isotropy was made with studies of self-correlation—a comparison of the number of event pairs as a function between the angular distance of the pair compared to that of isotropic source distribution. The number of experimental pair events is consistently above the expectations. The largest deviation is at an angular distance of 11°, where the experimental events show 51 pairs while 34.8 pairs are expected for an isotropic distribution. At angular distances higher than 45°, the number of pairs is consistent with isotropy but below 30° it is not.

3. Events coming from specific objects

Ever since the publication of the first correlation analysis of the Auger events with extragalactic objects, the question was why there are so many events coming from directions close to Cen A and there are none from the Virgo cluster and M87. With the increased contemporary statistics, Auger was able to better analyze this fact. There are still no events coming from less than 18° from M87. And there are now 13 events coming from less than 18° from Cen A and two events very close to it. Cen A is close to the direction of the Centaurus cluster but is not a part of it.

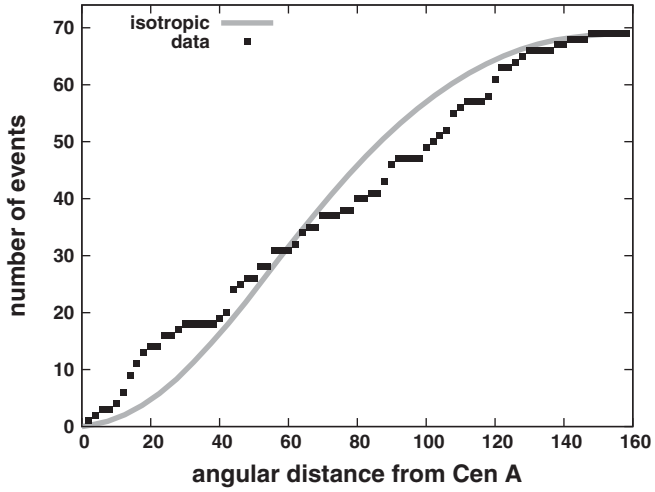

FIG. 23. Number of events as a function of the angular distance to Cen A. The thick gray line shows the expectation from isotropic distribution of the cosmic ray sources.

M87 is almost 5 times more distant than Cen A, which is at a distance of 3.8 Mpc. It is also in a region where the Auger exposure is 3 times less as shown in Fig. 22. Using these two rough numbers, one expects 75 times less events from M87 than from Cen A. In other words, one expects 13/75 events coming from M87 if it has the same CR luminosity as Cen A. The lack of events then is not a problem.

The 13 events coming from directions close to Cen A are mostly responsible for the excess of self-correlation discussed above. The events coming from this direction have 28 pairs coming with separation less than 11°. For an isotropic distribution one expects 3.2 events rather than 13, while the map based on the 2MRS catalog predicts 9.2 and that based on Swift-BAT catalog predicts 20.6.

Figure 23 shows the comparison of the number of events coming at different distances from this object compared to the expectations from an isotropic distribution. A Kolmogorov-Smirnov test of these distributions establishes 96% significance or about 2σ deviation from an isotropic distribution. The question then is if at least a part of these events come from the Centaurus cluster rather than from Cen A. This does not appear likely because the Centaurus cluster is further away than Virgo and one would expect a small fraction of events coming from there for equal CR luminosities, which is of course not guaranteed.

IX. ULTRAHIGH ENERGY NEUTRINOS

The relationship between UHECR and ultrahigh energy neutrinos was first noted by Berezinsky and Zatsepin (1969). Later on, an important relation between the observed UHECR flux and the flux of diffuse neutrino was derived (Waxman and Bahcall, 1998). They took a simple basic approach to the problem and using the measured cosmic ray flux at 10^{19} eV. Then they assumed a flat, $\gamma = 2$ injection spectrum and calculated the emissivity of UHECR in the Universe, which came to 10^{44} ergs/(Mpc^3 yr) in the range 10^{19}–10^{21} eV. The next observation is that a fraction of these cosmic rays would have photoproduction interaction at their sources and a fraction of their energy loss ϵ would go to neutrinos. The upper

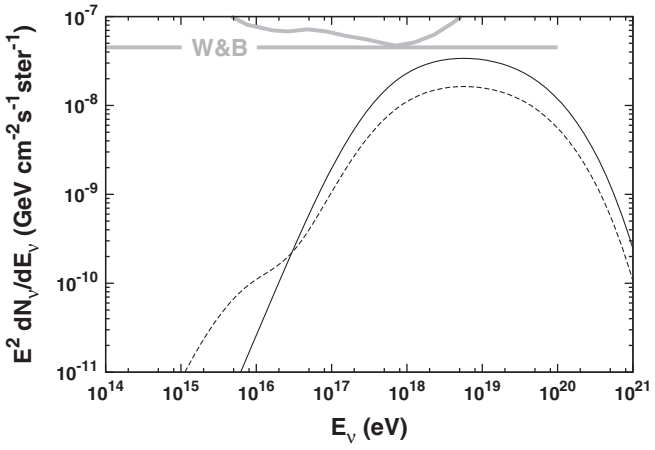

FIG. 24. The upper limits on the ultrahigh energy neutrino fluxes derived by Waxman and Bahcall (1998) (labeled) and Mannheim *et al.* (2000) are compared to a calculation of cosmogenic neutrinos produced by UHE protons by Engel *et al.* (2001). Electron neutrinos and antineutrino fluxes are plotted with a dashed line. One can see the contribution of neutron decay at lower energy.

bound of the ultrahigh energy muon neutrinos and antineutrinos would be reached if UHECR lost all of their energy in production of neutrinos. Using the average energy loss, they arrived at an upper bound of

$$E_\nu^2 dN_\nu/dE_\nu = 1.5 \times 10^{-8}\ \mathrm{GeV(cm^2\,s\,sr)^{-1}}, \tag{25}$$

which after accounting for the cosmological evolution of the sources as $(1+z)^3$ is increased by a factor of 3. The limit was criticized by Mannheim *et al.*(2000) who derived a more realistic limit that only touched the limit of Waxman and Bahcall at 10^{18} eV. Both limits are shown as thick gray lines in Fig. 24.

Cosmogenic neutrinos were first suggested by Berezinsky and Zatsepin (1969). These are neutrinos that are produced by UHECR in photoproduction interactions in the CMB and other photon fields in propagation. The original paper did not produce much interest since the contemporary experiments could not detect high energy neutrinos. The shapes of the cosmogenic neutrino spectra are very different from those of the Waxman and Bahcall limit. Muon neutrino and antineutrino spectra peak at about 10^{18} eV and significantly decline at both lower and higher energy. These spectra are shown in Fig. 24 together with the two limits assuming the same astrophysical input. Even after the multiplication by E_ν^2 the electron neutrino and antineutrino spectra show an extension to lower energy which is due to $\bar{\nu}_e$ from neutron decay.

The magnitude of the cosmogenic neutrino spectra depends on the cosmic ray injection spectrum and composition, on the distribution of UHECR sources, and very strongly on the cosmological evolution of these sources. For flatter injection spectra, more UHECR can undergo photoproduction interactions and hence generate more neutrinos. Cosmological evolution importance has a simple explanation—UHECR can arrive to us only from very low redshifts (less than 0.05) while neutrinos can travel without energy loss (except adiabatic) from the whole Universe. If the cosmological evolution of the UHECR sources peaks at $z = 2$, as it does in many models,

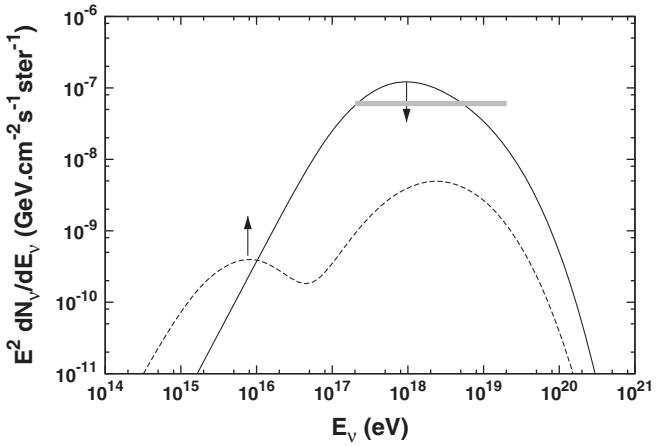

FIG. 25. Neutrino fluxes calculated from the Auger energy spectrum interpretation that produces the larger amount of cosmogenic neutrinos. The solid line shows the sum of $\nu_\mu + \bar{\nu}_\mu + \nu_e$. The dash-dottted line shows the flux of $\bar{\nu}_e$. Any heavier nuclei contribution to the UHECR flux can only raise the dash-dotted line and decrease the solid one. The thick gray line shows the median (halfway between optimistic and pessimistic) limit set by Auger on ν_τ.

the cosmogenic neutrino production would peak close to $z = 3$, when the source emission is much stronger.

The influence of the cosmic ray composition on the cosmogenic neutrino flux is even stronger, although more difficult to evaluate. Figure 25 shows the fluxes of cosmogenic neutrinos calculated for UHE protons. The solid line shows the sum of muon neutrinos and antineutrinos and electron neutrinos and the dash-dotted line shows the flux of electron antineutrinos from neutron decay. The input parameters come from the Auger energy spectrum fit that produces the larger amount of cosmogenic neutrinos [protons, $\gamma = 1.3$, cosmological evolution $(1 + z)^5$]. If UHECR are not all protons, the solid line should come down keeping all other parameters stable. For 20% protons in UHECR, the flux would be lower by a factor of 5. At the same time, the flux of cosmogenic $\bar{\nu}_e$ would rise since heavy nuclei photodisintegrate and emit neutrons that decay. The estimate of the increase of the $\bar{\nu}_e$ flux is more complicated, but it would increase roughly also by a factor of 5. The cosmogenic neutrino flux would then be dominated at production by this neutrino flavor. After propagation it would be shared equally by all three neutrino flavors.

The conclusion is that a measurement of the cosmogenic neutrino flux is a complementary measurement to that of the UHECR spectrum and composition. Even the detection of a few events will considerably help the analysis of the UHECR features and origin. The problem here is that the current limits on the UHE neutrino fluxes are generally above the predictions shown in Fig. 25. The measurement of the cosmogenic $\bar{\nu}_e$ spectra and their oscillations is even more difficult because of the energy dependence of the neutrino-nucleon cross section.

X. REMAINING PROBLEMS AND EXPECTATIONS FROM FUTURE EXPERIMENTS

A. Remaining problems

It is obvious from the controversial results on the chemical composition of UHECR that this is the main unsolved problem. The uncertainty of the chemical composition also affects the interpretation of the end of the cosmic ray energy spectrum. If the UHECR composition is dominated by protons, the most likely explanation is the GZK effect. If, however, the composition is increasingly heavier to the highest energies, it could be a result of reaching the maximum acceleration rigidity at the UHECR sources.

At the highest energies (above a few tens of EeV) two important observables need to be measured with better precision, the composition and the anisotropies. Both will tell us about the sources and their distribution as well as about the mechanisms at play in accelerating particles up to 100 EeV or more.

Currently, the available data from Auger and HiRes appear contradictory and no model is able to explain in a coherent way all the observations. Moreover, in the Auger data Centaurus A is today the sole possible source candidate that may have been seen in the sky. Can this possibility be confirmed? Is Cen A the only source visible from the Southern hemisphere; from both hemispheres?

At the highest energies, the effort needs to be pursued along at least three lines: covering the whole sky, increasing the statistics by instrumenting larger surfaces or volumes, and improving the measurements adding new detector components. To make definite progress, the next generation of detectors should be able to measure independently, and if possible redundantly, all EAS components. This includes, in particular, an electromagnetic shower profile with a maximum of a few tens of g/cm^2 resolution, as well as the muonic and electromagnetic components at ground to better constrain the hadronic model and the first interaction dynamics.

At the EeV scale, the expected transition from galactic to extragalactic origin in the cosmic ray spectrum has not been confirmed. Several features in the energy spectrum need attention. Is there a second knee around 0.1 EeV or at almost 1 EeV as measured by the Akeno array (Nagano *et al.*, 1992)? How pronounced is the ankle? What is its origin? Today the interpretations in terms of a pure proton composition undergoing e^+e^- pair creations, or in terms of the galactic to extra galactic transition of a mixed composition seem equally (in) valid. What is the level of anisotropy in this energy range? Can the above models accommodate or predict the low values already reported (Abraham *et al.*, 2009e)? Again the only hope for light can come from more accurate measurements of this regions, both in terms of statistics and in terms of multiparametric observations.

B. Extensions of Auger South

The High Elevation Auger Telescope (HEAT) (Kleifges *et al.*, 2009) and the Auger Muon and Infill for the Ground Array (AMIGA) (Platino *et al.*, 2009) have been added to the original design of the Pierre Auger Observatory. Improving the efficiency of the observatory in the 0.1 to 1 EeV range, these extensions will efficiently test the various models for the acceleration and transport of galactic and extragalactic cosmic rays in the transition region.

Studies of this region require not only a better collection efficiency to improve the statistics, but also powerful mass discrimination capabilities. While very high energy showers

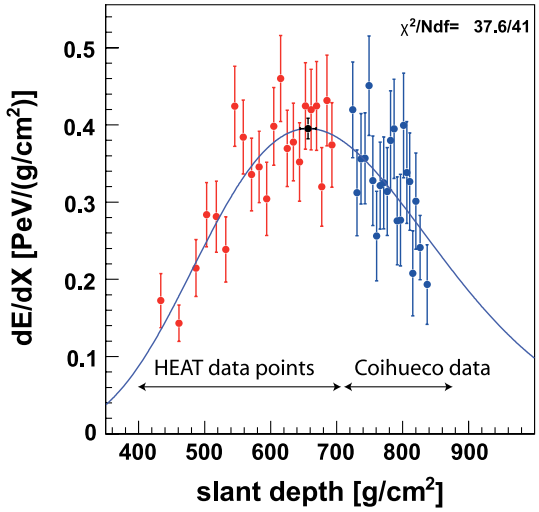

FIG. 26 (color online). Longitudinal profile of a 0.2 ± 0.02 EeV shower recoded in coincidence by the HEAT and Coihueco fluorescent telescope of the Auger observatory.

can be efficiently measured by fluorescent telescopes from distances up to several tens of kilometers, lower energy ones do not emit sufficient light to be seen further than a few kilometers away. For the same position of $X_{\max}$, closer showers appear at higher elevation than distant ones. Since low energy showers reach their maximum of development faster, coverage above the 30° limit of the original Auger telescopes is required. HEAT is composed of three fluorescent telescopes of the same basic design as the original Auger telescope and is installed at the western fluorescent detector site (Coihueco) of the observatory. They can operate in two positions. Horizontally, they share the same field of view as the original telescopes. This position is used for laser and drum calibration of the instruments, as well as for intercalibration using shower data. Tilted upward by 29°, this is the normal operation mode in which the nearby upper part of the atmosphere is observed. Construction took place in 2008 to 2009 and first light was seen from one of those telescopes in January 2009.

Routine observation with the HEAT telescope began in 2010. Figure 26 shows the longitudinal shower profile of an event recorded in coincidence with the Coihueco telescope. The reconstruction of this event gives a shower energy of 0.2 ± 0.02 EeV and a distance of 2.83 ± 0.06 km from Coihueco. It is clear from the plot that the data points provided by the HEAT telescope are mandatory to properly reconstruct the shower development profile.

The Auger observatory reconstruction is based on the hybrid technique. To provide the HEAT telescope with adequate information from the surface array, it was necessary to also increase the surface detector density at the foot of the telescope. An infill array of 85 detectors is deployed on two grids of one-half (750 m) and one-fourth (433 m) of the regular Auger surface array grid. Measuring the muon densities on the ground together with the electromagnetic component provides important information on the cosmic ray composition in addition to the longitudinal shower development. Such a multiparametric measurement allows one to study independently the evolution of $X_{\max}$ and the muon densities, which are linked in a similar way in all interaction models. The AMIGA extension aims to provide such information by measuring the shower muons with buried muon counters. Each counter is made of a segmented plastic scintillator read out by wave shifting fibers connected to a 64 channels multianode PMT.

The muon lateral distribution function is adjusted to the counter data to provide the number of muons at 600 m from the shower axis. Realistic Monte Carlo analysis together with an improved reconstruction showed a relative precision on the estimated muon density better than 20% in the energy range of 0.4 to 3 EeV accessible to the 750 m infill alone (Supanitsky *et al.*, 2008).

Currently, nearly all of the 750 m infill grid is completed and is operating while a muon counter has been buried and successfully tested. Completion of this effort is expected to take place in 2011 to 2012.

Finally, colocated with the infill array, the Auger collaboration is currently installing the first phase of the Auger Engineering Radio Array (AERA, (van den Berg *et al.*, 2009). The base line parameters for AERA comprise about 150 radio-detection stations distributed over an area of 20 km^2. The main scientific goals of the project are a thorough investigation of the radio emission from an air shower at the highest energies, the exploration of the capability of the radio-detection technique, and the provision of additional observables (calorimetric energy and shower profile determination with 100% duty cycle) for the composition measurements between $10^{17.4}$ and $10^{18.7}$ eV

In order to increase the amount of data on the shower longitudinal development, today severely limited by the 10% duty cycle of the fluorescent detector, the Auger Collaboration is pursuing several research and development programs aiming at measuring the shower longitudinal development using microwave radio techniques (P. W. Gorham *et al.*, 2008; Gambetta *et al.*, 2010; Privitera *et al.*, 2010).

C. Telescope Array

The Telescope Array (TA) is a new hybrid detector that started collecting data in 2009 in Utah, USA, at 39°N, 120°W and altitude of 1500 m above sea level. Its surface array (SD) currently consists of 607 scintillator counters on a square grid with a dimension of 1.2 km. Each scintillator detector consists of two layers of thickness, 1.2 cm and an area of 3 m^2. The phototube of each layer is connected to the scintillator via 96 wavelength shifting fibers which make the response of the scintillator more uniform. Each such station is powered by a solar panel that charges a lead-acid battery. The total area of the surface array is 762 km^2. The surface array is divided into three parts that communicate with three control towers where the waveforms are digitized and triggers are produced. Each second the tower collects the recorded signals from all stations and a trigger is produced when three adjacent stations coincide within 8 μ sec . The SD reaches a full efficiency at $10^{18.7}$ eV for showers with zenith angle less than 45° (Nonaka *et al.*, 2009). This angle corresponds to SD acceptance of 1600 km^2 sr.

The FD consists of three fluorescent stations, as shown in Fig. 27. Two of them are new and consist of 12 telescopes

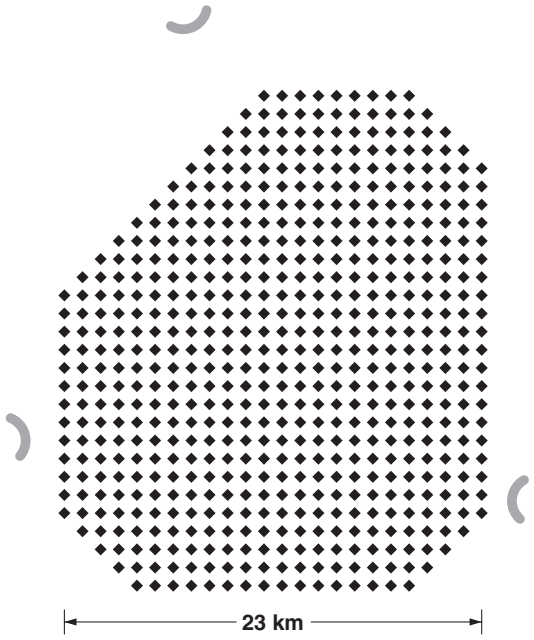

FIG. 27. Sketch of the telescope array geometry. The surface detectors are indicated with full diamonds and the telescope stations with arcs.

with a field of view from elevations of 3° to 31°. The total horizontal field of view of each station is 108°. Each telescope has a camera consisting of 256 PMT with field of view 1° × 1°. The signals are digitized by a 40 MHZ sample fast analog to digital converter and the waveforms are recorded when signals are found in 5 adjacent PMTs. The third station has 14 telescopes that use cameras and electronics from HiRes-I and mirrors from HiRes-II. The fluorescent telescopes are calibrated with lasers, Xe flashers, and an electron linear accelerator (Tokuno *et al.*, 2009).

The atmosphere is monitored for clouds by IR cameras and with the use of the central laser facility, which is in the center of the array at 20.85 km from each station. The fluorescent stations are positioned in such a way that they cover the whole area of the surface detector. The mono acceptance of the FD is 1830 km^2 sr and the stereo one is 1040 km^2 sr. The total energy resolution is 25% and the X_{max} resolution is 17 g/cm^2.

The lower energy extension of the Telescope Array (TALE), which will be deployed to study cosmic rays of energy $10^{16.5}$ to 10^{18} eV. It consists of an infill array and a fourth fluorescent station inside TA. The field of view of this station will be elevations of 33° to 71° so it will be able to see X_{max} of the lower energy showers. The infill will consist of 100 scintillator counters on a square grid of 400 m and muon counters.[5] .

D. Auger North

Based on the same detection principle as the southern observatory, the design of the northern site of Auger (Auger North) is focussed on collecting significantly larger statistics (Bluemer *et al.*, 2010). Its target energy lies above the 60 EeV threshold where anisotropy in the distribution of cosmic ray sources within the GZK sphere has been detected. Motivation for such a detector are plenty; they principally concern the determination of the cosmic ray composition up to at least 100 EeV. This would lead, on the one hand, to the identification of the trans-GZK cosmic ray sources and their acceleration mechanisms and, on the other hand, to the study of particle interactions at center of mass energies far beyond any man made accelerators.

Covering 20 000 km^2, this new facility is to be deployed in the state of Colorado (USA) in the northern hemisphere to provide the Auger collaboration with full sky coverage. Composed of a particle array of 4000 Cherenkov tanks principally on a $\sqrt{2}$ miles grid and 39 fluorescent telescopes overlooking the atmosphere over the whole array. This configuration should reach 90% efficiency above 30 EeV for proton primaries.

The expected performances of this detector are similar to its southern counterpart, but at a higher energy due to the larger spacing. For example, the angular resolution is expected to be better than 2.2° above 50 EeV. The statistics above 60 EeV are expected to be of the order of 150 events per year. Out of those, of order of 10 per year should have an appropriate profile reconstruction from the FD telescopes for mass composition measurements.

Construction of this facility was planned for 2011 and should last 5 years. However, as of the end of 2010, the funding situation and prioritization in the USA does not allow for such construction to start in the short term.

E. EUSO—JEM-EUSO

The Extreme Universe Space Observatory (EUSO) is an UV telescope mounted on an external facility of the International Space Station (ISS) which observes the atmosphere to detect light signals from UHE cosmic rays and neutrinos. It is a monocular telescope that measures the air-shower fluorescent light and the Cherenkov light diffusively reflected from the surface of the Earth. The initial idea of such an experiment was proposed and developed by the pioneer of the UHECR research, John Linsley (1998). He was later joined by Livio Scarsi and a group of scientists from the University of Palermo. Initially, EUSO was approved by the European Space Agency for a phase A conceptual study (Catalano *et al.*, 2000). It was not approved to be mounted on the European research module of ISS and was taken over by the Japanese Space Agency. It is now known as JEM-EUSO.

EUSO is a wide angle (± 30°) camera with a diameter of 2.5 m. The UV light is imaged through the Fresnel lens optics and detected by a segmented focal surface detector using multianod PMT. The aim is to have 1 km^2 resolution on the surface of the Earth, which provides an angular resolution of 2.5°. The surface area covered on the Earth is about 160 000 km^2. The duty cycle of EUSO will be similar to that of surface fluorescent telescopes, of order of 10%. The plan is to have JEM-EUSO looking straight down and also in a tilted mode that will increase the viewing area by a factor up to 5, but decrease its resolution. EUSO will

[5]See its description at http://www.telescope array.org

also be equipped with devices that measure the transparency of the atmosphere and the existence of clouds. Clouds are not always bad for such a detector because some shower signals could be reflected by them and detected better by the instrument.

The motivation for EUSO is the study of cosmic rays of energy above 5×10^{19} eV as well as very high energy neutrinos (Ebisuzaki, 2008).

Currently, JEM-EUSO is the second experiment to be launched to the Japanese Experimental Module of ISS in 2015. The launch will be provided by the Japanese transfer vehicle HTV.

ACKNOWLEDGMENTS

We acknowledge extended discussions with D. Allard, P. Billoir, R. Engel, T. K. Gaisser, A. Olinto, P. Sokolsky, M. Unger, A. A. Watson, and others. Special thanks to C. Dobrigkeit, P. Ghia, and A. A. Watson for the careful reading of the manuscript and their comments. A. L. S. thanks the whole Auger Collaboration. T. S. is grateful to LPNHE/UPMC-CNRS/IN2P3 for their support of his visit to Paris University Pierre et Marie Curie in 2009. The work of T. S. is supported in part by the U.S. Department of Energy Grant No. UD-FG02-91ER40626.

REFERENCES

Abbasi, R. *et al.* (HiRes Collaboration), 2007, Astropart. Phys. **27**, 370.
Abbasi, R. *et al.* (HiRes Collaboration), 2008, Phys. Rev. Lett. **100**, 101101.
Abbasi, R. U. *et al.* (HiRes Collaboration), 2004, Phys. Rev. Lett. **92**, 151101.
Abbasi, R. U. *et al.* (HiRes Collaboration), 2005a, Astropart. Phys. **23**, 157.
Abbasi, R. U. *et al.* (HiRes Collaboration), 2005b, Astrophys. J. **622**, 910.
Abbasi, R. U. *et al.* (HiRes Collaboration), 2005c, Phys. Lett. B **619**, 271.
Abbasi, R. U. *et al.* (HiRes Collaboration), 2008a, Astrophys. J. **684**, 790.
Abbasi, R. U. *et al.* (HiRes Collaboration), 2008b, Astropart. Phys. **30**, 175.
Abbasi, R. U. *et al.* (HiRes Collaboration), 2009, Astropart. Phys. **32**, 53.
Abbasi, R. U. *et al.* (HiRes Collaboration), 2010, Phys. Rev. Lett. **104**, 161101.
Abdo, A. A. *et al.* (Fermi LAT Collaboration), 2009, Astrophys. J. Suppl. Ser. **183**, 46.
Abraham, J. *et al.* (Pierre Auger Collaboration), 2004, Nucl. Instrum. Methods Phys. Res., Sect. A **523**, 50.
Abraham, J. *et al.* (Pierre Auger Collaboration), 2007a, Astropart. Phys. **27**, 155.
Abraham, J. *et al.* (Pierre Auger Collaboration), 2007b, Science **318**, 938.
Abraham, J. *et al.* (Pierre Auger Collaboration), 2008a, Astropart. Phys. **29**, 188.
Abraham, J. *et al.* (Pierre Auger Collaboration), 2008b, Phys. Rev. Lett. **101**, 061101.
Abraham, J. *et al.* (Pierre Auger Collaboration), 2008c, Astropart. Phys. **29**, 243.
Abraham, J. *et al.* (Pierre Auger Collaboration), 2008d, Phys. Rev. Lett. **100**, 211101.
Abraham, J. *et al.* (Pierre Auger Collaboration), 2009a, Astropart. Phys. **32**, 89.
Abraham, J. *et al.* (Pierre Auger Collaboration), 2009b, Phys. Rev. D **79**, 102001.
Abraham, J. *et al.* (Pierre Auger Collaboration), 2009c, in *Proceedings of the 31st ICRC, Lodz, Poland* (University of Lodz, Lodz, Poland).
Abraham, J. *et al.* (Pierre Auger Collaboration), 2009d, Astropart. Phys. **31**, 399.
Abraham, J. *et al.* (Pierre Auger Collaboration), 2009e, in *Proceedings of the 31st ICRC, Lodz, Poland* (University of Lodz, Lodz, Poland).
Abraham, J. *et al.* (Pierre Auger Collaboration), 2010a, Nucl. Instrum. Methods Phys. Res., Sect. A **620**, 227.
Abraham, J. *et al.* (Pierre Auger Collaboration), 2010b, Astropart. Phys. **33**, 108.
Abraham, J. *et al.* (Pierre Auger Collaboration), 2010c, Phys. Rev. Lett. **104**, 091101.
Abraham, J. *et al.* (Pierre Auger Collaboration), 2010d, Phys. Lett. B **685**, 239.
Abraham, J. *et al.* (Pierre Auger Collaboration), 2010e, Nucl. Instrum. Methods Phys. Res., Sect. A **613**, 29.
Abreu, P. *et al.* (Pierre Auger Collaboration), 2010, Astropart. Phys. 34, 314.
Abu-Zayyad, T. *et al.*, 1999, in *Proceedings of the 26th ICRC, Salt Lake City, USA* (University of Utah, Salt Lake City, Utah), Vol. 5, p. 349.
Abu-Zayyad, T. *et al.*, 2000a, Nucl. Instrum. Methods Phys. Res., Sect. A **450**, 253.
Abu-Zayyad, T. *et al.*, 2000b, Phys. Rev. Lett. **84**, 4276.
Abu-Zayyad, T. *et al.*, 2001, Astropart. Phys. **16**, 1.
Achterberg, A., Y. A. Gallant, J. G. Kirk, and A. W. Guthmann, 2001a, Mon. Not. R. Astron. Soc. **328**, 393.
Achterberg, A., Y. A. Gallant, J. G. Kirk, and A. W. Guthmann, 2001b, Mon. Not. R. Astron. Soc. **328**, 393.
Achterberg, A. *et al.* (IceCube Collaboration), 2007, Phys. Rev. D **76**, 042008.
Aglietta, M. *et al.* (EAS-TOP Collaboration), 2004, Astropart. Phys. **21**, 583.
Aharonian, F. *et al.* (HESS Collaboration), 2006a, Nature (London) **439**, 695.
Aharonian, F. *et al.* (HESS Collaboration), 2006b, Astrophys. J. **636**, 777.
Ahn, E.-J., R. Engel, T. K. Gaisser, P. Lipari, and T. Stanev, 2009, Phys. Rev. D **80**, 094003.
Ahn, H. *et al.*, 2010, Astrophys. J. **714**, L89.
Allan, H. R., 1977, in *Proceedings of the 15th ICRC, Plovdiv, Bulgaria* (Bulgarian Academy of Sciences, Sofia, Bulgaria), Vol. 10, p. 414.
Allard, D., E. Parizot, E. Khan, S. Goriely, and A. V. Olinto, 2005, Astron. Astrophys. **443**, L29.
Allard, D., E. Parizot, and A. V. Olinto, 2007, Astropart. Phys. **27**, 61.
Allekotte, I. *et al.* (Pierre Auger Collaboration), 2008, Nucl. Instrum. Methods Phys. Res., Sect. A **586**, 409.
Aloisio, R., V. Berezinsky, and A. Gazizov, 2009, arXiv:0907.5194.
Aloisio, R. *et al.*, 2007, Astropart. Phys. **27**, 76.
Alvarez-Muñiz, J., R. Engel, T. K. Gaisser, J. A. Ortiz, and T. Stanev, 2002, Phys. Rev. D **66**, 033011.
Amenomori, M. *et al.* (TIBET III Collaboration), 2008, Astrophys. J. **678**, 1165.
Antoni, T. *et al.* (KASCADE Collaboration), 2005, Astropart. Phys. **24**, 1.

Apel, W. D. *et al.*, 2008, Astropart. Phys. **29**, 412.
Ardouin, D. *et al.* 2006, Int. J. Mod. Phys. A **21S1**, 192.
Arqueros, F., F. Blanco, and J. Rosado, 2009, New J. Phys. **11**, 065011.
Arqueros, F., J. R. Hoerandel, and B. Keilhauer, 2008, Nucl. Instrum. Methods Phys. Res., Sect. A **597**, 23.
Arqueros, F. *et al.*, 2000, Astron. Astrophys. **359**, 682.
Ave, M., J. A. Hinton, R. A. Vazquez, A. A. Watson, and E. Zas, 2002, Phys. Rev. D **65**, 063007.
Ave, M. *et al.* (AIRFLY Collaboration), 2008, Nucl. Instrum. Methods Phys. Res., Sect. A **597**, 46.
Axford, W., E. Lear, and G. Skadron, 1977, in *Proceedings of the 17th ICRC (Plovdiv, Bulgaria)* (Bulgarian Academy of Sciences, Sofia, Bulgaria), Vol. 11, p. 132.
Bahcall, J. N., and E. Waxman, 2003, Phys. Lett. B **556**, 1.
Baltrusaitis, R. *et al.*, 1985, Nucl. Instrum. Methods Phys. Res., Sect. A **240**, 410.
Beatty, J., and S. Westerhoff, 2009, Annu. Rev. Nucl. Part. Sci. **59**, 319.
Beck, R., 2001, Space Sci. Rev. **99**, 243.
Bell, A. R., 1978, Mon. Not. R. Astron. Soc. **182**, 443.
Bell, A. R., 2004, Mon. Not. R. Astron. Soc. **353**, 550.
Berezhko, E. G., 1996, Astropart. Phys. **5**, 367.
Berezinsky, V., 1999, Nucl. Phys. B, Proc. Suppl. **70**, 419.
Berezinsky, V., P. Blasi, and A. Vilenkin, 1998, Phys. Rev. D **58**, 103515.
Berezinsky, V., A. Gazizov, and S. Grigorieva, 2006, Phys. Rev. D **74**, 043005.
Berezinsky, V. S., and S. I. Grigor'eva, 1988, Astron. Astrophys. **199**, 1.
Berezinsky, V. S., and G. T. Zatsepin, 1969, Phys. Lett. B **28**, 423.
Bergeson, H. *et al.*, 1977, Phys. Rev. Lett. **39**, 847.
Bertou, X., P. Billoir, O. Deligny, C. Lachaud, and A. Letessier-Selvon, 2002, Astropart. Phys. **17**, 183.
Bhattacharjee, P., 1998, in *Workshop on Observing Giant Cosmic Ray Air Showers From 10(20) eV Particles From Space*, AIP Conf. Proc. No. 433 (AIP, New York), p. 168.
Bhattacharjee, P., and G. Sigl, 2000, Phys. Rep. **327**, 109.
Bird, D. J. *et al.* (HiRes Collaboration), 1993, Phys. Rev. Lett. **71**, 3401.
Blandford, R., and D. Eichler, 1987, Phys. Rep. **154**, 1.
Blandford, R. D., and J. P. Ostriker, 1978, Astrophys. J. **221**, L29.
Bluemer, J., R. Engel, and J. R. Hoerandel, 2009, Prog. Part. Nucl. Phys. **63**, 293.
Bluemer, J. *et al.* (Pierre Auger Collaboration), 2010, New J. Phys. **12**, 035001.
Bonifazi, C., A. Letessier-Selvon, and E. M. Santos (Pierre Auger Collaboration), 2008, Astropart. Phys. **28**, 523.
Bonifazi, C. *et al.* (Pierre Auger Collaboration), 2009, Nucl. Phys. B, Proc. Suppl. **190**, 20.
Borione, A. *et al.*, 1994, Nucl. Instrum. Methods Phys. Res., Sect. A **346**, 329.
Boyer, J. H. *et al.*, 2002, Nucl. Instrum. Methods Phys. Res., Sect. A **482**, 457.
Brennan, M. H. *et al.*, 1958, Nature (London) **182**, 973.
Bunner, A. N., 1967, Ph. D. Thesis (Cornell University).
Bunner, A. N. *et al.*, 1967, Sky and Telescope, **34**, 204.
Calvez, A., A. Kusenko, and S. Nagataki, 2010, Phys. Rev. Lett. **105**, 091101.
Capelle, K., J. Cronin, G. Parente, and E. Zas, 1998, Astropart. Phys. **8**, 321.
Cassidy, M. *et al.*, 1997, in *Proceedings of 25th ICRC (Durban, South Africa)* (Potchestroomse Universiteit, Potacefstroom, South Africa), Vol. 5, p. 189.
Catalano, O. *et al.*, 2000, Nucl. Phys. B, Proc. Suppl. **80**, C804.
Chernov, D. *et al.*, 2006, Int. J. Mod. Phys. A **20**, 6977.
Chiba, N. *et al.*, 1992, Nucl. Instrum. Methods Phys. Res., Sect. A **311**, 338.
Chou, A. S., M. D. A. Pernas, and T. Yamamoto (Pierre Auger Collaboration), 2005, in *Proceedings of the 29th ICRC, Pune, India* (Tata Itstitute for Fundamental Research, Mumbai, India), Vol. 7, p. 323.
Chudakov, A. E. *et al.*, 1960, in *Proceedings of the 6th ICRC Conference (Moscow, Russia)*, Vol. 2, 47.
Cronin, J. W., 1999, Rev. Mod. Phys. **71**, S165.
Cusumano, G. *et al.*, 2010, Astron. Astrophys. **510**, A48+.
de Vaucouleurs, G., 1956, Vistas Astron. **2**, 1584.
Dickinson, J. E. *et al.*, 1999, in *Proceedings of the 26th ICRC (Salt Lake City, USA)* (University of Utah, Salt Lake City, Utah), Vol. 3, p. 136.
Drury, L. O., 1983, Rep. Prog. Phys. **46**, 973.
Drury, L. O., F. A. Aharonian, and H. J. Volk, 1994, Astron. Astrophys. **287**, 959.
Ebisuzaki, T. (EUSO Collaboration), 2008, J. Phys. Soc. Jpn., Suppl. B **77**, 88.
Efimov, N. N. *et al.*, 1991, in *Proceedings of the International Symposium of Astrophysical Aspects of Most Energetic Cosmic Rays* (World Scientific, Singapore), p. 20.
Engel, R., D. Seckel, and T. Stanev, 2001, Phys. Rev. D **64**, 093010.
Fermi, E., 1949, Phys. Rev. **75**, 1169.
Fowler, J. W. *et al.*, 2001, Astropart. Phys. **15**, 49.
Gaisser, T., and A. Hillas, 1977, in *Proceedings of the 15th ICRC, Plovdiv, Bulgaria* (Bulgarian Academy of Sciences, Sofia, Bulgaria), Vol. 8, p. 353.
Gaisser, T. K. *et al.* (HiRes Collaboration), 1993, Phys. Rev. D **47**, 1919.
Gambetta, S. *et al.*, 2010, in *Proceedings of the 7th Air Fluorescence Workshop, Coimbra, Portugal* (University of Coimbra, Coimbra, Portugal).
Giller, M., G. Wieczorek, A. Kacperczyk, H. Stojek, and W. Tkaczyk, 2004, J. Phys. G **30**, 97.
Ginzburg, V. L., and S. I. Syrovatskii, 1964, *The Origin of Cosmic Rays* (MacMillan, London).
Glushkov, A. *et al.* 2010, Phys. Rev. D **82**, 041101.
Gorham, P. *et al.*, 2008, Phys. Rev. D **78**, 032007.
Gorham, P. W. *et al.*, 2008, Phys. Rev. D **78**, 032007.
Green, D. A., 2009, Bulletin of the Astronomical Society of India **37**, 45.
Greisen, K., 1956, Progress in Cosmic Ray Physics, **3**, 1.
Greisen, K., 1960, Annu. Rev. Nucl. Sci. **10**, 63.
Greisen, K., 1966, Phys. Rev. Lett. **16**, 748.
Halzen, F., and E. Zas, 1997, Astrophys. J. **488**, 669.
Han, J. L., R. N. Manchester, A. G. Lyne, G. J. Qiao, and W. van Straten, 2006, Astrophys. J. **642**, 868.
T. Hara, *et al.*, 1970, Acta Physica Academiae Scientiarum Hungaricae **29**, 361.
Haungs, A. *et al.* (LOPES Collaboration), 2009, Nucl. Phys. B, Proc. Suppl. **196**, 297.
Heitler, W., 1954, *International Series of Monographs on Physics* (Clarendon, Oxford), 3rd ed.).
Hersil, J., I. Escobar, D. Scott, G. Clark, and S. Olbert, 1961, Phys. Rev. Lett. **6**, 22.
Hillas, A., 2005, J. Phys. G **31**, R95.
Hillas, A. M., 1970, *Proceedings of the 11th ICRC, Budapest, Hungary*, Vol. 3, p. 539.
Hillas, A. M., 1984, Annu. Rev. Astron. Astrophys. **22**, 425.
Hooper, D., S. Sarkar, and A. M. Taylor, 2007, Astropart. Phys. **27**, 199.

Huchra, J., N. Martimbeau, T. Jarrett, R. Cutri, M. Skrutskie, S. Schneider, R. Steining, L. Macri, J. Mader, and T. George, 2005, in *Maps of the Cosmos*, edited by M. Colless, L. Staveley-Smith, and R. A. Stathakis (Astronomical Society of the Pacific, San Francisco, California), Vol. 216, p. 170.
Jiang, Y.-Y., L. Hou, J. Han, X. Sun, and W. Wang, 2010, Astrophys. J. **719**, 459.
Jokipii, J. R., 1987, Astrophys. J. **313**, 842.
Jones, F. C., and D. C. Ellison, 1991, Space Sci. Rev. **58**, 259.
Kakimoto, F. *et al.*, 1996, Nucl. Instrum. Methods Phys. Res., Sect. A **372**, 527.
Kalmykov, N. N., S. S. Ostapchenko, and A. I. Pavlov, 1997, Nucl. Phys. B, Proc. Suppl. **52**, 17.
Kamata, K., and J. Nishimura, 1958, Prog. Theor. Phys. Suppl. **6**, 93.
Kleifges, M. *et al.* (Pierre Auger Collaboration), 2009, in *Proceedings of the 31st ICRC, Lodz, Poland* (University of Lodz, Lodz, Poland).
Kotera, K., and A. Olinto, 2011, Annu. Rev. Astron. Astrophys. **49**, 119.
Kronberg, P. P., 1994, Rep. Prog. Phys. **57**, 325.Krymsky, G. F., 1977, Dokl. Akad. Nauk SSSR **243**, 1306.[Sov. Phys. Dokl. **22**, 327 (1977)]
Kuempel, D., K. H. Kampert, and M. Risse, 2008, Astropart. Phys. **30**, 167.
Kulikov, G., and Khristiansen, 1958, Zh. Eksp. Teor. Fiz. **35**, 441.
Landau, L. D., and I. Pomeranchuk, 1953, Dokl. Akad. Nauk SSSR **92**, 735.
Lawrence, M. A., R. J. O. Reid, and A. A. Watson, 1991, J. Phys. G **17**, 733.
Learned, J. G., and S. Pakvasa, 1995, Astropart. Phys. **3**, 267.
Lidvansky, A. S., 2006, Radiat. Phys. Chem. **75**, 891.
Linsley, J., 1963, Phys. Rev. Lett. **10**, 146.
Linsley, J., 1977, in *Proceedings of the 17th ICRC (Plovdiv, Bulgaria)* (Bulgarian Academy of Sciences, Sofia, Bulgaria), Vol. 12, p. 89.
Linsley, J., 1998, in *Workshop on Observing Giant Cosmic Ray Air Showers From 10(20) eV Particles From Space*, AIP Conf. Proc. No. 433 (AIP, New York), p. 1.
Linsley, J., L. Scarsi, and B. Rossi, 1961, Phys. Rev. Lett. **6**, 485.
Linsley, J., and A. A. Watson, 1981, Phys. Rev. Lett. **46**, 459.
Lipari, P., 2009, Nucl. Phys. B, Proc. Suppl. **196**, 309.
Lyutikov, M., and R. Ouyed, 2007, in *Proceedings of the 30th ICRC, Merida (Mexico)* (Universidad Nacional Autonoma de Mexico, Mexico City, Mexico).
Mannheim, K., R. J. Protheroe, and J. P. Rachen, 2000, Phys. Rev. D **63**, 023003.
Martens, K. *et al.* (HiRes Collaboration), 2007, in *Proceedings of the 30th ICRC, Merida, Mexico* (Universidad Nacional Autonoma de Mexico, Mexico City, Mexico), Vol. 5, p. 1465.
Massaglia, S., 2008, in *Proceedings of the CRIS 2008 Conference, Malfa (Italy)* (INFN, Catania, Italy).
Matthews, J., 2005, Astropart. Phys. **22**, 387.
Matthews, J. A. J. *et al.*, 2010, J. Phys. G **37**, 025202.
Migdal, A. B., 1956, Phys. Rev. **103**, 1811.
Milgrom, M., and V. Usov, 1995, Astrophys. J. **449**, L37.
Mostafa, M. (Pierre Auger Collaboration), 2007, Nucl. Phys. B, Proc. Suppl. **165**, 50.
Nagano, M., K. Kobayakawa, N. Sakaki, and K. Ando, 2004, Astropart. Phys. **22**, 235.
Nagano, M., and A. A. Watson, 2000, Rev. Mod. Phys. **72**, 689.
Nagano, M. *et al.*, 1984, J. Phys. G **10**, 1295.
Nagano, M. *et al.*, 1992, J. Phys. G **18**, 423.
Nerling, F., J. Bluemer, R. Engel, and M. Risse, 2006, Astropart. Phys. **24**, 421.
Nonaka, T. *et al.*, 2009, Nucl. Phys. B, Proc. Suppl. **190**, 26.
Ohoka, H., S. Yoshida, and M. Takeda (AGASA Collaboration), 1997, Nucl. Instrum. Methods Phys. Res., Sect. A **385**, 268.
Ostapchenko, S., 2007, AIP Conf. Proc. **928**, 118.
Panov, A. *et al.*, 2011, arXiv:1101.3246.
Patterson, J., and A. Hillas, 1983, J. Phys. G **9**, 1433.
Peters, B., 1959, Nuovo Cimento Suppl. **14**, 436.
Pierog, T., and K. Werner, 2007, in *Proceedings of the 30th ICRC (Merida, Mexico)* (Universidad Nacional Autonoma de Mexico, Mexico City, Mexico), Vol. 4, p. 629.
Pierog, T., and K. Werner, 2009, Nucl. Phys. B, Proc. Suppl. **196**, 102.
Platino, M. *et al.* (Pierre Auger Collaboration), 2009, in *Proceedings of the 31st ICRC, Lodz, Poland* (University of Lodz, Lodz, Poland).
Privitera, P. *et al.*, 2010, Nucl. Phys. B, Proc. Suppl. **329**, 212.
Ptuskin, V., V. Zirakashvili, and E. Seo, 2010, Astrophys. J. **718**, 31.
Rachen, J., and P. Biermann, 1993, Astron. Astrophys. **272**, 161.
Revenu, B. *et al.* (CODALEMA Collaboration), 2009, arXiv:0906.2832.
Risse, M., and P. Homola, 2007, Mod. Phys. Lett. A **22**, 749.
Rossi, B., and K. Greisen, 1941, Rev. Mod. Phys. **13**, 240.
Ryu, D., S. Das, and H. Kang, 2010, Astrophys. J. **710**, 1422.
Schmidt, F. *et al.*, 2007, in *Proceedings of the 30th ICRC (Merida, Mexico)* (Universidad Nacional Autonoma de Mexico, Mexico City, Mexico).
Schmidt, F. *et al.*, 2008, Astropart. Phys. **29**, 355.
Shinozaki, K. *et al.*, 2002, Astrophys. J. **571**, L117.
Sommers, P., 1995, Astropart. Phys. **3**, 349.
Song, C. *et al.*, 2000, Astropart. Phys. **14**, 7.
Stanev, T., 1997, Astrophys. J. **479**, 290.
Stanev, T., 2010, *High Energy Cosmic Rays*, Springer Praxis Books (Springer-Verlag, Berlin).
Stanev, T., P. L. Biermann, J. Lloyd-Evans, J. P. Rachen, and A. A. Watson, 1995, Phys. Rev. Lett. **75**, 3056.
Stanev, T., R. Engel, A. Mucke, R. J. Protheroe, and J. P. Rachen, 2000, Phys. Rev. D **62**, 093005.
Stecker, F., 1968, Phys. Rev. Lett. **21**, 1016.
Stecker, F., 1969, Phys. Rev. **180**, 1264.
Supanitsky, A. D. *et al.* (Pierre Auger Collaboration), 2008, Astropart. Phys. **29**, 461.
Swordy, S. P. *et al.*, 2000, Astropart. Phys. **13**, 137.
Takeda, M. *et al.*, 1998, Phys. Rev. Lett. **81**, 1163.
Takeda, M. *et al.*, 1999, Astrophys. J. **522**, 225.
Takeda, M. *et al.*, 2003, Astropart. Phys. **19**, 447.
Tokuno, H. *et al.*, 2009, Nucl. Instrum. Methods Phys. Res., Sect. A **601**, 364.
Uchihori, Y. *et al.*, 2000, Astropart. Phys. **13**, 151.
Ulrich, R. *et al.*, 2009, New J. Phys. **11**, 065018.
Unger, M. *et al.* (Pierre Auger Collaboration), 2008, Nucl. Instrum. Methods Phys. Res., Sect. A **588**, 433.
Vachaspati, T., 1997, arXiv:hep-ph/9710292.
Vachaspati, T., 1998, arXiv:astro-ph/9903362.
van den Berg, A. M. (Pierre Auger Collaboration), 2009a, in *31st ICRC, Lodz, Poland* (University of Lodz, Lodz, Poland).
van den Berg, A. M. *et al.* (Pierre Auger Collaboration), 2009b, *Proceedings of the 31st ICRC, Lodz, Poland* (University of Lodz, Lodz, Poland).
Véron-Cetty, M. P., and P. Véron, 2006, Astron. Astrophys. **455**, 773.
Vietri, M., 1995, Astrophys. J. **453**, 883.
Vilenkin, A., and E. P. S. Shellard, 1995, *Cosmic Strings and Other Topological Defects* (Cambridge University Press, Cambridge, United Kingdom).

Watson, A. A. (Pierre Auger Collaboration), 2007, *Invited talk at the 30th International Cosmic Ray Conference (ICRC 2007), Merida, Mexico July 2007* (Universidad Nacional Autonoma de Mexico, Mexico City, Mexico).
Waxman, E., 1995, Phys. Rev. Lett. **75**, 386.
Waxman, E., 2006, Nucl. Phys. B, Proc. Suppl. **151**, 46.
Waxman, E., and J. N. Bahcall, 1998, Phys. Rev. D **59**, 023002.
Wick, S. D., C. D. Dermer, and A. Atoyan, 2004, Astropart. Phys. **21**, 125.
Yoshida, S. *et al.*, 1995, Astropart. Phys. **3**, 105.
Zatsepin, G. T., and V. A. Kuzmin, 1966, JETP Lett. **4**, 78.